Study to improve measurement accuracy and resolution of atmospheric radars

by

Gan Tong

September 2015

Abstract

Radars operated at VHF (30 – 300 MHz) or UHF (300 – 3000 MHz) frequency bands (atmospheric radars; ARs) are sensitive to refractive index perturbations caused by atmospheric turbulence. From a Doppler spectrum collected by a AR, echo power (P), Doppler velocity (V_{d}), and spectrum width (σ_{3dB}) of echoes scattered by the refractive index perturbations (clear-air echo) can be measured. Hereafter, these parameters are referred to as spectral parameters. Because the refractive index irregularities can be produced by temperature and humidity perturbations caused by atmospheric turbulence, ARs can be used to measure turbulence parameters (e.g., dissipation rate and diffusivity).

In order to improve angular resolution or range resolution, spaced receiver antennas or multiple carrier frequencies are used. The former is referred to as coherent radar imaging (CRI) or spatial domain interferometric imaging (SDI). The latter is referred to as range imaging (RIM) or frequency interferometric imaging (FII). In this study, we developed a new radar digital receiver which can perform both RIM and oversampling (OS) on a 1.3-GHz AR (RIM LQ-7). The new radar digital receiver contains a general-purpose software-defined radio receiver referred to as Universal Software Radio Peripheral 2 (USRP2) and a commercial personal computer. Software developed for the digital receiver was written in the C++ language and that developed for signal processing was written in the Python language.

Because high-resolution ARs collect a huge amount of Doppler spectra, methods for calculating the spectral parameters must be simple and fast. Using numerical simulations, we investigated a method for calculating the spectral parameters from Doppler spectra collected in the clear air region. The proposed method has two steps in general. In the first step, the echo range (R_{echo}), in which the Doppler spectrum point with peak intensity is contained and all the smoothed Doppler spectrum points have intensities that are greater than the noise intensity, was determined. For producing the smoothed Doppler spectrum, a running average with equal weight (RA) or multi-taper method (MTM) was used. In the second step, the spectral parameters were calculated using the Doppler spectrum points within R_{echo}. By

comparing the performance of the computation method using RA and that of the computation method using MTM, we concluded that the computation method using RA is more suitable because it has better estimation performance for small spectrum widths and the calculations are faster.

Estimation error of the spectral parameters depends on the determination accuracy of the Doppler spectrum peak and R_{echo}. Furthermore, for the case of a 512-point Doppler spectrum and 13-point RA, the estimation errors tend to be independent of the signal-to-noise ratio (SNR) when the detectability (D) is $\sim$6 or more larger. For a D range of $< \sim$2.5, the estimation errors are significantly large. The results indicate that the estimation accuracy is affected by D. It is recommended that number of incoherent integration times is determined by considering both D and the SNR.

By using the method we proposed, data collected by the vertical beam of the RIM LQ-7 was processed. Measurement using a 1-μs subpulse width, a 8-bit optimum binary code, five frequencies (1357.00, 1357.25, 1357.50, 1357.75, and 1358.00 MHz), 10-MS s^{-1} sampling in the range direction, and the vertical beam was carried out at Shigaraki MU Observatory (34°51′ N, 136°06′ E). Measurement results indicate that RIM in combination with OS achieves unambiguous RIM measurement in the range direction, and hence is useful for improving the accuracy of RIM measurement. Further, measurement results indicate that the high range and time resolution of the RIM LQ-7 are useful for observing the boundary layer.

In the precipitation region, ARs can receive clear-air echoes and Rayleigh scatterings from hydrometeors (hydrometeor echoes) simultaneously. In order to calculate the spectral parameters of the clear-air echo accurately, the clear-air echo must be separated from the hydrometeor echo well. Therefore, we proposed methods (top method and two-echo method) for calculating the spectral parameters in precipitation region. The top method is used when raindrops or solid hydrometeors with small echo intensities exist. The top method sets an echo cut level by using the peak intensity of a clear-air echo. The echo cut level is used for separating clear-air echoes from hydrometeor echoes. The two-echo method is used when solid hydrometeors with large echo intensities exist. The two-echo method sets the echo cut level

by using the local minimum of echo intensity between the clear-air echo and the hydrometeor echo.

In order to determine the optimum echo cut levels for the top method and two-echo method, numerical simulations with different simulation conditions were carried out. The simulation results indicate that the top method with L of 10 dB shows the best performance and that L down to 5 dB also can be used. For the two-echo method, the simulation results indicate that an echo cut level which is 1 dB greater than the minimum echo intensity has good performance.

Measurement results obtained by the vertical beam of the MU radar at Shigaraki MU Observatory during a precipitation event on 26 October 2009 were used for evaluating the performance of the top and two-echo methods. The measurement results demonstrate that the top method and two-echo method are useful for reducing the errors of spectral parameters.

We believe that the high range and time resolution of RIM LQ-7 are useful for observing the boundary layer. Further, the top and two-echo methods are useful for measuring the vertical wind in precipitation for 50-MHz band ARs.

Acknowledgements

The author wishes to express his gratitude to Prof. Mamoru Yamamoto of Research Institute for Sustainable Humanosphere (RISH), Kyoto University and Dr. Masayuki K. Yamamoto of National Institute of Information and Communications Technology (NICT) for their guidance, stimulating supervision for my research. Their overwhelming encouragements and constructive approach as well as their high standards and expertise have encouraged me to be better.

The author also wants to express his appreciation to Dr. Hiroyuki Hashiguchi of RISH for his valuable advices about the present work.

The author wishes to thank Prof. Hajime Okamoto of Research Institute for Applied Mechanics (RIAM), Kyushu University for giving him many valuable comments and advices in research meeting, conferences, and personal discussions.

Thanks are also due to Dr. Masanori Yabuki of RISH, Associate Prof. Luce Hubert of Université du Sud Toulon-Var, France, Associate Prof. Richard Wilson of Université Pierre et Marie Curie, France, and Prof. Tomoyuki Nakajo of Department of Electrical, Electronics and Computer Engineering, Fukui University of Technology for their discussions and advices. The author expresses his gratitude to the members of Yamamoto laboratory, RISH for their kindly supports.

The MU radar belongs to and is operated by RISH, Kyoto University. The LQ-7 data and radiosonde data were provided by RISH, Kyoto University. The author's study in Japan was financially supported by the Ministry of Education, Culture, Sports, Science and Technology (MEXT), Japan.

Last but not the least, I gratefully acknowledge the support of my parents and BingBing Yu, who is my angel, for their patience, dedication and unconditional love.

Contents

List of Figures

List of Tables

Abbreviations

ABL	**Atmospheric boundary layer**
AP	**Automatic processing**
AR	**Atmospheric radar**
BLR	**Boundary layer radar**
CRI	**Coherent radar imaging**
DFT	**Discrete Fourier transform**
DSD	**Drop size distribution**
DSP	**Digital signal processor**
EAR	**Equatorial Atmosphere Radar**
ECL	**Echo cut level**
EPL	**Echo peak level**
FFT	**Fast Fourier transform**
FII	**Frequency interferometric imaging**
FPGA	**Field programmable gate array**
IGW	**Internal gravity wave**
JST	**Japan Standard Time**
LNA	**Low noise amplifier**
MAARSY	**Middle Atmosphere Alomar Radar System**
MC	**Manual correction**
MEL	**Minimum echo level**
MTM	**Multi-taper method**
MU	**Middle and Upper atmosphere**
NRB	**Normalized relative backscatter**
NWPM	**Numerical Weather Prediction Models**
OS	**Oversampling**

PA	**Power aperture**
PANSY	**Program of the Antarctic Syowa MST/IT Radar**
PC	**Personal computer**
PRT	**Pulse repetition time**
RA	**Running average**
RASS	**Radio Acoustic Sounding System**
RF	**Radio frequency**
RIM	**Range imaging**
RISH	**Research Institute for Sustainable Humanosphere**
RMS	**Root-mean-square**
SDI	**Spatial domain interferometric imaging**
SDR	**Software-defined radio**
SNR	**Signal-to-noise ratio**
TC	**Tropical cyclone**
UDP	**User Datagram Protocol**
UHD	**Universal Software Radio Peripheral Hardware Driver**
USRP2	**Universal Software Radio Peripheral 2**
WINDAS	**Wind Profiler Data Acquisition System**

Chapter 1

General Introduction

1.1 Radar measurements of the atmosphere

1.1.1 Atmospheric radar

During the last three decades, enormous progress has been made in remote-sensing of the lower atmosphere (the region from near ground level to the tropopause) and the middle atmosphere (the region between the tropopause and approximately 100 km in altitude) using sensitive atmospheric radars (hereafter, ARs; e.g., *Balsley and Gage* [1980]; *Gage and Balsley* [1978]; *Röttger and Larsen* [1990]). ARs receive very weak scattering from radio refractive index fluctuations produced by turbulence [*Woodman and Guillen*, 1974]. Due to the exponential decrease of atmospheric density (and accordingly the exponential decrease of radio refractive index fluctuations) with increasing altitude, the backscattering is too weak for useful echoes to be detected above 20–25 km in altitude. The backscattering above about 60 km, which is normally detected only during daylight hours, arises primarily from electrons that enhances the scattering from the turbulence at these altitudes [*Woodman and Guillen*, 1974].

The energy spectrum of atmospheric turbulence falls off rapidly with decreasing eddy size in the inertia subrange, and radar radio waves are scattered only from turbulent eddies with a scale size that satisfies the Bragg condition (i.e., one half of

the transmitted wavelength). Accordingly, higher sensitivity to turbulences scattering is achieved in the VHF (30 – 300 MHz)/UHF (300 – 3000 MHz) bands than in the microwave frequency band generally used for meteorological radars. Therefore, ARs are often operated at VHF or UHF bands.

Initial AR research started with radar systems dedicated primarily to ionospheric incoherent scatter (IS) studies at Jicamarca, Peru, Arecibo, Puerto Rico, and so forth. It immediately progressed to extensive design and use of systems specifically intended for the atmosphere research. Backscattering from the mesosphere is so weak even at 50-MHz band that VHF ARs are fitted with a high peak transmitted power of the order of one megawatt (MW) and large antenna area of the order of 10^4 m^2. Various radars with less sensitivities that operate at frequencies higher than 50 MHz are widely put to practical use for remote-sensing of the lower stratosphere and troposphere (ST radar), troposphere (T radar), lower troposphere (Lower Troposphere Radar or LTR) or atmospheric boundary layers (BL radar or BLR). In general, larger systems have the capability to carry out varies experiments with greater degrees of complexity in features, such as beam steerability, pulse coding, and data acquisition, while smaller systems tend to be designed for more dedicated purposes and often tend to specialize in particular techniques [*Hocking*, 1997].

The most important capability of ARs is continuous monitoring of three dimensional atmospheric winds over an altitude range including most of the troposphere, lower stratosphere and mesosphere. In particular, there has been no other direct means to observe wind velocities continuously during all weather conditions (e.g., *Fukao et al.* [1985b] and [2007]; *Hocking* [2011]; *Yamamoto et al.* [2008], [2009a], and [2009b]). Large efforts have been put forth to investigate the reliability and accuracy of observations by ARs. Comparisons have shown that the accuracy of the wind measurement of a well-operated and well-maintained AR is at least comparable to the accuracy of radiosonde wind data. In addition, ARs operated at UHF are sensitive enough to measure precipitation as well. Thus, they also can be used for precipitation measurement. Typical altitude and time resolutions for middle atmosphere observations are several hundred meters and several minutes or less. Details of atmospheric wind measurements by ARs will be introduced in the following sections.

The heights from which one may expect to achieve useful echoes at a specific radar frequency depend on power aperture (PA) product. A PA product exceeding 10^8 Wm^2 is required to observe up to the mesosphere. For the Middle and Upper atmosphere (MU) radar at Shigaraki, Japan, the PA product is 9.5×10^9 Wm^2 [*Fukao et al.*, 1985a] (Figure 1.1). For the Equatorial Atmosphere Radar (EAR) at Kototabang, Indonesia, the PA product is 9.5×10^8 Wm^2 [*Fukao et al.*, 2003]. Most recently the Middle Atmosphere Alomar Radar System (MAARSY) at Norwegian island Andøya has a PA product of 5.04×10^9 Wm^2 [*Latteck et al.*, 2012]. For the Antarctic Syowa MST/IT radar (PANSY) at Syowa Station (69°S, 39°E) has a PA product of 9.36×10^9 Wm^2 [*Sato et al.*, 2014].

Currently, there are several operational networks of those instruments in the America, Europe and Japan which provide continuous wind measurements in real-time and most of the data are successfully assimilated in numerical weather prediction models (NWPM).

FIGURE 1.1: A bird's eye view of the MU radar located at Shigaraki, Japan (34.85°N, 136.10°E).

The Radio Acoustic Sounding System (RASS) is one of the most interesting applications for ARs (e.g., *Matuura et al.* [1986]; *Tsuda et al.* [1989]). In RASS, ARs receive echoes from periodic fluctuations in the radio refractive index due to density

fluctuations artificially produced by acoustic sounders on the surface. The acoustic wavelength should be equal to half the radar wavelength to satisfy the Bragg condition. The observed sound speeds provide local (virtual) temperature with an accuracy better than 0.5 °C up to an altitude of ∼20 km, depending on weather conditions [*Tsuda et al.*, 1994]. A new technique has been developed to monitor a humidity profile with ARs by incorporating the RASS technique (e.g., *Hocking and Mu* [1997]; *Tsuda et al.* [2001]; *Furumoto et al.* [2003]).

1.1.2 Measurements of gravity waves and other meteorological processes

Internal gravity waves (IGWs) exist due to stratification of the Earth's atmosphere, while inertio-gravity waves result from a combination of stratification and Coriolis effects. They are generated either in the lower part of the atmosphere or in the middle atmosphere and propagate upward, producing dynamical variations with periods from minutes to hours. It is now well established that IGWs transport energy and momentum over large distances, serve as the mechanism for coupling different height regions, and make a significant contribution to the general circulation in the middle atmosphere, in particular, to formation of the "weak (zonal) wind" region near 90 km in altitude (e.g., *Lindzen* [1981]; *Matsuno* [1982]). Small dissipation leads to quasi-exponential growth of IGW amplitudes with increasing altitude due to the decrease of atmospheric density with increasing altitude. At the breaking level, where wave amplitude $|v^{'}| = |c - \overline{u}|$ (where c and u are wave phase velocity and mean flow, respectively), the wave meets unstable regions caused either by dynamical (or shear) instability where the Richardson number $R_{\mathrm{i}} < 1/4$ or convective instability where $R_{\mathrm{i}} < 0$, and strong turbulence generation occurs. Above that level the amplitude ceases to grow, and the waves become saturated, producing wave forced to the mean flow.

ARs are the most suitable instruments for studying IGWs due to their capability of continuous measurement of three-dimensional winds with fine time resolution simultaneously at many altitudes. The primary source of IGWs is a variety of dynamical processes in the lower atmosphere. First, mountain waves that are generated on lee side when flows pass over mountains are a typical source (e.g., *Nastrom and*

Fritts [1992]; *Lott and Teitelbaum* [1993]). A second source is shear instability in jet streams (e.g., *Hines* [1968]; *Lindzen* [1984]; *Fritts* [1984]; *Fritts and Nastrom* [1992]). Third, a good correlation has been noticed between IGW intensity and the passage of cold/warm fronts (e.g., *Einaudi et al.* [1978]). The generation of long-period inertio-gravity waves by synoptic-scale motions and jet streams is described by the theory of spontaneous adjustment that the wave motions appear as the result of permanent competition between the violation of equilibrium of pressure and velocity and the tendency of the atmosphere to establish the quasi-geostrophic balance of these fields (e.g., *Gill* [1982]; *O'Sullivan and Dunkerton* [1995]). Despite the important role of IGWs in formation of the general circulation, thermal regime, and composition of the middle atmosphere, their origin is still an issue in need of further investigation.

By using ARs, the vertical eddy diffusivity K, due to wave breaking turbulence with spatial scales of 10–100 m, has been estimated often from power spectral width (e.g., *Hocking* [1983], [1985], and [1986]). By an extended analysis using a seven-year (1986–92) database of MU radar data, *Kurosaki et al.* [1996] confirmed features of K.

Microwave meteorological radars have long been standard tools for the study of precipitating air. They detect echoes from precipitation particles but not from the ambient air. On the other hand, ARs have a unique feature in that they can detect precipitation echoes simultaneously with the echoes from the ambient air [*Fukao et al.*, 1985c]. The two echoes are discriminated according to their Doppler shifts, making it possible to estimate both air and precipitation parameters simultaneously. An algorithm has been developed that classifies precipitating clouds into either stratiform, mixed stratiform/convective, deep convective, or shallow convective clouds by analyzing the vertical structure of reflectivity, velocity, and spectral width derived from measurements made with the vertically pointing beam of UHF ARs (e.g., *Williams et al.* [1995]; *Renggono et al.* [2001]).

Tropical cyclones (TC or typhoons) have been observed extensively with the ARs in Japan and Taiwan (e.g., *Fukao et al.* [1985c]; *Sato et al.* [1991]; *Sato* [1993]; *May et al.* [1994]; *Teshiba et al.* [2001] and [2004]; *Shibagaki et al.* [2003]). A mature-stage TC forms an "eye" where no clouds and precipitation exist, which generally makes

it difficult to observe with microwave meteorological radars. Therefore, ARs are necessary equipment for observing the TC (e.g., *Shibagaki et al.* [2003]; *Teshiba et al.* [2005]).

The atmospheric boundary layer (ABL) is of cardinal importance for atmospheric chemistry, pollutant studies and numerical weather modeling. Because the refractive index structure constant has a local maximum at the inversion due to small-scale buoyancy fluctuations, the depth of the ABL has been determined successfully with ARs (e.g., *Angevine et al.* [1994]; *Hashiguchi et al.* [1995a] and [1995b]).

1.2 Basics of atmospheric radar

1.2.1 Scattering mechanism of atmospheric radars

The primary mechanism of backscatter from clear air is radio refractive index fluctuation experienced by an electromagnetic wave due to the presence of localized scattering centers known as refractive index irregularities. The radio refractive index of the clear air n is modeled by [*Balsley and Gage*, 1980]

$$n = 1 + 7.76 \times 10^{-5} \frac{p}{T} + 3.73 \times 10^{-1} \frac{e}{T^2} - 40.3 \frac{N_\mathrm{e}}{f^2}, \tag{1.1}$$

where p is atmosphere pressure [hPa], T is atmospheric temperature [K], e is partial pressure of water vapor [hPa], N_e is the number density of free electrons [m^{-3}], f is the radar frequency [Hz]. The second term of the right-hand side is the contribution from dipole moment due to polarization field of neutral molecules. It contributes most to the refractive index between middle troposphere and stratopause. The third term is due to the permanent dipole moment of the water molecule, which is significant only in lower troposphere. The fourth term is the contribution from free electrons. It is significant only in the mesosphere and above, and can be ignored in the stratopause or lower layer. Figure 1.2 shows typical height profiles of contributions of water vapor, dry air, and free electrons to the radio refractive index. In general, n is almost 1 and the value is around 1.0003 or smaller. The value of n varies due to turbulence. However, the variance is extremely small which is around

10^{-5} to 10^{-6}. Because of this reason, the scale of abscissa that shows the change of n is given by $\log_{10}(n-1)$.

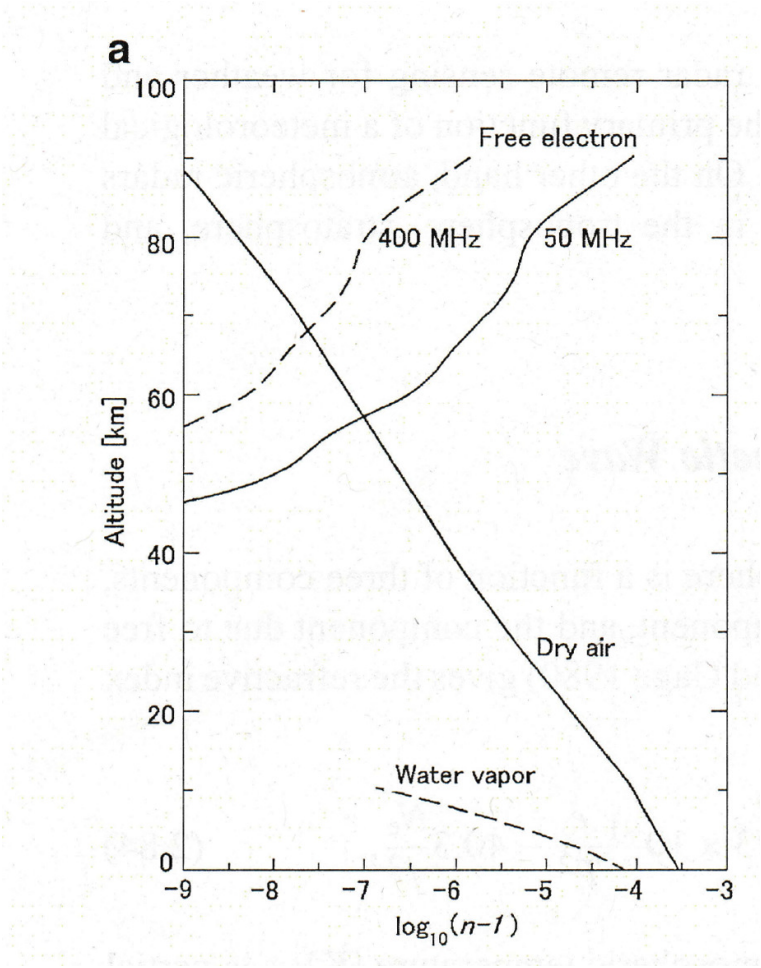

FIGURE 1.2: Height profiles of contributions of water vapor, dry air, and free electrons to the radio refractive index n (from [*Sato*, 1988]).

Scattering from the clear air is produced by randomly distributed refractive index perturbations, i.e., the refractive index $n \equiv n(r)$, where r is the distance between radar and a point in the region of refractive index perturbations, resulting from turbulent mixing of the gradients of the potential refractive index. For a monostatic radar (a single antenna for transmission and reception), scattering arises from refractive index perturbations caused by atmospheric turbulence has mainly the scale of half the radar wavelength along the beam direction. It is called "Bragg scatter". From a point view of radar observations from Bragg scatterers, only the fluctuating component with the spatial scale of a half transmitted wavelength in the direction of radar wave propagation contributes the scattering. In other word, a

radar ideally samples only the spectral component of refractive index perturbations with a half transmitted wavelength (λ). Thus, the structure wave number κ for the Bragg scatter becomes

$$\kappa = \frac{2\pi}{\frac{\lambda}{2}} = \frac{4\pi}{\lambda} = 2k, \tag{1.2}$$

where $\kappa = |\kappa|$, and k is the radar wave number vector of scattered wave.

1.2.2 Radar equation

Considering the case of a radar transmitting a signal which has power of P_t. The radar has an antenna which has effective area of A. $g_\mathrm{t}(\theta, \phi)$ is the transmitted antenna gain at the scatter direction, where θ and ϕ are the polar angles. When the signal scatters from a scatterer with a cross section of σ (explained later) and r away from the antenna, the received power P_r can be calculated by

$$P_\mathrm{r} = \frac{P_\mathrm{t} g_\mathrm{t}(\theta, \phi) A \sigma}{(4\pi r^2)^2}. \tag{1.3}$$

It is noted that the gain of antenna G and A are related as follows

$$G = \frac{4\pi A}{\lambda^2}, \tag{1.4}$$

where λ is the radar wavelength. A monostatic radar uses the same antenna for transmission and reception. Therefore, the reception gain ($g_\mathrm{r}(\theta, \phi)$) equals to the transmission gain that

$$g_\mathrm{t}(\theta, \phi) = g_\mathrm{r}(\theta, \phi) = g(\theta, \phi). \tag{1.5}$$

By substituting (1.4) and (1.5) into (1.3), the received power is expressed by

$$P_\mathrm{r} = \frac{P_\mathrm{t} g(\theta, \phi)^2 \lambda^2 \sigma}{(4\pi)^3 r^4}. \tag{1.6}$$

In the case that the scattering from the scatterer occurs isotropically in all directions, and the scattered power density at range r from the particle is S_s, the total scattered power becomes $4\pi r^2 S_\mathrm{s}$. On the other hand, the input power is $S_\mathrm{i}\sigma$, when the incident power density S_i is intercepted by the particle with σ. Then, σ can be

calculated as

$$\sigma = \lim_{r\to\infty} 4\pi r^2 \frac{S_\mathrm{s}}{S_\mathrm{i}}. \tag{1.7}$$

σ is defined as the area of a supposed isotropic scatterer which radiates the same power as that reradiated by the particle concerned to the receiving antenna. For distributed discrete hard scatterers such as raindrops and fog droplets, the radar cross section of individual scatterer is extremely small. In general, the cross sections of these distributed scatterers are treated by the total amount $\sum\sigma$. $\sum\sigma$ is given by the produce of V and η as

$$\sum\sigma = V\eta, \tag{1.8}$$

where V is radar resolution volume, η is called volume reflectivity. V is expediently assumed to be the shaded truncated cone of the radius of radar beam width and length of $c\tau/2$ that τ is the pulse width. Figure 1.3 shows an example of the total cross sections within V.

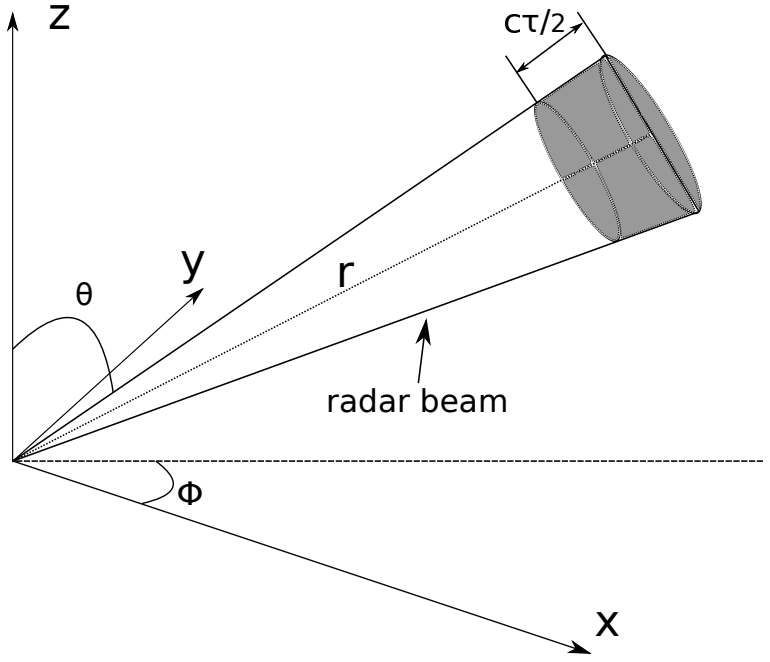

FIGURE 1.3: The coordinate system and the scattering resolution volume of a pulse radar. The shaded area is assumed to be the radar resolution volume V.

The derivative of V in the coordinates of Figure 1.3 is given by

$$\mathrm{d}V = r^2 \mathrm{d}r \sin\theta \mathrm{d}\theta \mathrm{d}\phi. \tag{1.9}$$

Here we introduce V_6, which is circumscribed by the 6-dB contour of radar antenna beam width, τ weighted with window function, and the receiver bandwidth. Applying (1.9), V is given by

$$V = V_6 = r^2 \int |W(r)|^2 \mathrm{d}r \int_0^{2\pi} \int_0^{\pi} f^4(\theta, \phi) \sin\theta \mathrm{d}\theta \mathrm{d}\phi, \tag{1.10}$$

where $|W(r)|$ is the range weighting function and $|W(r)|^2$ approaches $c\tau/2$. A factor $f^4(\theta, \phi)$ is the two-way antenna function, and the 6-dB width of $f^4(\theta, \phi)$ is often taken to be the angular width of V_6. Thus, $f^2(\theta, \phi)$ is the normalized one-way radiation pattern of the antenna. In general, the radiation pattern of the antenna can be represented by the Gaussian function. Therefore, we can show that

$$\int_0^{2\pi} \int_0^{\pi} f^4(\theta, \phi) \sin\theta \mathrm{d}\theta \mathrm{d}\phi = \pi\theta_1^2/8\ln 2, \tag{1.11}$$

where θ_1 is the 3-dB width of the one-way pattern (in radians). Then, V_6 can be written as

$$V_6 = r^2 \frac{c\tau}{2} \frac{\pi\theta_1^2}{8\ln 2}. \tag{1.12}$$

Substituting (1.12) into (1.6), we compute the signal mean power at the antenna to be given by

$$E[P_\mathrm{r}] = \frac{P_\mathrm{t} g^2 \lambda^2 \theta_1^2 c\tau}{2^{10}(\ln 2)\pi^2 r^2} \eta. \tag{1.13}$$

The above equation is called the radar equation for distributed hard scatterers when any loss is not taken into consideration. It is noted that the received power for a single isolated scatterer is proportional to r^{-4} as show in (1.6). On the other hand, it is proportional to r^{-2} for distributed hard scatterers as shown in (1.13).

If the perturbations caused by turbulence uniformly fill the radar resolution volume, it is possible to define a distribution of Bragg scatterers so that the radar equation can be basically derived in the same way as the radar equation for distributed hard scatterers (e.g., (1.13)).

1.2.3 Radar reflectivity factor

The cross section σ for a raindrop with diameter D and permittivity ε can be expressed as

$$\sigma = \frac{\pi^5}{\lambda^4}|K|^2 D^6, \tag{1.14}$$

where K is given by

$$K = \frac{\varepsilon - \varepsilon_0}{\varepsilon + 2\varepsilon_0}, \tag{1.15}$$

where ε_0 is the permittivity of propagation medium (i.e., the atmosphere). Volume reflectivity η, the backscattering cross section per unit volume, for spherical particles have distribution diameters in a unit volume is

$$\eta = \int_{D_{\min}}^{D_{\max}} \sigma(D) N(D) \mathrm{d}D, \tag{1.16}$$

$D_{\min}$ and $D_{\min}$ are the minimum and maximum values of the raindrop diameters in the unit volume, $N(D)$ is the drop size distribution (DSD) of minute precipitation particles. Substituting (1.14) into (1.16), η is expressed as

$$\eta = \frac{\pi^5}{\lambda^4}|K|^2 \int_{D_{\min}}^{D_{\max}} D^6 N(D) \mathrm{d}D. \tag{1.17}$$

The integral of (1.17) is called the radar reflectivity factor or radar reflectivity index (Z), which is defined as

$$Z = \int_{D_{\min}}^{D_{\max}} D^6 N(D) \mathrm{d}D. \tag{1.18}$$

Further, (1.17) is expressed as

$$\eta = \frac{\pi^5}{\lambda^4}|K|^2 Z. \tag{1.19}$$

The above equation shows that η is inversely proportional to the forth power of wavelength λ.

The structure constant for the perturbations (refractive index structure constant) C_n^2 is defined as

$$\overline{[n(r+\Delta r)-n(r)]^2} = C_n^2 |\Delta r|^{2/3}, \tag{1.20}$$

where Δr is a small distance between two space locations. The quantity C_n^2 is a measure of the mean-square refractive index perturbations over the distance Δr with the inertial subrange. By using a radio of wavelength λ and C_n^2, the radar reflectivity for reflective index perturbation can be calculated as (e.g., *Ottersten* [1969])

$$\eta \simeq 0.38 C_n^2 \lambda^{-1/3}. \tag{1.21}$$

The value of C_n^2 significantly varies in altitudes, seasons, and others, and approximately becomes 10^{-12} to 10^{-18} $\mathrm{m}^{-2/3}$. Z for distributed scatterers usually takes values around 10^0 to 10^4 $\mathrm{mm}^6\mathrm{m}^{-3}$ for rain and 10^{-3} to 10^{-1} $\mathrm{mm}^6\mathrm{m}^{-3}$ for fog and cloud. Using these typical values for C_n^2 and Z, the values of η are shown in Figure 1.4. The figure indicates that the radar reflectivity due refractive index perturbations becomes dominate in larger radar wavelengths, whereas the radar reflectivity by hard scatterers such as rain drops becomes larger at radar wavelengths of several-tens centimeters or shorter.

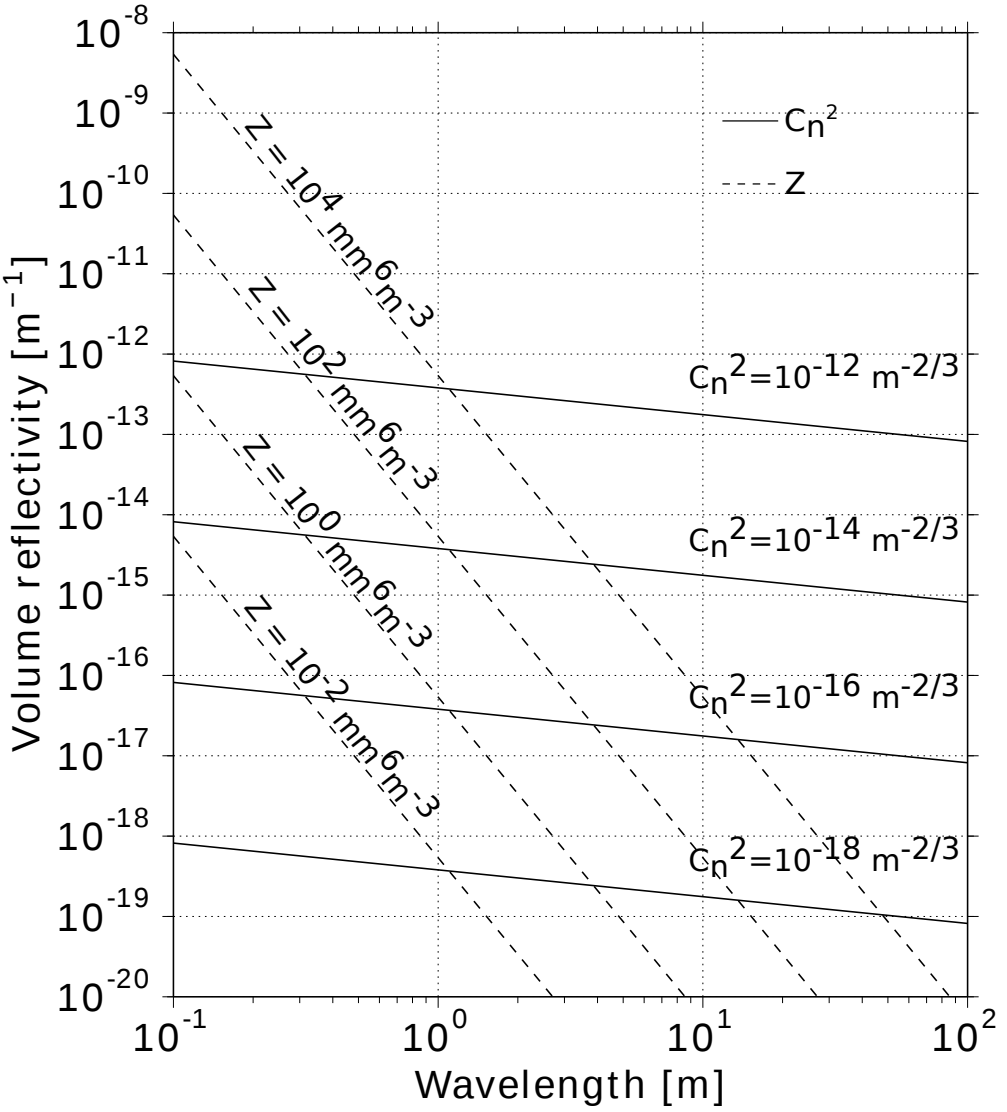

FIGURE 1.4: Volume reflectivity (η) for the atmospheric turbulence (solid lines) and the precipitation (dashed lines) versus radar wavelength.

Figures 1.5 and 1.6 show an example of Doppler spectra collected by a 46.5-MHz AR (VHF AR) and a 1357.5-MHz AR (UHF AR), respectively, in precipitation region. It is noted that the VHF AR and UHF AR are ∼110 m apart from each other. Therefore, the Doppler spectra can be considered scattered from similar scatterers. For the VHF AR, the wavelength is ∼6.45 m. Therefore, the intensity of hydrometeor echo is smaller than that of clear-air echo. The peak of clear-air echo locates at ~ -0.1 m s^{-1} and has intensity ∼56 dB. For hydrometeor echo, the peak locates at ∼6.5 m s^{-1} and has intensity ∼53 dB. For the UHF AR, the wavelength is ∼0.22 m that it is more sensitive to hydrometeors. The peak of hydrometeor echo

locates at ∼5.5 m s^{-1} and has intensity ∼52 dB. For the VHF and UHF ARs, the hydrometeor echoes are seen around the Doppler shift of ∼6 m s^{-1}. However, the spectral shape is different from each other. For the UHF AR, because the intensity of hydrometeor echo is greater than that of the clear-air echo, the peak of clear-air echo cannot be detected accurately.

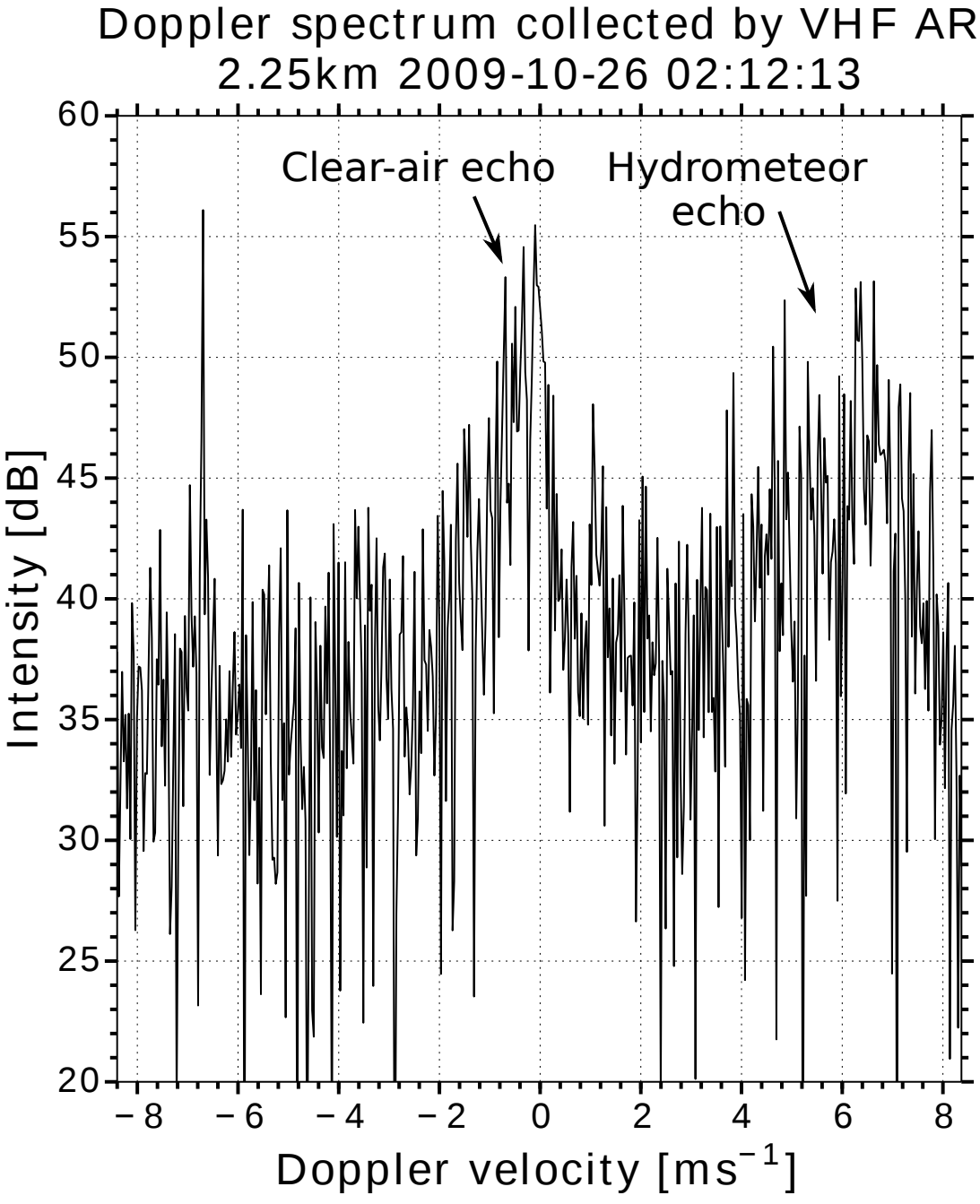

FIGURE 1.5: A Doppler spectrum collected by a VHF AR in precipitation region.

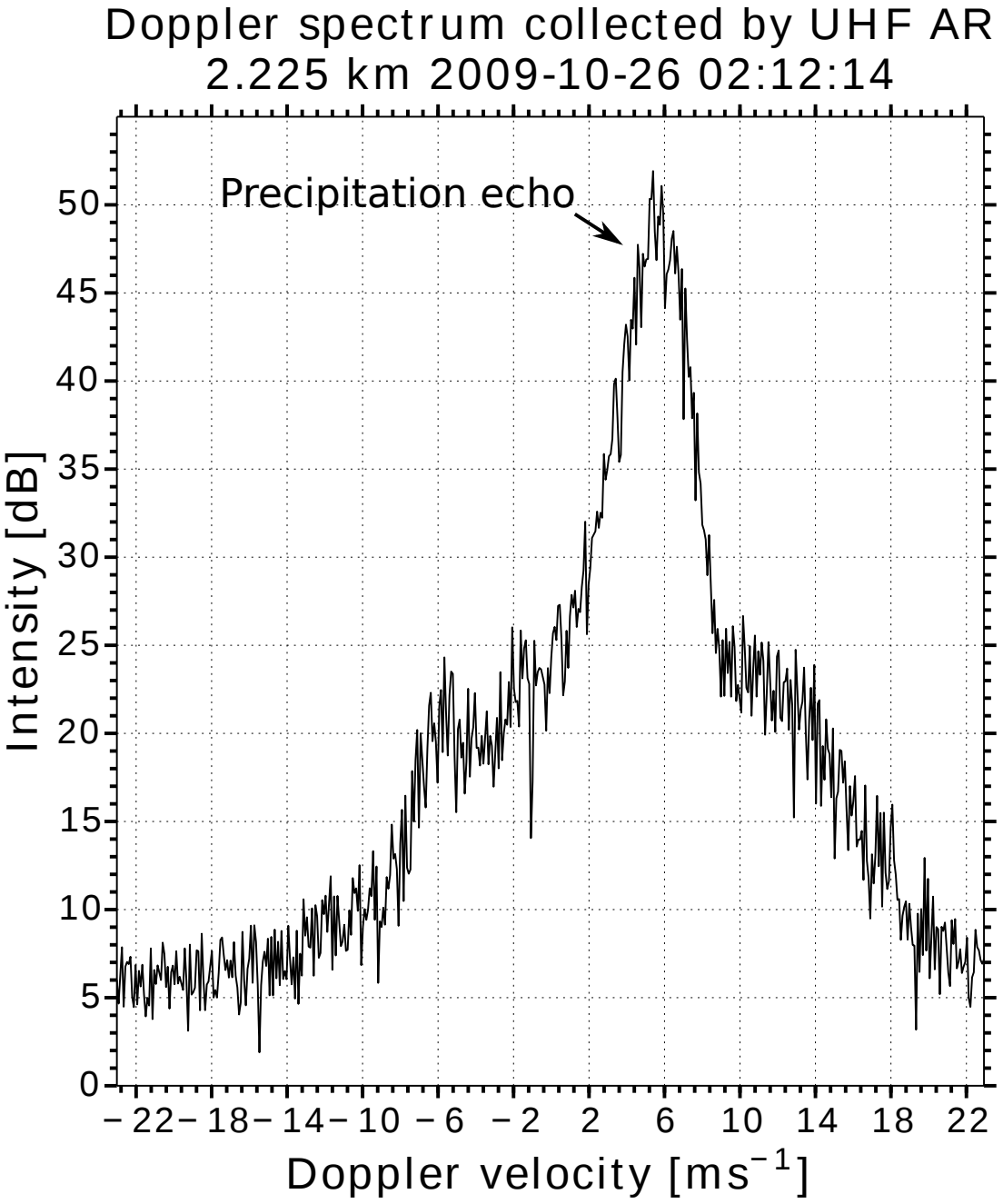

FIGURE 1.6: A Doppler spectrum collected by a UHF AR in precipitation region.

1.2.4 Doppler velocity measurements

1.2.4.1 Calculation of Doppler velocity

Radar waves incident on a scatterer forces electromagnetic vibrations to the scatterer. If the scatterer moves toward the radar, internal vibrations will be faster than that for a stationary scatterer because the wave's apparent propagation speed relative to the scatter is faster and thus the approaching scatterer experiences more rapid fluctuations of incident waves. Thus, the backscattered radiation (i.e., echoes) received by the radar will have higher frequency.

If the phase differences between transmitted pulses and received signals (echoes) from a scatterer are measured, the frequency shift (Doppler shift) of received signals from the transmitted pulses can be calculated. This functional capability is limited only to coherent radars, which have the stable transmitted pulse phase and handle phase information of every transmitted pulses and received echoes.

If the radar transmitted wavelength is λ, and the range to the scatterer is r, the two-way path from the radar to scatterer normalized by λ (i.e., total number of wavelengths) is $2r/\lambda$. It corresponds to the phase change of $(2r/\lambda) \times 2\pi = 4\pi r/\lambda$ radians. Thus, when the initial phase of transmitted signal is φ_0, the phase of received echo becomes

$$\varphi = -\frac{4\pi r}{\lambda} + \varphi_0, \tag{1.22}$$

where the sign of minus means a phase delay. The phase change, which is derivative with respect to time, is

$$\frac{\mathrm{d}\varphi}{\mathrm{d}t} = -\frac{4\pi}{\lambda}\frac{\mathrm{d}r}{\mathrm{d}t}. \tag{1.23}$$

If the movement of the scatter is toward (or away from) the radar beam, the Doppler velocity given by $V_\mathrm{d} = \mathrm{d}r/\mathrm{d}t$ becomes negative (or positive). The value $\mathrm{d}\varphi/\mathrm{d}t$ is called Doppler angular frequency ω_d, which is equal to $2\pi f_\mathrm{d}$, where f_d is called Doppler shift or Doppler frequency. Substituting these values into (1.23), the basic relations of Doppler radar is given by

$$f_\mathrm{d} = \frac{\omega_\mathrm{d}}{2\pi} = -\frac{2V_\mathrm{d}}{\lambda}. \tag{1.24}$$

The measurement of the Doppler shift in a single short received signal is principally possible, but not a practical approach for short pulse Doppler radars. Instead, the change of the echo's phase angle within one transmitted pulse to the next is commonly measured. As stated in (1.22), the phase angle is proportional to the scatterer's range and equals to twice the number of wavelengths, between the radar and the scatterer. Thus, the distance to the scatterer can be measured quite precisely with the phase angle. However, φ change is the more accurate measure of changes in scatterer location. For example, a change of r by $\lambda/4$ causes φ changes of 180°, a large angular change, whereas the change δt along t is $\delta t = \lambda/2c$ a extremely tiny value of t. Thus, the scatterer motion is measured by the changes in φ.

There is ambiguity because the phase can only be determined within a wavelength. Nevertheless, the change of the echo phase, from pulse to pulse, is used to measure V_{d}, the time rate-of-change of range to the scatter. Pulses of the time interval T_{s} are transmitted, thus echoes from a stationary scatter will periodically appear at $t = 2r/c + mT_{\mathrm{s}}$, where m =1,2,3,... defines each pulse. Conceptual traces for $I(t, mT_{\mathrm{s}})$ of echoes from a distribution of scatterers are shown in Figure 1.7.

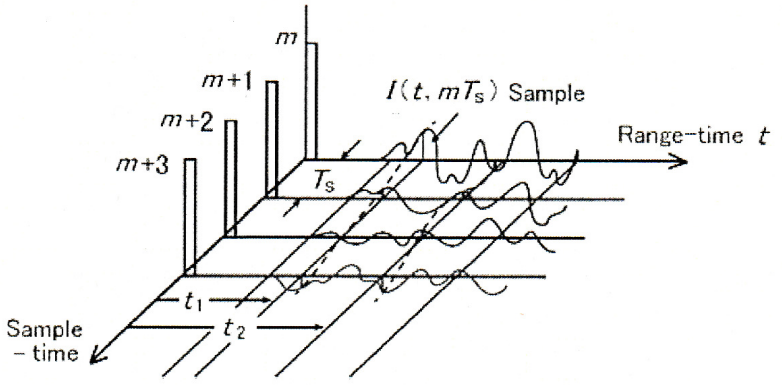

FIGURE 1.7: Conceptual traces for $I(t, mT_{\mathrm{s}})$ of echoes from a distribution of scatterers (from [*Doviak and Zrnić*, 2006]).

The solid line traces represent $I(t, mT_{\mathrm{s}})$ for the mth T_{s} interval. Dashed lines connect samples at each t, where t determines the range $r = ct/2$. In this sampling process, the sampled echo voltage is written as

$$V(t, mT_{\mathrm{s}}) = I(t, mT_{\mathrm{s}}) + jQ(t, mT_{\mathrm{s}}). \tag{1.25}$$

The sampled echo voltage of (1.25) can be represented as a vector which has the amplitude $|V(t)|$ and echo phase φ, where φ is positive when measured counter-clockwise (ccw) from the $I(t, mT_s)$ axis. Figure 1.8 shows vector presentation of five samples at five intervals ($mT_s, m = 1, 2, ..., 5$) for the moving scatterers.

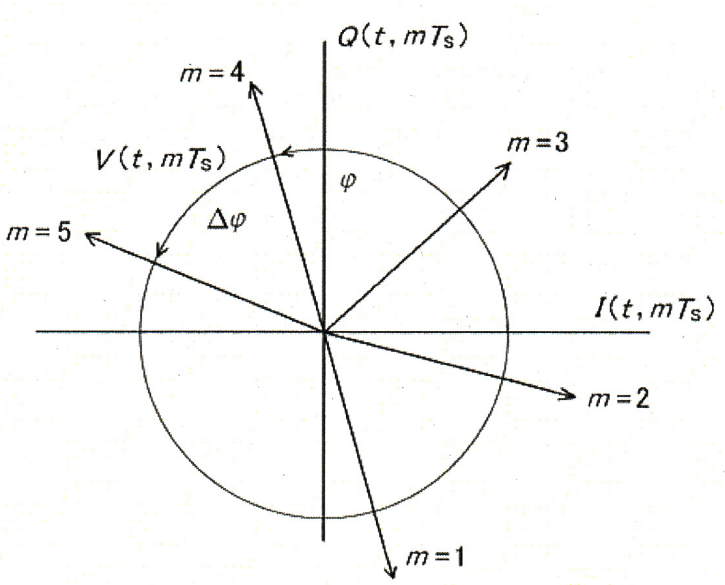

FIGURE 1.8: Vector presentation of five samples at five internals for a moving scatterer (from [*Doviak and Palmer*, 2014]).

If the scatterer moves, not only the echo will change its location along t, but φ also changes according to (1.22), its position along t and φ can be in principle used to measure the change in scatterer location, and thus indirectly its radial velocity. From (1.23) and (1.24),

$$\frac{\Delta\varphi}{\Delta t} = \frac{\varphi_{\mathrm{m}} - \varphi_{\mathrm{m-1}}}{T_{\mathrm{s}}} = \omega_{\mathrm{d}} = 2\pi f_{\mathrm{d}}, \tag{1.26}$$

$$V_{\mathrm{d}} = -\frac{\lambda f_{\mathrm{d}}}{2}, \tag{1.27}$$

where T_{s} is the sample time interval equals to the pulse repetition time (PRT). Negative (positive) f_{d}, where a scatterer moves away from (approaches toward) radar, defines velocity as positive (negative) by following the convention.

1.2.4.2 Nyquist limitation

According to the Shannon and Someya's sampling theorem, the maximum measurable frequency is a half of the frequency of signal sampling, i.e., half of the pulse repetition frequency which is a reciprocal of the data interval. Therefore, the maximum measurable Doppler frequency f_{dmax} is given by

$$f_{\mathrm{dmax}} = \frac{1}{2T_{\mathrm{s}}}. \tag{1.28}$$

If the Doppler frequency of a scatter f_{d} exceeds f_{dmax} or $-f_{\mathrm{dmax}}$, a frequency aliasing occurs and the measured Doppler frequency becomes ambiguous. The maximum velocity below which f_{d} is not affected by aliasing is the Nyquist limiting v_{N} which is expressed as

$$v_{\mathrm{N}} = \frac{\lambda}{4T_{\mathrm{s}}}. \tag{1.29}$$

When the radial velocity V_{r} of a scatterer exceeds the Nyquist limit, the Doppler velocity is folded and aliased as illustrated in Figure 1.9, and the Doppler velocity V_{d} measured with a radar takes the value between v_{N} and $-v_{\mathrm{N}}$.

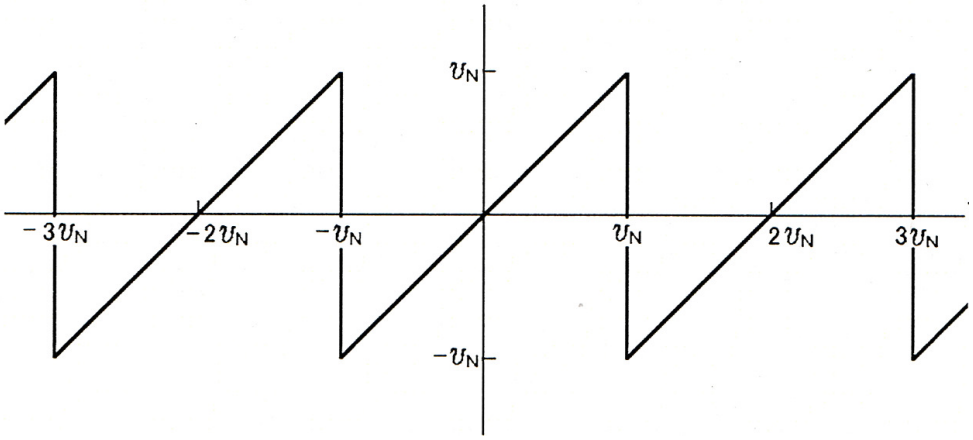

FIGURE 1.9: Doppler velocity aliasing.

The values of V_{r} are related by the following equation

$$V_{\mathrm{r}} = V_{\mathrm{d}} + 2v_{\mathrm{N}}, \tag{1.30}$$

where the integers $N(= 0, \pm 1, \pm 2, ...)$ are Nyquist numbers, and $2v_{\mathrm{N}}$ is the Nyquist width.

1.2.4.3 The maximum observation range

The maximum observable range r_a is

$$r_a = \frac{cT_s}{2}. \tag{1.31}$$

From (1.29) and (1.31), v_N is related to r_a by

$$v_N r_a = \frac{c\lambda}{8}. \tag{1.32}$$

Equation (1.32) shows that the produce of v_N by r_a becomes a constant value, and both v_N and r_a cannot be enlarged at the same time. In general, r_a is limited in order to enlarge v_N for suppressing the occurrence of velocity aliasing.

1.2.5 Atmospheric radars operated at VHF and UHF bands

As described in Section 1.1.1, ARs usually operate at VHF or UHF bands. The advantages of ARs operated at VHF band include the following:

- In precipitation region, lower VHF band ARs can receive Bragg scatterings from refractive index irregularities (clear-air echoes) and Rayleigh scatterings from hydrometeors (hydrometeor echoes) simultaneously. Therefore, lower VHF band ARs are useful for measuring vertical air velocity (W) of both the clear air and the precipitation (e.g., *Balsley et al.* [1988]; *Cifelli and Rutledge* [1994]; *Mega et al.* [2012]; *Nishi et al.* [2007]; *Rao et al.* [1999]; *Vincent et al.* [1998]).

- Measurement of the vertical gradient of the vertical velocity gives the divergence of the wind field, especially in storm conditions when the vertical motions and gradients are large.

- VHF ARs are unlikely to suffer the problems with contamination by bird and bat echoes that UHF ARs often encounter [*Barth et al.*, 1994; *Wilczak et al.*, 1995].

- When combination of radio and acoustic techniques in a single RASS system, VHF ARs have a better height coverage than a similar UHF system because the lower-frequency sound waves suffer much less attenuation.

However, effects such as long recovery times in transmit-receive systems and reflections or ringing in antennas and transmission cables mean that VHF band ARs generally cannot make measurements in the lowest 1 – 2 km of the atmosphere. Compared with VHF ARs, the lowest measurement height for UHF ARs can be as low as ∼100 m. The UHF ARs can attain fine range resolution more easily than the VHF ARs. For example, a range resolution of 75 m requires a transmitted pulselength of 0.5 μs and a corresponding bandwidth of about 2 MHz, which is very difficult to use at the VHF band. As described in Section 1.2.3, UHF ARs have higher sensitivity for hydrometeors. Therefore, UHF ARs can be used for hydrometeors measurement (e.g., *Gage et al.*, [1994]; *Rao et al.*, [2008]; *Tabata et al.*, [2011]; *Williams et al.*, [1995]). By using a 1357.5-MHz boundary layer radar (BLR), *Hashiguchi et al.* [1995a] and [1995b] measured the diurnal variations of the ABL in Serpong, Indonesia and Shigaraki, Japan, respectively. The measurement indicates that UHF ARs are useful for measuring the variations of the PBL both in clear atmosphere and precipitation atmosphere.

1.2.6 Factors that affect the measurement accuracy

Noise considerations are often unimportant for weather radars that observe storms, because the signal power is much larger than noise. However, when ARs are used to measure wind in clear air, the noise contributions from components (such as transmission lines, radomes, or the T/R switch) between the receiver and scatterer have paramount importance because the echo power can be smaller than the noise power.

Clutter refers to echoes that might interfere with desired signals. The name is descriptive because such echoes "clutter" the radar display and impede recognition of wanted images. For radars designed to detect objects such as aircraft, weather clutter is a nuisance that often obscures observation. On the other hand, the weather clutter contains the needed meteorological information, and for weather radars,

ground clutter and echoes from aircraft, birds, et cetera, obscure meteorological observation; consequently we reserve the term clutter for such interfering echoes. Because the clutter affects the measurement accuracy of signal-to-noise ratio (SNR), Doppler velocity and other parameters. The clutter must be suppressed for accurate measurement.

1.3 Signal processing techniques

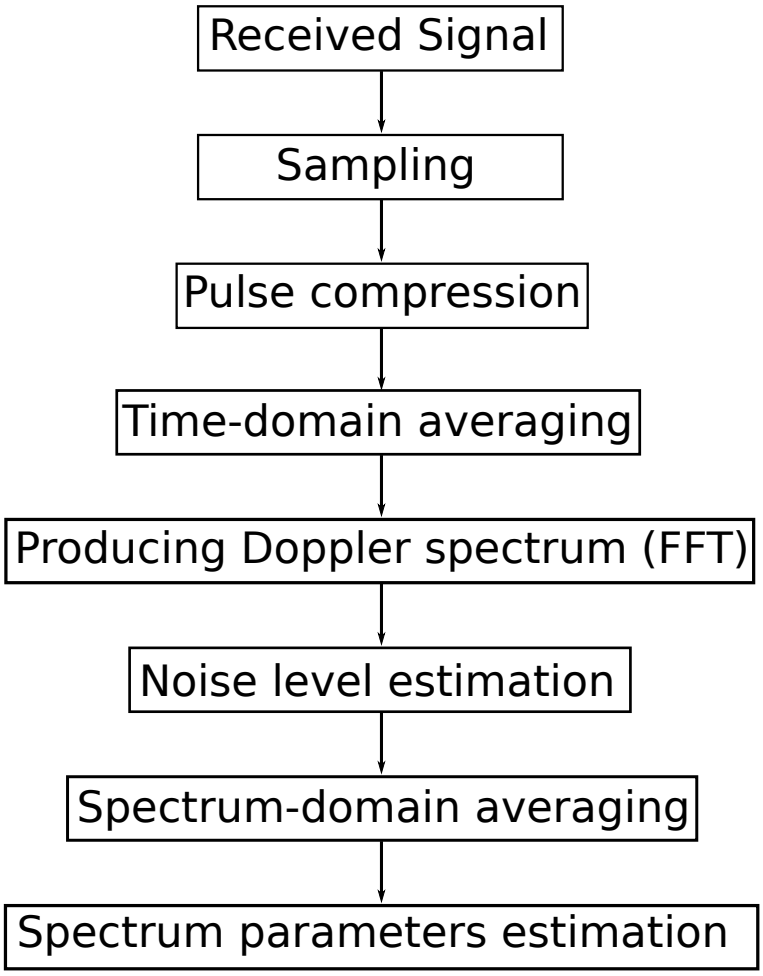

FIGURE 1.10: Flow diagram of a typical digital signal processing.

Figure 1.10 shows a flow chart of signal processing for ARs. First, a received signal is sampled. Sampling is the conversion of a continuous signal to a discrete signal. After the sampling, demodulation of pulse compression is carried out. The demodulated signal is averaged to minimize the effect of noise (coherent integration). Then,

a Doppler spectrum is created by using fast Fourier transform (FFT). FFT is an algorithm to convert a time series to a Doppler spectrum. Compared with discrete Fourier transform (DFT), FFT is much faster. After FFT, the Doppler spectrum can be averaging to reduce the effect of noise further (incoherent integration). Finally, the noise intensity, spectral parameters of the signal can be calculated. In this section, several techniques for signal processing are introduced.

1.3.1 Coherent integration

The ratio of received signal power from scatterers to noise power is called the SNR. For a received signal, coherent integration are usually used to improve the SNR. Because correlation time of the signal is much longer than the PRT in the lower and middle atmosphere, signals are coherent over a time interval which is shorter than the signal's correlate time. When N_{coh} sets of complex received signals are coherently added, noise power becomes N_{coh} times as large because white Gaussian noise samples are incoherent and change randomly from sample to sample. However, power of received signals becomes N_{coh}^2 times. Therefore, SNR is improved as

$$10 \log_{10} \frac{N_{\mathrm{coh}}^2}{N_{\mathrm{coh}}} = 10 \log_{10} N_{\mathrm{coh}} \quad [\mathrm{dB}]. \tag{1.33}$$

By using the coherent integration, the signal processing load can be reduced. When using FFT to produce the Doppler spectrum, the FFT points can be reduced by the coherent integration. For example, when the FFT points of 4096 is reduced to 128 by 32 times of coherent integration, the FFT calculation time is reduced by approximately 1/55.

Gage and Balsley [1978] defined the detectability D of the received signal in terms of $\overline{S}_{\mathrm{S}}$ (i.e., the spectral peak of the received signal density after averaging) relative to $\overline{\Delta S_{\mathrm{n}}}$ (i.e., the noise fluctuation level after averaging) as

$$D = \frac{\overline{S}_{\mathrm{S}}}{\overline{\Delta S_{\mathrm{n}}}} \tag{1.34}$$

By using N_{coh} times coherent integration, even the SNR is improved $10 \log_{10} N_{\mathrm{coh}}$ dB, D is not improved.

The pulse repetition time T_s is proportional to N_{coh}. Therefore, as shown in (1.29), the Nyquist limiting is proportional to N_{coh}^{-1}. Thus, the use of coherent integration should consider the required Nyquist velocity v_N. Further, the use of coherent integration would introduce more contamination signals by frequency aliasing.

1.3.2 Incoherent integration

In frequency domain, the power spectrum produced by FFT still has a statistical fluctuation. Averaging (or integration) of Doppler spectra which are independent with each other is indispensable to obtain precise amplitude and phase information. Such averaging processing in the frequency domain is called incoherent integration. By using N_{icoh} times of incoherent integration, statistical fluctuation of the Doppler spectrum becomes smaller by $1/\sqrt{N_{icoh}}$. Therefore, D becomes $\sqrt{N_{icoh}}$ times larger. However, the use of incoherent integration downgrades the time resolution of ARs.

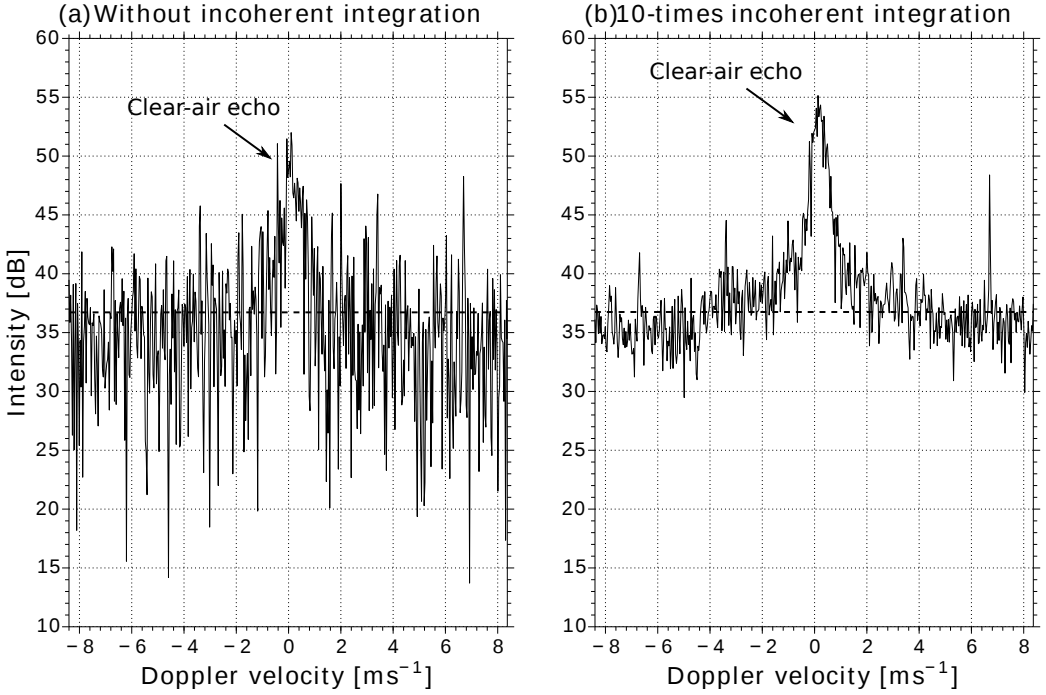

FIGURE 1.11: Doppler spectra collected by a VHF AR. The panels (a) and (b) show Doppler spectra without incoherent integration and with 10-times incoherent integration, respectively.

Figures 1.11 (a) and (b) show Doppler spectra collected by a VHF AR without incoherent integration and with 10-times incoherent integration, respectively. For

the Doppler spectrum processed without incoherent integration (Figures 1.11 (a)), the echo intensity varies from ∼14 dB to ∼52 dB. By using 10-times incoherent integration, the perturbation of the Doppler spectrum reduces much (Figure 1.11 (b)). The echo intensity varies from ∼29 dB to ∼55 dB. Because the perturbations reduce much, the peak of clear-air echo becomes clearer and more significant.

1.3.3 Pulse Compression

Besides the coherent integration and the incoherent integration performed at the receiver of a AR, several methods (i.e., increasing peak transmitted power, expand transmitted pulse width) can be used for improving SNR at the transceiver of a AR. However, there is limitation in transmitter devices to increase peak power. Furthermore, expansion of pulse width degrades range resolution. Therefore, a pulse compression technique is introduced for improving SNR. The basic concept of the pulse compression is to apply appropriate phase modulation on a long transmitted pulse and then demodulate and decode the received signal to obtain an equivalent echo sample having a much higher peak power than that transmitted, and having significantly better range resolution than that of the long transmitted pulse if it was not coded.

To compress a long pulse into a short one in the transmitter, the easiest method is to modulate a waveform that is uncorrelated in time but known at the receiver. A crosscorrelation operation at the receiver will compress the longer receiver waveform into a shorter one. This is due to the autocorrelation properties of the transmitted waveform, which is maximum at zero-lag and almost zero at lags other than zero. Generally, the pulse compression can be obtained by implementing the following procedures.

(1) Generate a modulated long pulse width signal as a transmitted pulse where the modulation signal is a quasi-random signal that has a very narrow auto-correlation function. In this stage, the frequency spectrum of the generated signal is spread and the phase is not aligned.

(2) In the receiving process, perform demodulation by applying cross-correlation between the detected received signal and the modulation signal which was adopted to generate the transmitted pulse.

The code modulation method is widely used in ARs. In the code modulation method, the transmitted radio-frequency pulse (rf pulse) is divided into N time slots and the phase of the transmitted pulse is changed at the beginning of each time slot. The binary phase coding which can perform phase modulation digitally by 180° is the most practical method. In this method, the phase $+(0°)$ or $-(180°)$ is applied to the transmitted pulse at each of N slots. In the reception, to decode the signal, the cross-correlation is performed between the detector output signal and phase modulated code series. The range resolution and the amplitude of the decoded signal become $1/N$ and N times, respectively, compared with original signal, and almost all the rf power in the pulse is transferred to one slot. At this time, the pulse compression ratio is N and the rf power of the signal becomes N^2 times larger. On the other hand, as the noise has no correlation to each other, the noise power of N samples becomes N times that of the original noise power. Thus, SNR is improved N times.

In a N bits binary phase code series, the unit amplitude signal series is expressed as

$$(X_1, X_2, ..., X_{\mathrm{N}}), \tag{1.35}$$

where $X_{\mathrm{i}} = 1$ or -1. The autocorrelation function $\Omega(k)$ can be given by

$$\Omega(k) = \sum_{i=1}^{N-|k|} X_i X_{i+|\mathrm{k}|}, \quad k = -(N-1), ..., (N-1). \tag{1.36}$$

The above function is an even function which is symmetric around $k = 0$. Generally, the autocorrelation function of binary phase code series does not become a single pulse of width N because there are residual signals, called range sidelobes, before and after the peak signal. In order to suppress sidelobes, several phase code series (i.e., Barker codes, Complementary codes, etc.) are proposed.

By using pulse compression, the capability for detecting weak echoes is improved. However, a minimum detectable range (or minimum altitude) is generally limited.

As the long pulse is transmitted, the transmitted pulse and backscattered signal intermingle up to the distance which is equivalent to the pulse duration from the radar. Thus, the correlation processing in demodulation in this region is not possible, and the perfect decoding of received signal cannot be performed. This time region is called truncated range. In the truncated range, the gain corresponding to the compression ratio cannot be obtained, and unnecessary range sidelobes are generated. *Spano and Ghebrebrhan* [1996a] and [1996b] proposed a phase codes (Spano codes) which can deal with low altitude observations as well as observations at high altitude.

Pulse-strings $P_{\mathrm{k}}, k = 0, 1, ..., S-1$ are S continuously transmitted pulses which have amplitude of 1 as shown in Figure 1.12.

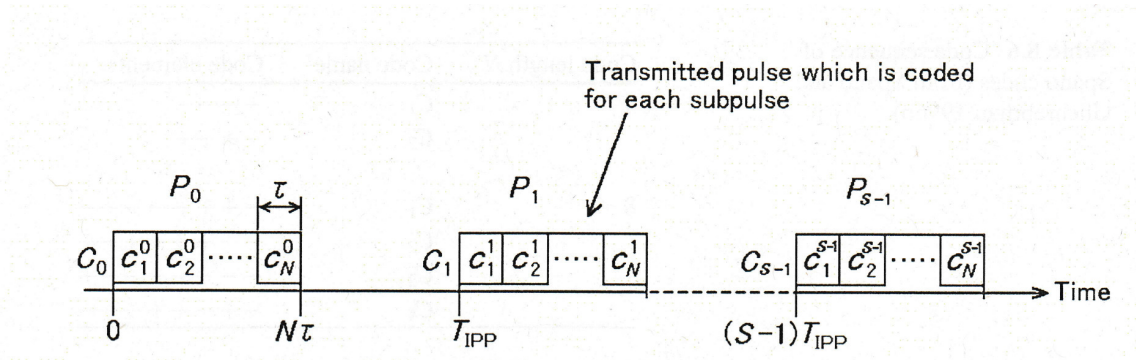

FIGURE 1.12: A train of S continuous pulses P_{k} ($k = 0$ to $S-1$) of identical pulse width and amplitude 1 coded by code sequence C_{k}, respectively (from [*Spano and Ghebrebrhan*, 1996b]).

Each pulse-string is composed of N subpulses of the same length. As shown in the same figure, the phase modulation of $c_{\mathrm{k}}^{\mathrm{j}}$ (0° or 180°) is applied to each transmitted subpulse by the code series C_{k}. In the reception, I and Q signals are sampled at the range gates $G_1, G_2, ..., G_{\mathrm{R}}$ in the time period of τ, respectively. The N-bits phase modulated signal is obtained in each gate as shown in Figure 1.13. Thus the backscattered signal for each gate is composition of received signals for N subpulses.

If sampled complex data series for kth transmitted pulse are $v_1^k, v_2^k, ..., v_N^k, ..., v_R^k$, and the decoded complex data series are $w_1^k, w_2^k, ..., w_N^k, ..., w_R^k$, then w_j^k is given by

$$w_j^k = \begin{cases} \sum_{m=1}^{j} c_{m+N-j}^k v_m^k & 1 \le j \le N-1 \\ \sum_{m=1}^{N} c_m^k v_{m-N+j}^k & N \le j \le R \end{cases}, \tag{1.37}$$

where $w_1^k, w_2^k, ..., w_{N-1}^k$ are signals in the truncated range.

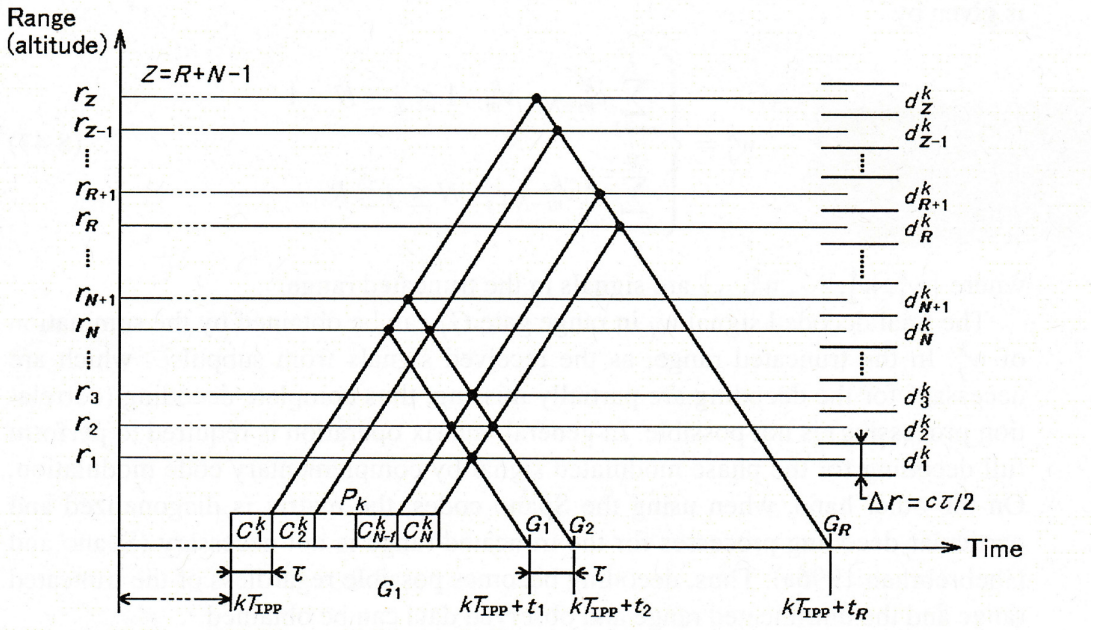

FIGURE 1.13: The in-phase and the quadrature components of the received, demodulated, and filtered signals are sampled by R range gates $G_1, G_2, ..., G_R$ with a time period τ (from [*Spano and Ghebrebrhan*, 1996b]).

The final decoded signal w_j in range gate G_j can be obtained by the summation of w_j^k. In the truncated range, as the received signals from subpulses which are necessary for the decoding are partially missing, thus complete decoding is not possible. In general, matrix operation is required to perform full decoding for the phase modulated signal by complementary code modulation. On the other hand, when using the Spano code, the matrix is diagonalized and particular decoding processes for the truncated range is not necessary. Thus, decoding becomes possible regardless of the truncated range and the untruncated range and observed data can be obtained.

Besides the code modulation method, linear frequency modulation (FM Chirping) can be used to do the pulse compression. The concept of FM Chirping is that the frequency of transmitted rf pulse linearly changes within a frequency bandwidth (Δf). For a transmitted rf pulse with pulse width of T, the peak power of the demodulated received signal is $T\Delta f$ times lager.

1.3.4 Noise estimation

Total noise of a receiver is the sum of external noise which enters through the antenna from the surrounding environment, antenna noise which is generated in the antenna, feeder noise which is caused in the path from the antenna to the receiver, and the receiver noise which is generated inside the receiver. It is noted that both external and internal noise are white noise. Noise from cosmic, atmospheric, and atmospheric absorption are the major external noise. Cosmic noise is radiated from the Galaxy, extragalactic nebulae, discrete radio sources and so on. Therefore, the noise intensity depends on the direction of the antenna beam; it becomes the maximum in the direction of the Galactic center while the minimum in the direction of its pole. Atmospheric noise due to lightning predominates in the frequency band below high frequency (HF; 3 – 30 MHz). Solar noise is a strong noise source, and sometimes increases by several figures with solar flares and so on. However, solar noise does not become a serious problem except if the radar beam points in the direction or vicinity of the sun. Ground noise also received by the antenna because part of the total antenna pattern is directed toward to the ground.

At the antenna, thermal noise which is caused by the lossy circuit in the antenna, and in the radome if equipped, is added to the noise from sky and ground. Thermal noise is additionally generated because of the power attenuation through the feeder lines such as waveguides and coaxial cables from the antenna to the feeder lines. In the receiver, the electric current flows through the electronic circuit is another source of thermal noise.

For estimating the average noise level, an objective method developed by *Hildebrand and Sekhon* [1974] is widely used. The method has the following steps:

(1) For a received Doppler spectrum $S(n), n = 1, 2, 3, ..., N$, a maximum intensity of the spectrum (p_{k}) is found. A threshold (T_{hr}) is set to p_{k} at first.

(2) Doppler spectrum points which have intensity smaller than T_{hr} are selected ($S(n), n = 1, 2, 3, ..., N^{'}$).

(3)

$$P = \frac{\sum_0^{N^{'}} S(n)}{N^{'}}, \tag{1.38}$$

$$Q = \frac{\sum_0^{N^{'}} S(n)^2}{N^{'}} - P^2 \tag{1.39}$$

and

$$R = \frac{P^2}{Q} \tag{1.40}$$

are calculated.

(4) If $R < 1$, smaller T_{hr} is calculated (e.g., $T_{\mathrm{hr}} = T_{\mathrm{hr}} - S$). S is the decrease step of T_{hr}. Then, return to (2) until $R \geq 1$.

When the condition that $R \geq 1$ is met, Doppler spectrum points which have intensity smaller than the determined T_{hr} are summed up as the noise level. In the following study, the noise level is calculated by using this method.

1.3.5 Spectral parameters estimation

For returned signals, we can assume that the power spectrum of the signal follows Gaussian distribution [*Yamamoto et al.*, 1988] (hereafter Y88) as

$$S(f) = \frac{P}{\sqrt{2\pi}\sigma} \times \exp(\frac{-(f - f_{\mathrm{d}})^2}{2\sigma^2}), \tag{1.41}$$

where f is the frequency and P, f_{d}, and σ are echo power, mean Doppler shift, and spectral width, respectively.

Previous studies have developed and evaluated methods for estimating P, f_{d}, and σ (e.g., *Le Foll et al.* [1997]; *Lottman et al.* [1997]; *Sato and Woodman* [1982]; *Woodman* [1985]; Y88). In general, two methods are used for calculating the three

parameters: a moment method and a least squares fitting method. For the moment method, the zeroth, first, and second moments of the spectral density correspond to P, f_{d}, and σ, respectively. For a received Doppler spectrum $S^{'}(f_{\mathrm{i}})$ obtained at M discrete frequencies f_{i},

$$P = \sum_{i=1}^{M} S^{'}(f_{\mathrm{i}}) \tag{1.42}$$

$$f_{\mathrm{d}} = \frac{1}{P} \sum_{i=1}^{M} f_{\mathrm{i}} S^{'}(f_{\mathrm{i}}) \tag{1.43}$$

$$\sigma = \sqrt{\frac{1}{P} \sum_{i=1}^{M} (f_{\mathrm{i}} - f_{\mathrm{d}})^2 S'(f_{\mathrm{i}})} \tag{1.44}$$

For the least squares fitting method, a Gaussian spectrum is fitted to the observed one so as to minimize the squared sum of the residual

$$\epsilon^2 = \sum_{i=1}^{M} [S^{'}(f_{\mathrm{i}}) - S(f_{\mathrm{i}}; P, f_{\mathrm{d}}, \sigma)]^2 \tag{1.45}$$

by changing the parameters P, f_{d}, and σ.

Y88 compared the performance of the moment method and that of the least squares fitting method and indicated that the moment method has better performance than the least squares fitting method if SNR is sufficient. Further, the least squares fitting method causes slightly underestimation of spectrum width. The least squares fitting method needs to determine the initial values of P, f_{d}, and σ and a threshold for finishing the iterations. The initial values and threshold raise a problem in regards to how they are determined; their robust determination is difficult because measured spectral parameters have large variability. Conversely, the moment method requires only the determination of the Doppler spectrum points that are used for calculating the parameters. The simplicity of the moment method also enables easy and practical assessments of the estimation errors of P, f_{d}, and σ.

Figure 1.14 shows an example of calculated P, f_{d}, and σ. Half-power full spectrum width ($\sigma_{3\mathrm{dB}}$) is defined as the one where a power spectral density is half of the maximum power. $\sigma_{3\mathrm{dB}}$ can be calculated by $\sigma_{3\mathrm{dB}} = 2\sqrt{2 \ln 2} \times \sigma$. By using (1.27),

Doppler velocity (V_{d}) can be calculated. In the following study, P, V_{d}, and σ_{3dB} are defined as spectral parameters.

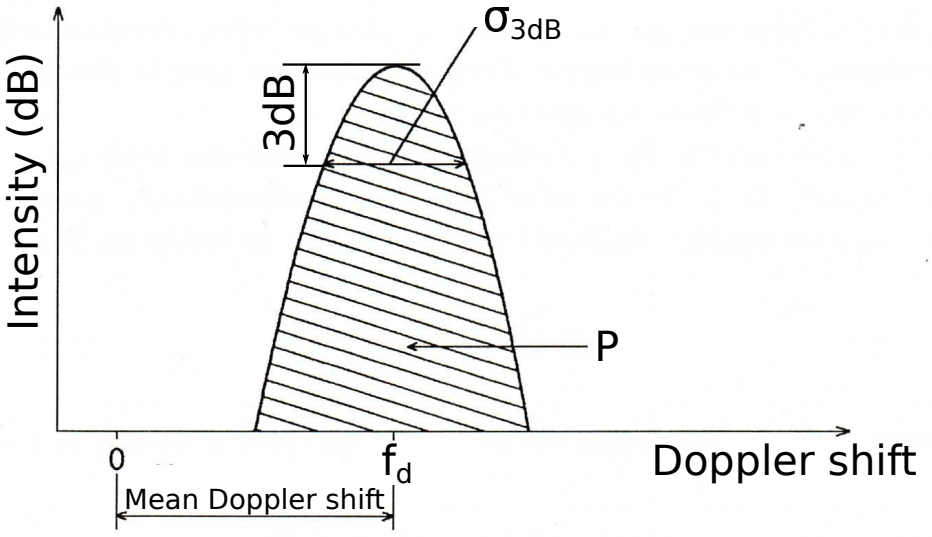

FIGURE 1.14: Spectral parameters of an atmospheric echo.

1.4 Overview and structure of this thesis

Wilson [2004] introduced techniques for retrieving turbulence parameters (e.g., dissipation rate). Therefore, the fine range resolution contributes better calculation accuracy. However, many ARs have the range resolution greater than 100 m which is determined by their transmitted pulse width. In order to measure the vertical structure of turbulence, ARs with the fine range resolution should be used with improve accuracy. A new digital receiver to support high-resolution observation was developed with software defined radio technique. In the high-resolution observation, the range interval and time interval are as small as several tens of meters and several tens of seconds or less, respectively. Therefore, a huge amount of data needs to be processed in high-resolution observation. In this study, we propose simple and robust computation methods to improve the estimation accuracy.

This thesis is divided into five chapters. **Chapter 1** introduces the related theories including the radar measurement of the atmosphere, basics of radars, and signal processing techniques for radars.

Chapter 2 describes observation techniques for precipitation and advances of techniques to improve radar resolution. The principles of radar imaging technique are introduced. Further, the development of a high-resolution digital receiver for a 1.3-GHz AR is described.

Chapter 3 describes methods for calculating the spectral parameters of clear-air echo in the clear air region. Using numerical simulation, methods for calculating the spectral parameters from Doppler spectra collected by high-resolution ARs are investigated. By using the method we proposed, Doppler spectral collected by the 1.3-GHz AR were processed.

Chapter 4 describes methods (top method and two-echo method) for calculating the spectral parameters of clear-air echo in the precipitation region. By using numerical simulation and measurement results obtained by the vertical beam of the MU radar during a precipitation event on 26 October 2009, the performance of the top and two-echo methods are evaluated.

Chapter 5 provides a summary of the thesis. The concepts of the methods are highlighted in this chapter.

Chapter 2

Recent advances in radar resolution enhancement

2.1 Radar observations of precipitation

Among various physical quantities which are measured with atmospheric radars, precipitation is widely considered as an important quantity from the viewpoint of the practical use. In this section, we discuss the relation between the basic radar quantities including radar reflectivity factor (Z), mean Doppler frequency, and mean Doppler spectrum width, and the drop size distribution (DSD). Then, we describe the specific techniques to derive these physical parameters from the basic radar quantities.

2.1.1 Parameters of precipitation

Precipitation particles include raindrops, graupels, hails, clouds, fogs, and so on. Thus, meteorological radars, in general, choose the wavelengths where the Rayleigh approximation becomes effective. Because the radar cross section σ is proportional to the sixth power of particle diameter (see 1.14), the rainfall rate is related closely to the DSD when rainfall rate is given as the function of σ (or radar reflectivity factor). A variety of functions have been so far proposed for the DSD, and among

them, the following gamma distribution is known as the most popular one which expresses a general DSD (e.g., *Ulbrich* [1983]; *Willis* [1984]).

$$N(D) = N_0 D^{\mu} \exp(-\Lambda D) \tag{2.1}$$

This distribution depends on three parameters, N_0, μ, and Λ. If small drop size is predominant and the distribution monotonically decreases as drop size becomes large, the values of $\mu \leq 0$ fit better. On the other hand, when a specific drop size which is not the minimum diameter is predominant, the values of $\mu > 0$ represent the distribution better [*Ulbrich*, 1983]. Theoretical models of the DSD generated by breakup and coalescence have been presented by e.g., *Srivastave* [1967] and [1971].

The parameter N_0 is an intercept parameter of the distribution curve, and its unit becomes $\mathrm{m}^{-1-\mu}\ \mathrm{m}^{-3}$ if the unit of diameter is expressed in meter. The parameter Λ is a slope parameter which shows the gradient of distribution curve. When $\mu = 0$, $N(D)$ becomes an exponential distribution expressed as [*Marshall and Palmer*, 1948]

$$N(D) = N_0 \exp(-\Lambda D). \tag{2.2}$$

The Marshall-Palmer (M-P) distribution belongs to the group of (2.2) with the following values for N_0 and Λ:

$$N_0 = 8.0 \times 10^6\ \mathrm{m}^{-1}\ \mathrm{m}^{-3}, \Lambda = 4100 R^{-0.21}\ \mathrm{m}^{-1}, \tag{2.3}$$

where R is the rainfall rate with a unit of mm h^{-1}.

It is convenient to use the higher moment of the DSD to express various physical quantities of precipitation. The nth moment of $N(D)$ is defined as

$$m_{\mathrm{n}} = \int_0^{\infty} D^{\mathrm{n}} N(D) dD. \tag{2.4}$$

Although the actual integral range is between $D_{\min}$ and $D_{\max}$, it is generally assumed, for simplicity, that $D_{\min} = 0$ and $D_{\max} = \infty$. The error caused by this approximation can be ignored to practical use. We adopt the following formula

which is useful in expressing the DSD [*Doviak and Zrnić*, 2006]

$$\int_0^\infty x^{\mathrm{a}-1} exp^{-\mathrm{bx}} dx = \frac{1}{b^{\mathrm{a}}}\Gamma(a), \tag{2.5}$$

where $a > 1$ and $b > 1$. The function Γ is the complete gamma function, and $\Gamma(n+1) = n\Gamma(n)$. If n is an integer, $\Gamma(n+1) = n!$. Substituting (2.1) into (2.4) and utilizing (2.5), the nth moment of the DSD can be expressed as

$$m_{\mathrm{n}} = N_0 \frac{\Gamma(n+\mu+1)}{\Lambda^{n+\mu+1}}. \tag{2.6}$$

Precipitation particles are falling at a constant speed in the atmosphere, which is determined by the balance between the downward force of gravity and the upward resistance exerted by the atmosphere. The speed is called the terminal velocity (w_{T}). A variety of formulae have been proposed to express w_{T} of the precipitation particles in the atmosphere. When the drop diameter D in the range around 3×10^{-4} m $< D < 6 \times 10^{-3}$m, $w_{\mathrm{T}}(D)$ can be expressed as [*Atlas et al.*, 1973]

$$w_{\mathrm{T}}(D) = 9.65 - 10.3\exp(-600D), \tag{2.7}$$

where w_{T} has a unit of m s^{-1}. The error from (2.7) has been confirmed less than 2% by comparison with the actual measurement in the range of drop diameter 6×10^{-4} m $< D < 5.8 \times 10^{-3}$ m. The more simplified expression is given by power law fit to the actual measurement as follows [*Atlas and Ulbrich*, 1977]

$$w_{\mathrm{T}}(D) \approxeq 386.6 D^{0.67}. \tag{2.8}$$

It is said that the above equation meets well with that actual measurement in the range 5×10^{-4} m $< D < 5 \times 10^{-3}$ m.

Theoretical terminal velocity of hailstones can be obtained through Newton's third law by equating the total drag force to the weight. [*Matson and Huggins*, 1980] determined the best-fit relationship between the diameter and terminal velocity of

hailstones with diameters less than 2.5×10^{-2} m as

$$w_{\mathrm{T}}(D) \cong 114.5 D^{0.5}. \tag{2.9}$$

As for aggregate snowflakes, [*Gunn and Marshall*, 1958] used the formula for

$$w_{\mathrm{T}}(D) \cong 8.34 D^{0.31}, \tag{2.10}$$

where D is the diameter of a water sphere with the same mass as the snowflake less than 2.5×10^{-3} m.

2.1.2 Relations between basic radar parameters and DSD

2.1.2.1 Radar reflectivity factor and DSD

By using the gamma function, the relation between Z and DSD can be expressed as

$$Z = \int_0^\infty D^6 N(D) dD = m_6 = N_0 \frac{\Gamma(\mu + 7)}{\Lambda^{\mu+7}}, \tag{2.11}$$

where the units of Z, N_0, and Λ are $\mathrm{m}^6\ \mathrm{m}^{-3}$, $\mathrm{m}^{-1-\mu}\ \mathrm{m}^{-3}$, and m^{-1}, respectively. It is should be noted that N_0 has a physical interpretation for the exponential distribution, i.e., it is the number density per unit drop diameter. However, for the gamma distribution, as shown in (2.1), it depends on μ and does not seem to have any physical meaning.

2.1.2.2 Doppler velocity and DSD

The mean Doppler velocity $\overline{V_{\mathrm{d}}}$ in the vertical direction which is measured with ground based radar is expressed by the following equation as the sum of the terminal velocity w_{T} of precipitation particles and the vertical component w of the

background wind velocity, where the velocity away from radar is assume to be positive.

$$\overline{V_{\mathrm{d}}} = -\frac{\int_{D_{\min}}^{D_{\max}} w_{\mathrm{T}}(D) D^6 N(D) dD}{\int_{D_{\min}}^{D_{\max}} D^6 N(D) dD} + w. \tag{2.12}$$

Using the higher moment of (2.6) and the terminal velocity of (2.7), the equation (2.12) can be expressed as

$$\begin{aligned} \overline{V_{\mathrm{d}}} &= -\frac{\int_{0}^{\infty} (9.65 - 10.3e^{-600D}) D^6 N_0 D^{\mu} e^{-\Lambda D} dD}{\int_{0}^{\infty} D^6 N_0 D^{\mu} e^{-\Lambda D} dD} + w \\ &= -9.65 + 10.3\left(\frac{\Lambda}{\Lambda + 600}\right)^{\mu+7} + w. \end{aligned} \tag{2.13}$$

2.1.2.3 Spectrum width and DSD

The spectrum width for vertical direction σ_{w} can be expressed using the Doppler velocity V_{d} as

$$\sigma_{\mathrm{w}} = (\overline{V_{\mathrm{d}}^2} - \overline{V_{\mathrm{d}}}^2)^{1/2}. \tag{2.14}$$

If the background wind velocity can be ignored, it is possible to express σ_{w} of (2.14) as follows by using (2.6) and (2.7)

$$\begin{aligned} \sigma_{\mathrm{w}} &= \left[\left(\frac{\int_{0}^{\infty} w_{\mathrm{T}}^2 D^6 N(D) dD}{\int_{0}^{\infty} D^6 N(D) dD}\right) - \left(\frac{\int_{0}^{\infty} w_{\mathrm{T}} D^6 N(D) dD}{\int_{0}^{\infty} D^6 N(D) dD}\right)^2\right]^{1/2} \\ &= 10.3\left[\left(\frac{\Lambda}{\Lambda + 1200}\right)^{\mu+7} - \left(\frac{\Lambda}{\Lambda + 600}\right)^{2\mu+14}\right]^{1/2}. \end{aligned} \tag{2.15}$$

Equations (2.13) and (2.15) show that $\overline{V_{\mathrm{d}}}$ and σ_{w} are independent of N_0. It is suggested that these two parameters can determine μ and Λ. Above discussion shows that three basic radar parameters (Z, $\overline{V_{\mathrm{d}}}$, and σ_{w}) can be related with relative simple analytical equations to the three parameters of a gamma DSD.

2.1.3 Estimation of DSD

For precise estimation of the DSD, it is necessary to remove vertical motion of the background atmosphere from the observed velocity of precipitation particle. Therefore, in general, ARs which can directly measure vertical wind component simultaneously with precipitation particle velocity with higher precision are utilized. The relation between the normalized mean Doppler spectrum (power spectral density or power spectrum) $S_{\mathrm{p}}(w_{\mathrm{T}})$ of precipitation observed with a vertically pointed beam and $N(D)$ is derived by [*Doviak and Zrnić*, 2006]

$$S_{\mathrm{p}}(w_{\mathrm{T}})dw_{\mathrm{T}}(D) = \sigma(D)N(D)\frac{dD}{\eta}, \tag{2.16}$$

where σ is the backscatter cross section. Using the relation $\sigma(D)/\eta = D^6/Z$, (2.16) is expressed as

$$S_{\mathrm{p}}(w_{\mathrm{T}})dw_{\mathrm{T}}(D) = D^6N(D)\frac{dD}{Z}. \tag{2.17}$$

Thus, the power spectrum of a distribution of drops is expressed as

$$S_{\mathrm{p}}(w_{\mathrm{T}}) = \frac{D^6N(D)}{Z}/\frac{dw_{\mathrm{T}}(D)}{dD}. \tag{2.18}$$

Meanwhile, the power spectrum of atmosphere perturbation is assumed to following Gaussian function ([*Sato et al.*, 1990]),

$$S_{\mathrm{t}}(w) = \frac{1}{\sqrt{2\pi}\sigma_{\mathrm{w}}}\exp(-\frac{w^2}{2\sigma_w^2}), \tag{2.19}$$

where w is the mean wind velocity in the radar beam direction and σ_w is the spectral broadening.

If the rain drops completely follow the motion of atmospheric turbulence, the observed Doppler spectrum $S(v)$ due to the precipitation and atmosphere turbulence is expressed by

$$S(v) = P_{\mathrm{rp}}S_{\mathrm{P}}(w_{\mathrm{T}}) * S_{\mathrm{t}}(w) + P_{\mathrm{rt}}S_{\mathrm{t}}(w) + P_{\mathrm{n}}, \tag{2.20}$$

where P_{rp} and P_{rt} are echo power associated with precipitation and atmosphere turbulence, $*$ denotes convolution, P_{n} is the noise level on the spectrum.

The value of $S(v)$ is determined by seven parameters: echo intensity, vertical component of wind velocity, and spectrum width of the atmosphere turbulence, N_0, Λ, μ, and noise. In order to measure these parameters, the least squares fitting method is widely used (e.g., *Wakasugi et al.* [1986]; *Sato et al.* [1990], *Shibagaki et al.* [1997]). For the case only single VHF or UHF radar was used, the convolved term of (2.20) (hereafter referred as to S_{pt}) takes account of broadening of the reflectivity-weighted fall speed spectrum as a result of both clear air turbulence and falling raindrops. Then the least squares method is used to fit a function to the convolved term. For the case both VHF and UHF radars were used, the reflectivity-weighted fall speed spectrum $\hat{S_{\mathrm{P}}}$ can be retrieved from the UHF spectrum (spectrum collected by UHF radar) by subtracting the VHF spectrum (spectrum collected by VHF radar) [*Schafer et al.*, 2002]. The deconvolved reflectivity-weight fall speed spectrum is then estimated as

$$\hat{S_{\mathrm{P}}}(w) = \mathrm{SHIFT}_{-\overline{w}}(\mathrm{FFT}^{-1}[\frac{\mathrm{FFT}(S_{\mathrm{pt}}(w-\overline{w}))\Phi(w)}{\mathrm{FFT}(S_{\mathrm{t}}(w))}]), \tag{2.21}$$

where SHIFT denotes a shift by $-\overline{w}$ to remove any nonzero mean clear air vertical velocity, FFT represents the fast Fourier transform, FFT^{-1} represents the inverse of the fast Fourier transform, and Φ represents an optimal filter of the FFT. In this operation, the clear air velocity spectrum is known and determined from the VHF spectrum. Then, the least squares method is used to fit a function to (2.21).

2.2 Radar imaging technique

In radar interferometry, spaced receiver antennas are used to improve angular resolution, and multiple carrier frequencies are used to improve range resolution. The former is referred to as coherent radar imaging (CRI) or spatial domain interferometric imaging (SDI) (e.g., *Hassenpflug et al.* [2008]; *Palmer et al.* [1998]). The latter is referred to as range imaging (RIM) [*Palmer et al.*, 1999] or frequency interferometric imaging (FII) [*Luce et al.*, 2001]. In this section, the concepts of CRI and RIM are introduced.

2.2.1 Coherent radar imaging (CRI)

Figure 2.1 shows a conceptual drawing of CRI.

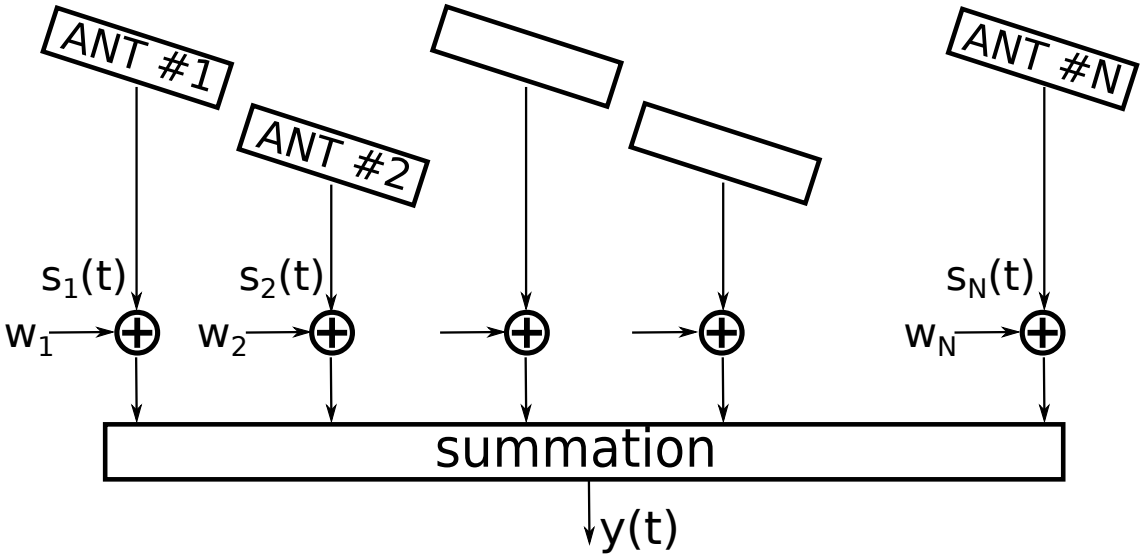

FIGURE 2.1: Conceptual drawing of coherent radar imaging (CRI).

In CRI, signals from spaced receivers are synthesized with appropriate weights in order to steer the radar beam in certain directions with improved angular resolution (e.g., *Woodman* [1997]). For CRI, the Capon method [*Capon*, 1969] is widely used because it satisfies both high angular resolution and simple calculation. Further, *Palmer et al.* [1999] indicated that the Capon method is extremely robust in that spurious artifacts are seldom seen in the range brightness estimates.

Hereafter, signal processing of CRI using the Capon method is described. $s = (s_1(t), s_2(t), ..., s_{\mathrm{N}}(t))^{\mathrm{T}}$ denotes a set of signals received by N spaced antennas, where t is the sampled time and T is the transpose operate. $w = (w_1, w_2, ..., w_{\mathrm{N}})^{\mathrm{T}}$ denotes a set of weights for summation. The optimal weight vector is given by a solution that minimizes the resulting average power B. B is expressed by

$$B = w^{\mathrm{H}} R w, \tag{2.22}$$

where H represents the Hermitian operator (conjugate transpose) and R is a covariance matrix given by

$$R = \begin{pmatrix} R_{11} & R_{12} & \dots & R_{1\mathrm{N}} \\ R_{21} & R_{22} & \dots & R_{1\mathrm{N}} \\ \vdots & \vdots & \ddots & \vdots \\ R_{\mathrm{N}1} & R_{\mathrm{N}2} & \dots & R_{\mathrm{NN}} \end{pmatrix}, \tag{2.23}$$

R_{ij} is a covariance between s_{i} and s_{j}. w is constrained by the condition of constant gain to waves coming from the target volume, and the constraint is given by

$$e^{\mathrm{H}} w = 1, \tag{2.24}$$

where

$$e = (e^{jk \cdot D_1}, e^{jk \cdot D_2}, ..., e^{jk \cdot D_{\mathrm{N}}})^{\mathrm{T}}, \tag{2.25}$$

k is the wavenumber vector of the focused direction with the zenith and azimuth angle of θ and ϕ, respectively. k can be calculated by

$$k = \frac{2\pi}{\lambda}[\sin\theta \sin\phi, \sin\theta \cos\phi, \cos\phi]. \tag{2.26}$$

D_{n} is the vectors which represent the center of each receiving for the nth receiver. As the solution of the constrained minimization problem, the optimal weight $w_{\mathrm{c}}(k)$ is given by

$$w_{\mathrm{c}}(k) = \frac{R^{-1}e}{e^{\mathrm{H}} R^{-1} e}. \tag{2.27}$$

Then, the filtered signal ($y(t)$) is given by

$$y(t) = w_{\mathrm{c}}^{\mathrm{H}}(k) s(t). \tag{2.28}$$

By calculating the Doppler spectrum of $y(t)$, echo power, Doppler velocity, and spectral width can be computed with improved angular resolution.

Using data collected by a VHF radar installed at Tourris, France (43.08°N, 6.01°E), [*Hélal et al.*, 2001] showed a fine-scale angular distribution of backscattered clear-air echo power using CRI. From a CRI measurement, *Pollard et al.* [2000] demonstrated that horizontal distribution of refractive index structure function is able to

be measured. *Cheong et al.* [2006] succeeded in separating clear-air echoes and the biological scattering which was moving in the grating-lobe region in a CRI measurement.

2.2.2 Range Imaging (RIM)

Figure 2.2 shows a conceptual drawing of RIM.

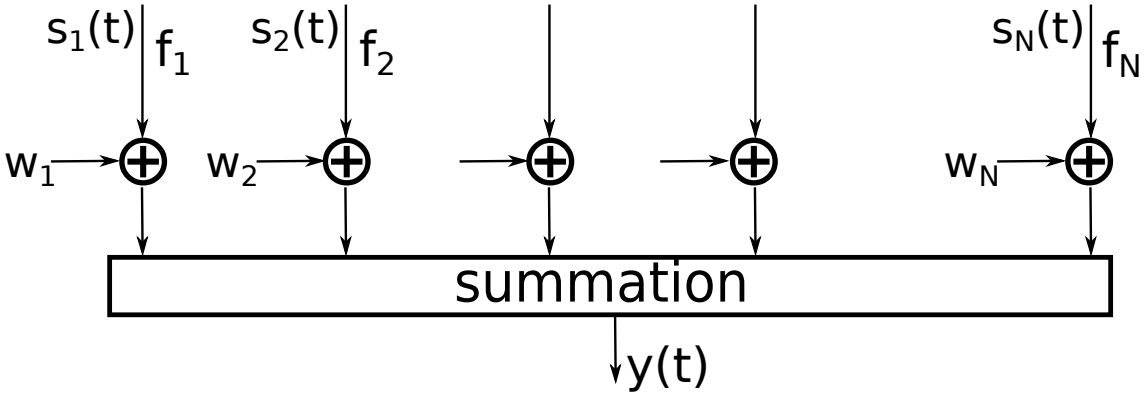

FIGURE 2.2: Conceptual drawing of range imaging (RIM).

In RIM, signals sampled from multiple frequencies are synthesized with appropriate weights in subranges within a range gate. Range imaging has advantages over the use of shorter transmitted pulse (i.e., the simplest technique to improve the range resolution) because RIM does not require improvements in the receiver sensitivity and it reduces spurious radio waves [*Chilson et al.*, 2003; *Yu et al.*, 2004]. Using the synthesized signal, echo power, Doppler velocity, and spectral width at each subranges are calculated in order to improve range resolution.

In RIM, the Capon method is widely used because it satisfies both high range resolution and simple calculation. s denotes a set of signals collected by N carrier frequencies that $s = (s_1(t), s_2(t), ..., s_{\mathrm{N}}(t))^{\mathrm{T}}$. Frequencies are switched on a pulse-to-pulse basis in order to maximize the correlation of signals sampled by different frequencies. Using numerical simulation, *Palmer et al.* [1999] showed that 3 or more frequencies are required for RIM measurements. The optimal weight vector is given as a solution that minimizes the resulting average power B_{r}. B_{r} is expressed by

$$B_{\mathrm{r}} = w^{\mathrm{H}} R w, \tag{2.29}$$

where w denotes a set of weights from summation that $w = (w_1, w_2, ..., w_{\mathrm{N}})^{\mathrm{T}}$, R is a covariance matrix as (2.23). w is constrained by the condition of constant gain to waves coming from the target, and the constraint is given by

$$e^{\mathrm{H}} w = 1, \tag{2.30}$$

where e is a range steering vector and given by

$$e = (e^{-j2k_1 r_1}, e^{-j2k_2 r_2}, ..., e^{-j2k_{\mathrm{N}} r_{\mathrm{N}}})^{\mathrm{T}}, \tag{2.31}$$

where k_{m} denotes the wavenumber of mth frequency, r_{m} is the range between the target and radar for different carrier frequencies. Because radar pulses with different carrier frequencies are transmitted almost at the same time so that the targets can be assumed to be constant in characteristics and their ranges are equal (e.g., $r_1 = r_2 = ... = r$). Therefore, (2.31) becomes

$$e = (e^{-j2k_1 r}, e^{-j2k_2 r}, ..., e^{-j2k_{\mathrm{N}} r})^{\mathrm{T}}, \tag{2.32}$$

For signals with a pair of frequencies, R can be calculated as

$$\begin{aligned} R_{\mathrm{mn}} &= < R_{\mathrm{m}} R_{\mathrm{n}}^{*} > = < A_{\mathrm{m}} \exp[j(-2k_{\mathrm{m}} r_{\mathrm{m}} + \phi_{\mathrm{m}})] \cdot A_{\mathrm{n}} \exp[j(2k_{\mathrm{n}} r_{\mathrm{n}} - \phi_{\mathrm{n}})] > \\ &= < A_{\mathrm{m}} A_{\mathrm{n}} \exp[j2(k_{\mathrm{n}} r_{\mathrm{n}} - k_{\mathrm{m}} r_{\mathrm{m}}) + (\phi_{\mathrm{m}} - \phi_{\mathrm{n}})] >, \end{aligned} \tag{2.33}$$

where $< \cdot >$ means ensemble average, ϕ_{m} and ϕ_{n} are the phase terms associated with the system responses to different transmitting frequencies. Because ϕ_{m} is determined not only by the total system delay throughout the transmitter and receiver chains but also the initial phase value. Therefore, the total system delay, from which the value of ϕ_{m} is computed, needs to be known. *Chilson* [2004] and *Palmer et al.* [2001] measured the initial phases of the carrier frequencies from the signals that were leaked from the transmitted signals back to the receiver by an ultrasonic delay line. (2.33) indicates that only the relative phase difference among different frequencies are necessary to calculate R. Therefore, by calculating the phase term of cross correlation between two time series of received signals measured at different frequencies, R can be calculated *Chen* [2004].

The optimal weight w_{rC} is given by

$$w_{\mathrm{rC}} = \frac{R^{-1}e}{e^{\mathrm{H}}R^{-1}e}. \tag{2.34}$$

Finally, the filtered time series $(y(t))$ can be calculated by

$$y(t) = w_{\mathrm{rC}}^{\mathrm{H}} s(t). \tag{2.35}$$

By applying RIM to a data collected by using 2 μs transmitted pulse, *Chilson et al.* [2004] produced Doppler velocity with 15-m range intervals and showed that the Doppler velocity produced by RIM agreed well with that measured with the 0.5 μs transmitted pulse. By applying RIM to the MU radar, the range resolution improved much. Figure 2.3 shows a time-height intensity plot of SNR in the vertical beam of the MU radar after RIM processing [*Luce et al.*, 2007]. The image reveals detailed structures of thin stratified layers, especially above 8 km, where a small tropopause fold is noticeable.

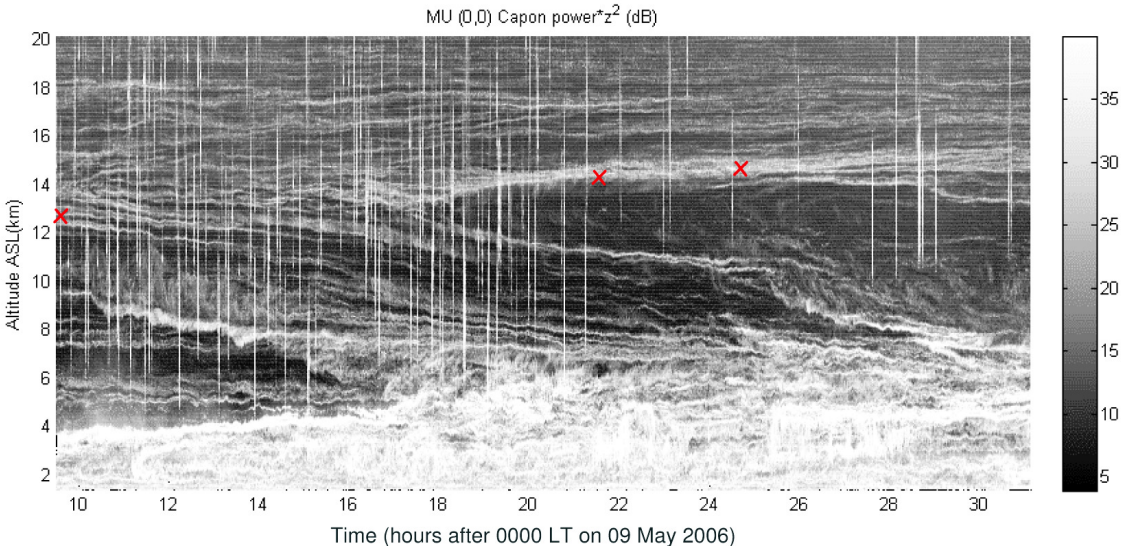

FIGURE 2.3: Time-height intensity plot of SNR after RIM processing with the MU radar. Vertical lines are airplane echoes and should not be considered (from [*Luce et al.*, 2007]).

2.3 Digital receiver for a 1.3-GHz high-resolution atmospheric radar (RIM LQ-7)

A small-sized BLR, using microstrip antenna technology to observe the wind velocities in the ABL, was first developed by *Ecklund et al.* [1988] and [1990] at Aeronomy Laboratory of National Oceanic and Atmospheric Administration in the United States. In 1992, Radio Science Center for Space and Atmosphere of Kyoto University (presently Research Institute for Sustainable Humanosphere, RISH) developed a 1357.5-MHz BLR. By using the BLR at Indonesia, *Hashiguchi et al.* [1995b] indicated that the observations with the BLR play an important role in various studies of the equatorial lower atmosphere. After the BLR, RISH developed a 1357.5-MHz Lower Troposphere Radar (LTR) for enabling observations of height profiles of wind velocity in the whole lower troposphere [*Hashiguchi et al.*, 2004]. The LTR combined the advantage of the transportability of the 1.3-GHz BLR with enlarged observable height range. The same radar system was adopted in a wind profiler network, the Wind Profiler Data Acquisition System (WINDAS), of the Japan Meteorological Agency ([*Ishihara and Goda*, 2000] and [*Kato et al.*, 2004]). Cooperated with Sumitomo Electric Industries, Ltd., RISH has developed the LQ-7 which uses Luneberg lense [*Sullivan*, 2000] in the antenna part. The use of Luneberg lens resulted into a big reduction in cost (∼40%), an expansion of observed height, an extension of system life, and an improvement in maintenance [*Imai et al.*, 2007]. The time and range resolution for the BLR are about 1 min and 100 m, respectively. For the LTR, different measurement parameters have different time and range resolution. The time and range resolution are generally greater than or equal to 61.4 s and 100 m, respectively. For the LQ-7, the time and range resolution are 10.6 s and 150 m, respectively.

Previous studies (e.g., *Luce et al.* [2010]; *Mega et al.* [2010]) indicated that RIM is useful for resolving turbulence and wind perturbations triggered by Kelvin-Helmholtz instability. Further, *Yu et al.* [2010] proposed RIM with adaptive clutter suppression by using both multiple receivers and multiple frequencies. It is hoped that the BLR can conduct RIM observations. RIM performs adaptive signal processing at every subgate to produce time series with high range resolution. When received signals are sampled with an interval that matches the transmitted pulse

width, the received signal intensity significantly decreases at the subgates near the edge of the sample volume in the range direction. This decrease in the received signal intensity is referred to as the range-weighting effect, and can significantly degrade the accuracy of RIM [*Chen and Zecha*, 2009]. Oversampling (OS) in the range direction, which samples received signals with range intervals smaller than that determined by the transmitted pulse width, is one way to overcome this difficulty. OS was also proposed for improving the range resolution for weather radar through adaptive processing [*Yu et al.*, 2006]. In this section, we show our recent development of a digital receiver. This digital receiver is developed for the existing LQ-7, and puts the capability of RIM and OS to the system (RIM LQ-7).

Currently, many radars perform real-time digital signal processing using digital boards that have field programmable gate array (FPGA) and/or digital signal processor (DSP) on-board. Such digital boards require high hardware cost. Further, software development for the boards is also expensive because it requires expertise in FPGA and DSP. It must be emphasized that because the expertise of vendors varies and the specifications of FPGAs and DSPs change, source codes developed for FPGAs and DSPs are difficult to re-use. Therefore, software development using popular programming languages and widely used libraries are necessary to ensure the re-usability of source code for the digital receiver. In this study, by using a general-purpose software-defined radio (SDR) receiver referred to as Universal Software Radio Peripheral 2 (USRP2) and a commercial personal computer (PC), we have developed a new radar digital receiver. The USRP2 is controlled from the PC using a Universal Software Radio Peripheral hardware driver (UHD). Software developed for the digital receiver was written in the C++ language. Software developed for the signal processing was written in the Python language.

Figure 2.4 shows a system block diagram of the RIM LQ-7. The RIM LQ-7 is developed based on the LQ-7. Figure 2.5 shows a picture of the LQ-7. It has a phased array antenna composed of seven Luneberg lenses with a diameter of 800 mm. The antenna gain is greater than 30 dBi. Each lens has five feeds directed toward the vertical and four oblique directions (north, east, south, and west) with a zenith angel of 14.2°, respectively. The beam direction is electronically switched. Below each lens, a transmission/reception switch and a radio frequency (RF) receiver unit including a low noise amplifier (LNA) are installed. Because each lens radiates 400

W radio waves, the total peak output power of the LQ-7 is 2.8 kW. The phased array antenna and outdoor unit of the LQ-7 are used for the RIM LQ-7. In order to switch the frequency for every transmission, five local oscillators, having frequencies of 1227.00, 1227.25, 1227.50, 1227.75, 1228.00 MHz, are installed.

The signal processing of the LQ-7 does not include the function of IF sampling. Further, the signal processing unit of the LQ-7 does not have the function necessary for real-time processing of RIM (i.e., decoding and integrating each of the received signals collected by the different frequencies) and Oversampling (OS). Therefore, we developed the new digital receiver for the RIM LQ-7 that comprises an IF amplifier and filter unit, a USRP2, and a PC. The received IF signals collected from each of the seven antenna elements are synthesized by a combiner. The synthesized signals are amplified, filtered with 3-MHz bandwidth, and then inputted to the USRP2.

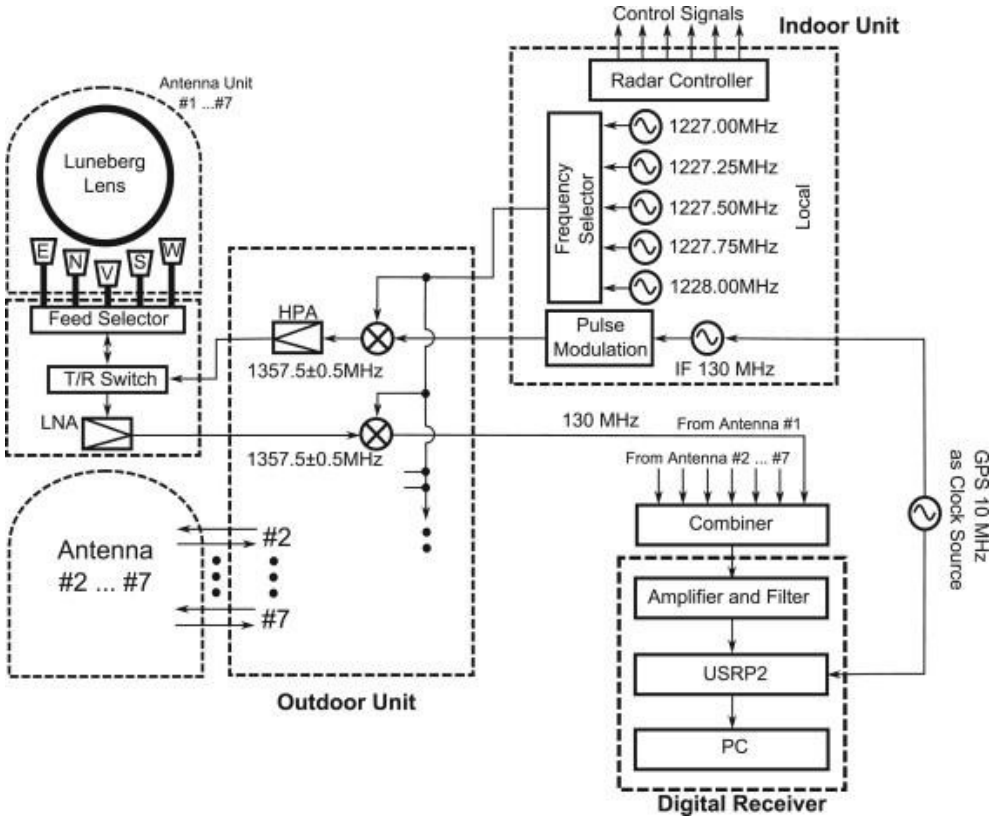

FIGURE 2.4: System block diagram of the 1.3-GHz range imaging wind profiler radar (RIM LQ-7) equipped with the digital receiver.

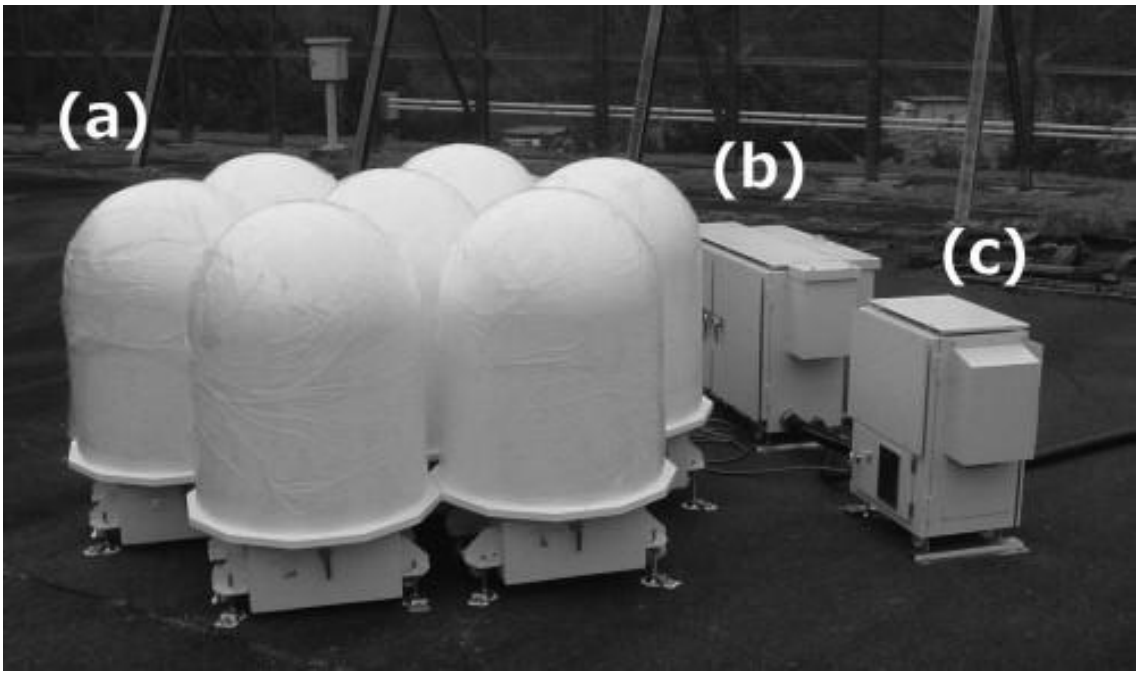

FIGURE 2.5: Picture of the (a) antenna, (b) outdoor unit, and (c) power supply unit of the RIM LQ-7.

Figure 2.6 shows a view of the USRP2 interface. As a reference signal, the 10-MHz signal from the GPS receiver is used. In order to synchronize the IF signal produced inside the USRP2, as well as that produced by the analog transmitter/receiver unit, the 10-MHz reference signal is branched into the REF clock terminal and the clock source of the IF oscillator. From the RF1 terminal, the USRP2 collects IF signals, digitizes them, and produces IQ time series by phase detection. From the GB ETHERNET interface, the IQ time series are transferred to the PC through Gigabit Ethernet. Note that the RF2 and PPS IN terminals are not used for the current receiver configuration. The resolution and maximum input voltage of the analog-to-digital converter of the USRP2 are 14 bits and 2 V peak-to-peak, respectively. The IF amplifier and filter unit were designed to match the input level of the USRP2. The dynamic range of the USRP2 is sufficient for the dynamic range of the LQ-7 (60 dB).

FIGURE 2.6: A view of the USRP2 interface.

Figure 2.7 shows the signal flow of the digital receiver. The USRP2 collects received IF signals and produces IQ time series. Then the IQ time series are transferred to the PC. In order to collect the IQ time series and perform other real time signal processing simultaneously, the PC uses multi-threading composed of Data Taking and Signal Processing threads. Data Taking collects the IQ time series and performs range sampling. At the start of data sampling, Data Taking creates Signal Processing. After its creation, Signal Processing waits for the start request from Data Taking. In order to avoid a memory conflict between Data Taking Thread and Signal Processing Thread, the shared memory is divided into two parts (i.e., double buffered). Signal Processing executes filtering in the range direction, decodes phase-modulated received signals, performs coherent integration, and finally saves the processed data in the external HDD.

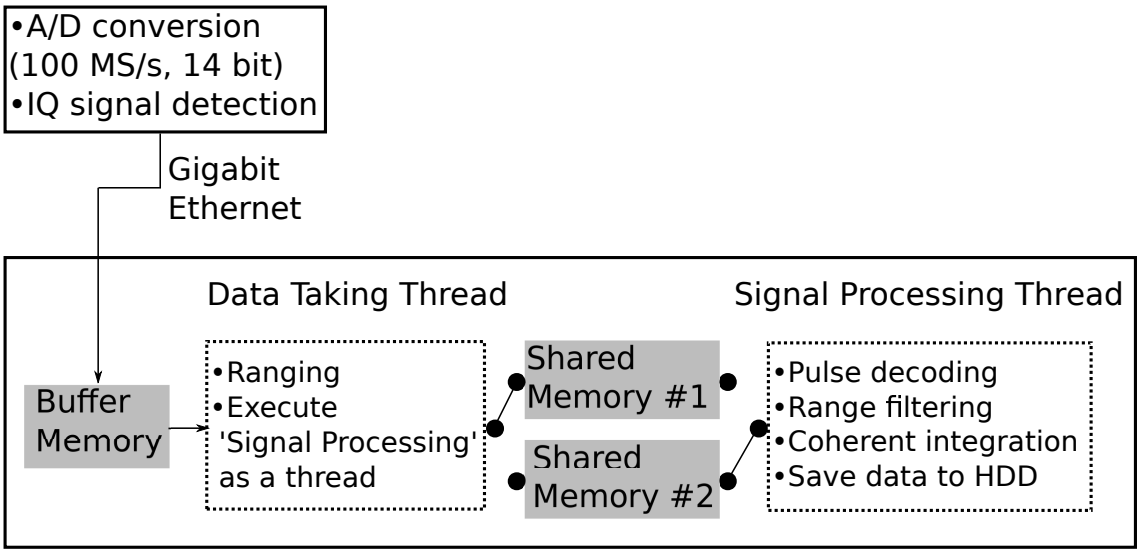

FIGURE 2.7: Signal flow of the digital receiver.

The USRP2 digitizes the 130-MHz IF signals with a sample rate of 100 MS s^{-1} and a resolution of 14 bit. In order to sample IF signals with a frequency higher than its sample rate (i.e., 100 MS s^{-1}), the USRP2 performs downsampling with a frequency of 30 MHz (= 130 MHz − 100 MHz). The downsampling works with sufficient accuracy for the RIM Lq-7. The USRP2 produces IQ time series by applying phase detection to the digitized signals. The IQ time series produced with a rate of 10 MS s^{-1} are transferred to the PC sequentially. The UHD uses User Datagram Protocol (UDP) for the data transfer and selects the data format of the IQ signals.

Data Taking collects the IQ time series sequentially transferred from the USRP2 and performs range sampling. In order to determine the start time of the range sampling, a leaked transmitted pulse is used. Because the intensity of the leaked transmitted pulse is much greater than that of the receiver noise and returned signals, it is safe to determine the onset of transmission using the leaked transmitted pulse.

The data sampled in the range direction are stored in the shared memory. Because we use a sample rate of 10 MS s^{-1}, the range sampling can have an offset of 15 m. However, the offset is sufficiently small that it can be ignored compared with the range uncertainties caused by signal delays in the transmitter, receiver, and cables.

The digital receiver is designed to decode any pulse patterns with binary phase (0° or 180°). The subpulse width must be multiples of 0.1 μs because we use the fixed sampling rate of 10 MS s^{-1}. The subpulse width constrain can be solved by varying the sample rate of the USRP2, and this sample rate variation function will be implemented in the future.

The degree of OS is limited by the sample rate of the IQ time series (i.e., 10 MS s^{-1}). For the 1-μs subpulse width, 10 times, 5 times, double, and no OS can be performed. Reducing the degree of OS helps to both reduce the amount of data saved in the external HDD and extend the upper limit of the range coverage.

Finally, Signal Processing performs coherent integration to reduce the amount of data and then stores the processed data in the external HDD, and then waits for the next start request from Data Taking.

It is noted that the synchronization between the digital receiver and the transmitter unit of the LQ-7 is ensured by using the leaked transmitted pulse. In addition to the ranging data, Data Taking transfers the sampled leaked transmitted pulse to Signal Processing through the shared memory. By verifying that the pulse pattern of the leaked transmitted pulse matches the pattern that is expected to be detected, Signal Processing confirms that Data Taking has correctly detected the onset of transmission. The verification confirmed that the digital receiver is able to make continuous measurements over several days or longer. In the following study, measurement results of the RIM LQ-7 are shown.

2.4 Discussion

As described in Sections 2.2.1 and 2.2.2, the use of CRI and RIM are useful for improving the angular resolution and range resolution, respectively. *Luce et al.* [2007] indicated that by using RIM, the range resolution of MU radar improved much which is useful for studying the detailed structures of the atmosphere. By using the digital receiver developed by using SDR (i.e., USRP 2), the radar imaging technique and OS are implemented in the 1.3-GHz AR (LQ-7) while the original receiver of the system could not perform these functions. SDR is a technique to implement functions of radiowave instruments by means of software on a personal computer or

embedded system. Then, with the digital receiver developed by using SDR, we can change the system parameters easily by changing the software setting. The use of the SDR technique will set a new paradigm in the AR system development.

In the high-resolution observation, the use of radar imaging technique can improve the range resolution down to several tens of meters. Thus, a huge number of Doppler spectra was collected. Therefore, the methods for calculating the spectral parameters should be simple and robust. In addition, the estimation accuracy of the spectral parameters should be kept high to ensure the correctness of the high-resolution observation.

As described in Section 1.3.5, the accurate detection of peak location is vital for accurate estimation of spectral parameters. For the moment method, the miss-determination of peak location causes the miss-selection of points used for calculation. For the least squares fitting method, the miss-determination of peak location causes the miss-fitting range. Therefore, determination accuracy of peak location must be investigated.

As described in Section 1.3.2, the use of incoherent integration downgrades the time resolution of ARs. The use of incoherent integration should be minimized in high-resolution observation. Therefore, a threshold for judging the necessary of incoherent integration should be proposed.

As described in Section 1.2.3, 50-MHz band ARs are useful for measuring vertical air velocity W in precipitation region. Further, the 50-MHz band ARs also have been used for measuring DSD (e.g., *Lucas et al.* [2004]; *May and Rajopadhyaya* [1996]; *Wakasugi et al.* [1986]). UHF ARs have higher sensitivity for hydrometeors than 50-MHz band ARs (e.g., *Gage et al.* [1994]; *Rao et al.* [2008]; *Tabata et al.* [2011]; *Williams et al.* [1995]). Previous studies showed that using both 50-MHz band and UHF ARs are useful for retrieving DSD (e.g., *Cifelli et al.* [2000]; *Rajopadhyaya et al.* [1998]; *Schafer et al.* [2002]). DSD retrieved by a AR was also used to compare with that measured by an aircraft [*Rogers et al.*, 1993]. In order to estimate the spectral parameters of the clear-air echo, the contamination of the hydrometeor echo must be eliminated as much as possible. *Williams* [2012] proposed a method for improving the estimation accuracy of W by using 50-MHz band and UHF ARs. However, UHF ARs are not always operated with 50-MHz band ARs. Therefore, in

the condition that only the 50-MHz band AR is used, computation methods must be developed and evaluated for estimating the spectral parameters of the clear-air echo fast and accurate.

In the following chapters, using numerical simulation, methods for estimating the spectral parameters from high-resolution observation in the clear air region are investigated. By setting different simulation parameters, the optimum parameters for estimating the spectral parameters with improved accuracy are determined. Further, the numeric simulation is used to develop and evaluate a method that estimates the spectral parameters under the condition that the use of incoherent integration is necessary. In the precipitation region, raindrops, ice particles, et cetera have different fall velocities and particle sizes vary with height. We investigate ways to distinguish turbulence echoes from precipitation echoes using the numerical simulation and measurement data.

Chapter 3

Methods for estimation of spectral parameters and error estimation in clear air region

3.1 Computation methods for the spectral parameters

In this section, the computation methods for calculating the spectral parameters in clear air region are described. By arranging the computation method described by Y88, we computed estimation errors of the spectral parameters. The computation method described by Y88 has the following four steps. In the first step, a Doppler spectrum is produced. The Doppler spectrum follows the Gaussian distribution and has perturbations following the χ^2 distribution with two degrees of freedom. Then, the Doppler spectrum is low-pass filtered (i.e., smoothed) with a von Hann window in order to reduce the perturbations. In the second step, a Doppler velocity point which has the peak intensity of the Doppler spectrum is found. The point is used as the first guess for the Doppler shift. In the third step, Doppler spectrum points used for calculating the spectral parameters are selected. The Doppler spectrum points have the Doppler spectrum peak in its center, and the number of Doppler

spectrum points is fixed. In the last step, the spectral parameters are calculated by using the initial values determined in the second step, the Doppler spectrum points selected in the third step, and the least squares method.

We made the following modifications to the method of Y88.

- In the method of Y88, the number of Doppler spectrum points used for calculating the spectral parameters was fixed. It is expected that estimation accuracy of the spectral parameters will improve by selecting the Doppler spectrum points under the condition where the intensity of clear-air echo (hereafter echo) is greater than the noise intensity. Therefore, we investigated a method that selects the Doppler spectrum points more adaptively.

- Because the smoothing method significantly affects the performance of the selection of the Doppler spectrum points, two methods for smoothing a Doppler spectrum were examined; they are the running average with equal weight (hereafter RA) and the multi-taper method (hereafter MTM). The RA was tested because its weighting of signal points is simple (i.e., equal for all the signal points). As an alternative computation, the MTM was tested as well. The MTM produces a set of filtered Doppler spectra by using orthogonal tapers. Then, the set of Doppler spectra are added into a single Doppler spectrum [*Thomson*, 1982]. Because the MTM can set its bandwidth easily, the MTM is useful for evaluating the performance of the RA. Though the MTM degrades the Doppler velocity resolution, it can reduce the spectrum perturbations without degrading the time resolution because the Doppler spectra produced by the orthogonal tapers have independent spectrum perturbations. *Anandan et al.* [2004] reported that the MTM can improve echo detection in low SNR conditions.

- Section 1.3.5 indicates that the moment method is simple that requires only the determination of the Doppler spectrum points which are used for calculating the spectral parameters. Because a huge amount of data needs to be processed in RIM measurements, we used the moment method to calculate the spectral parameters.

- For turbulence measurements using RIM, the time resolution must be as high as possible. Therefore, the use of incoherent integration, which can reduce estimation errors of the spectral parameters by degrading the time resolution, should be minimized. In this study, a practical index for assessing the errors of the spectral parameters is investigated. The index is useful for judging whether or not incoherent integration should be applied.

3.1.1 Computation method for the spectral parameters using the Running Average with equal weight (RA)

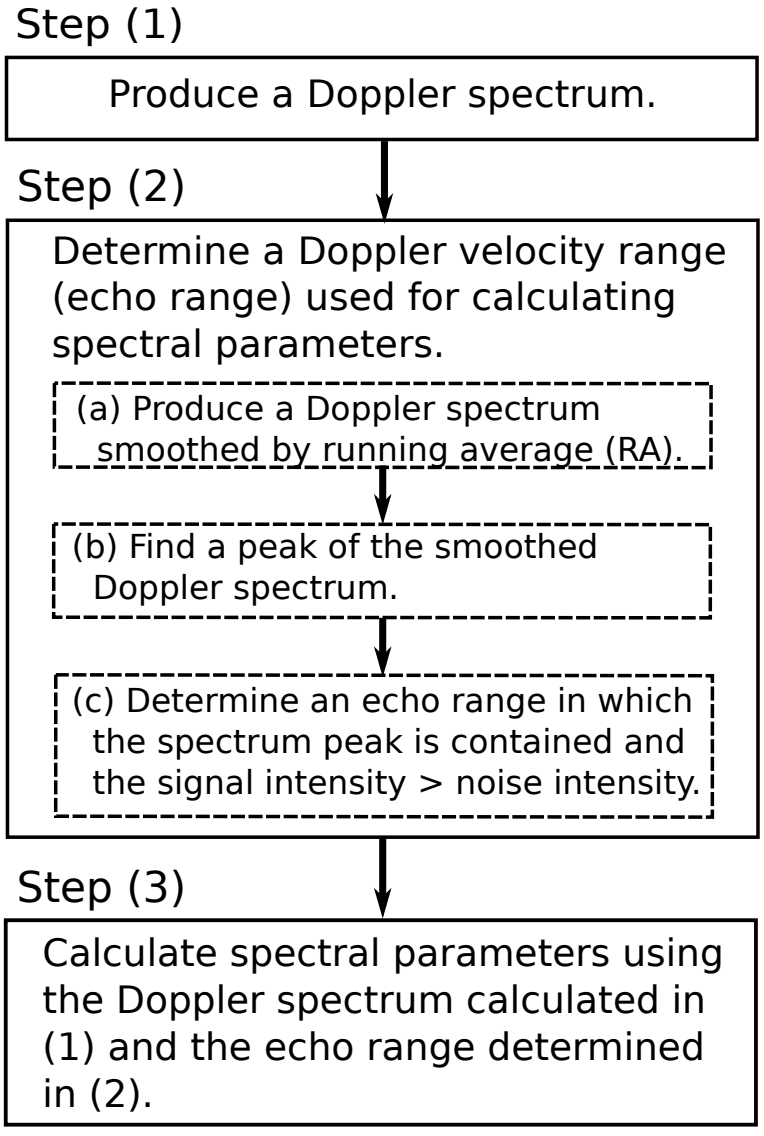

FIGURE 3.1: Flow chart of the computation method using the running average with equal weight (RA).

Figure 3.1 shows a flow chart of the computation method for estimating the spectral parameters using the RA. The signal processing has three steps. In Step (1), a Doppler spectrum is produced. We presumed that only an echo and white noise existed in the Doppler spectrum. Namely, other radio sources such as external interferences and clutters were not considered. Similar to Y88, we assumed that the Doppler spectrum of the echo follows the Gaussian distribution and has perturbations following the χ^2 distribution with two degrees of freedom. For simplicity, V_{d} was fixed to 0 and distortions of Doppler spectra caused by the limited frequency resolution of the Doppler spectrum (e.g., *Sato and Woodman* [1982]) were not taken into account. The noise intensity of the Doppler velocity bin (p_{n}) was set to 0 dB. In practical use, the noise level can be estimated from the received power at high-height ranges where echoes are not detected. In the simulation, because the Doppler velocity unit is normalized by the Doppler velocity resolution of a spectrum bin (ΔV_{bin}), bandwidth of the Doppler spectrum is equal to the number of Doppler spectrum points (NDATA). The value of noise power (P_{N}) is equal to the NDATA. The SNR is defined by P/P_{N}. Table 3.1 shows typical parameters for RIM measurements of the MU radar [*Hassenpflug et al.*, 2008] and the RIM LQ-7 [*Yamamoto et al.*, 2014]. In the table, F_{center} is the center radio frequency. IPP is the inter-pulse period. NBEAM is the number of beam directions. NFREQ is the number of radio frequencies. NCOH is the number of coherent integration times. NDATA is the number of Doppler spectrum points. For each record, the measurement time (T_{obs}) can be calculated as

$$T_{\mathrm{obs}} = \mathrm{IPP} \times \mathrm{NBEAM} \times \mathrm{NFREQ} \times \mathrm{NCOH} \times \mathrm{NDATA} \tag{3.1}$$

Beam directions are switched after Doppler spectrum collection (i.e., every NFREQ$\times$ NCOH $\times$ NDATA times transmission) for the RIM LQ-7. For the MU radar, beam directions are switched every transmission. 'V', 'N', and 'E' in the NBEAM row indicate the vertical, northward, and eastward beam direction. The Nyquist velocity (V_{NYQ}) can be calculated by

$$V_{\mathrm{NYQ}} = \pm \frac{1}{\mathrm{IPP} \times \mathrm{NFREQ} \times \mathrm{NCOH}} \times \frac{c}{4F_{\mathrm{center}}}. \tag{3.2}$$

For the MU radar and RIM LQ-7, V_{NYQ} are $\pm$16.8 m s^{-1} and $\pm$10.6 m s^{-1}, respectively. For the MU radar and RIM LQ-7, the Doppler velocity resolution of a spectrum bin ($\Delta V_{\mathrm{bin}} = 2 \times |V_{\mathrm{NYQ}}|/\mathrm{NDATA}$) are $\sim$0.07 m s^{-1} and $\sim$0.04 m s^{-1}, respectively.

In the simulation, we used the same value for the NDATA (512) as that listed in Table 3.1. In the simulation, the units of V_{d} and σ_{3dB} were normalized by ΔV_{bin}. The cases $\sigma_{\mathrm{3dB}} = 10$, 50, and 90, which are considered to be typical values for the narrow, large, and very large spectrum widths, were investigated in detail. σ_{3dB} of 10, 50, and 90 correspond to $\sim$0.66, 3.28, and 5.91 m s^{-1} for the MU radar case and $\sim$0.42, 2.08, and 3.74 m s^{-1} for the RIM LQ-7 case, respectively.

In Step (2), Doppler spectrum points used for calculating the spectral parameters are selected. Firstly, in order to minimize effects of perturbations of the Doppler spectrum, the Doppler spectrum smoothed by the RA (hereafter smoothed Doppler spectrum) was produced. Next, we found the peak location of the smoothed Doppler spectrum. Finally, using the smoothed Doppler spectrum, we determined the Doppler velocity range in which the peak of the Doppler spectrum is contained and the signal intensity is greater than the noise level (hereafter referred to as the echo range).

In Step (3), the spectral parameters are calculated using the moment method. The Doppler spectrum produced in Step (1), which was not smoothed by the RA, was used because the Doppler spectrum smoothed by the RA is broadened and hence it can overestimate σ_{3dB}. Only the Doppler spectrum points within the echo range were used for calculating the spectral parameters.

TABLE 3.1: Measurement parameters for (a) the middle and upper atmosphere radar (MU radar) and (b) a 1.3-GHz range-imaging wind profiler radar (RIM LQ-7).

(a) MU Radar

Item	Value
F_{center}	46.5 MHz
IPP	400 μ s
NBEAM	15 (V×5, N×5, E×5)
NFREQ	5
NCOH	16
NDATA	512
Transmitted pulse	1 μs×16 (16 bit optimum Spano code)
V_{NYQ}	$\pm$16.8 m s^{-1}
ΔV_{bin}	0.07 m s^{-1}
T_{obs}	49.2 s

(b) RIM LQ-7

Item	Value
IPP	65 μ s
Operating frequency	1357.00, 1357.25, 1357.50, 1357.75, 1358.00 MHz
Beam directions	(Azimuth, Zenith) = (0°, 0°), (0°, 14.3°), (0°, 0°), (90°, 14.3°)
NBEAM	4 (V, N, V, E)
NFREQ	5
NCOH	16
NDATA	512
Transmitted pulse width	1 μs × 8 (8 bit optimum Spano code)
V_{NYQ}	$\pm$10.6 m s^{-1}
ΔV_{bin}	0.04 m s^{-1}
T_{obs}	10.6 s

Figure 3.2 shows examples of the Doppler spectrum, the estimated echo range ($R_{\text{est\_RA}}$), and estimated spectral parameters. As a proxy of the echo range, the

Doppler velocity range, in which the model echo intensity is 0.05 times or more greater than p_{n} ($R_{\mathrm{echo\_RA}}$), is shown in each panel. Owing to the perturbations of the Doppler spectrum, some parts of the unsmoothed Doppler spectrum within $R_{\mathrm{echo\_RA}}$ have intensities smaller than p_{n} (see Figures 3.2(b-2) and (b-3)). This result indicates that a Doppler spectrum needs to be smoothed in order to determine the echo range with improved accuracy. It is clear that underestimation of the echo range, which is represented by the difference between $R_{\mathrm{echo\_RA}}$ and $R_{\mathrm{est\_RA}}$, was large for the cases $\sigma_{\mathrm{3dB}} = 50$ and 90 under the low SNR of -9 dB (Figures 3.2(b-2) and (b-3)); owing to the underestimation of $R_{\mathrm{est\_RA}}$, the estimated σ_{3dB} was as small as 41.1 (55.9) for the model echo with σ_{3dB} of 50 (90). These results indicate that the estimation accuracy of $R_{\mathrm{est\_RA}}$ is a major factor that determines errors in the spectral parameters. The relation between them is discussed in detail in Section 3.2.1.

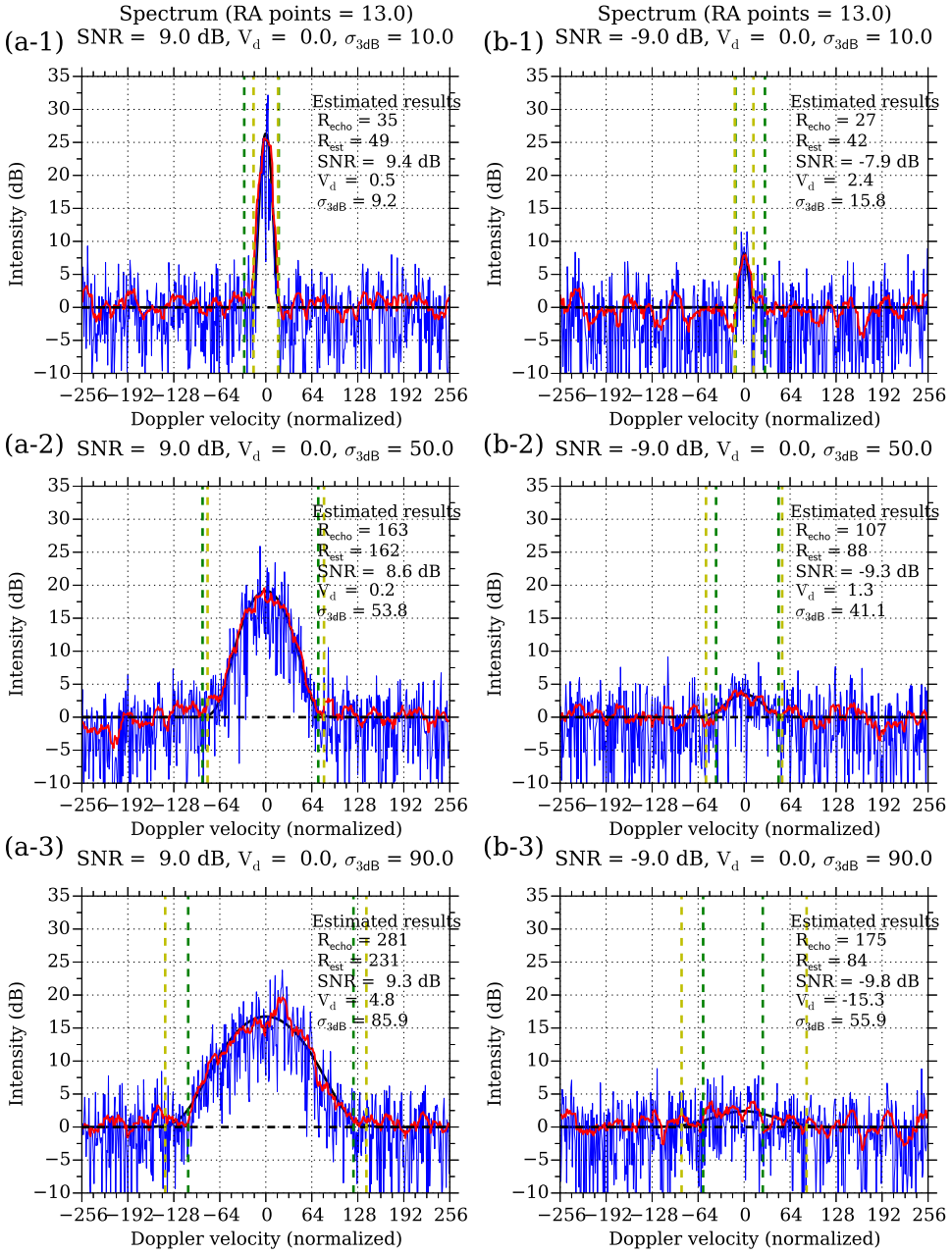

FIGURE 3.2: Examples of Doppler spectra smoothed by the 13-point RA. The panels (a-1) – (a-3) show cases for V_{d} of 0, SNR of 9 dB, and $\sigma_{3\mathrm{dB}}$ of 10, 50, and 90, respectively. The panels (b-1) – (b-3) show cases for SNR of −9 dB. In all the panels, the blue curve is the Doppler spectrum without the RA, the red curve is the Doppler spectrum smoothed by the RA, the black curve is the model echo, the black dashed line is the noise intensity (p_{n}), the green dashed lines are the boundaries of the estimated echo range ($R_{\mathrm{est\_RA}}$), and the yellow dashed lines are the boundaries of the Doppler velocity range in which the model echo is 0.05 times or more greater than p_{n} ($R_{\mathrm{echo\_RA}}$). $R_{\mathrm{echo\_RA}}$ is used as a proxy of the ideal echo range. The Doppler spectrum points within $R_{\mathrm{est\_RA}}$ were used for calculating the spectral parameters, and the estimation results are shown in each panel.

3.1.2 Computation method for the spectral parameters using the Multitaper method (MTM)

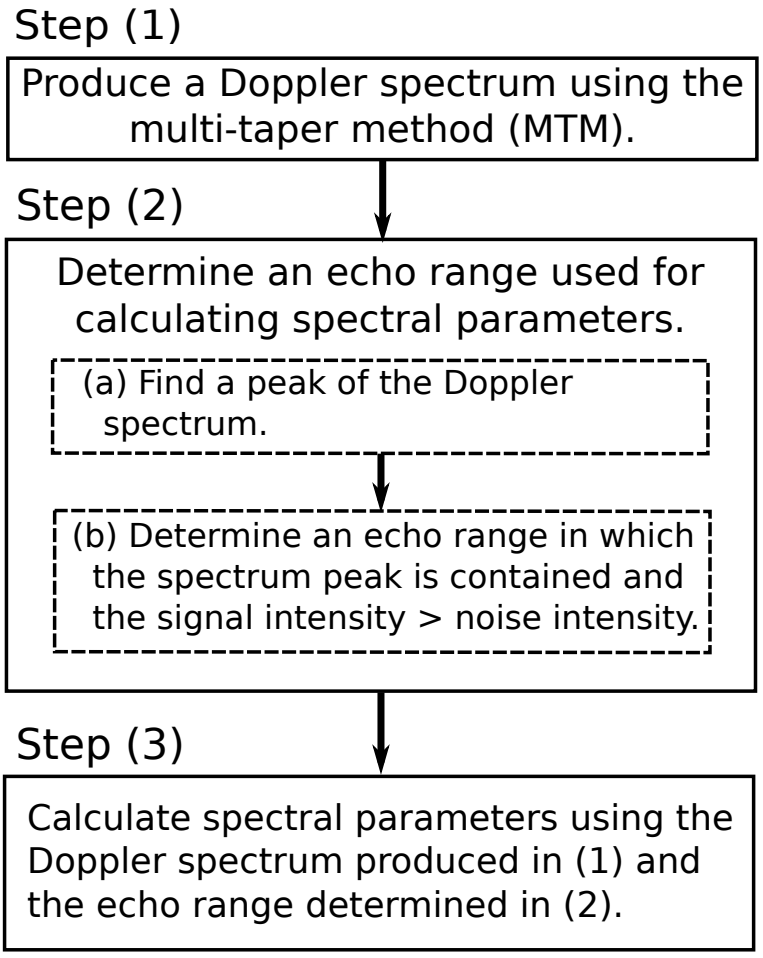

FIGURE 3.3: Flow chart of the computation method using the multi-taper method (MTM).

Figure 3.3 shows a flow chart of the computation method using the MTM. The signal processing has three steps. In Step (1), a Doppler spectrum is produced using the MTM. As a taper function of the MTM, the Slepian taper [*Slepian*, 1978] and the minimum bias taper [*Riedel and Sidorenko*, 1995] were examined. In this study, only results using the Slepian taper are shown because the two tapers had similar estimation performances. The normalized bandwidth (W) is defined by the taper bandwidth divided by the resolution of each Doppler velocity bin. W determines the degree of broadening of a Doppler spectrum and the amount by which spectrum perturbations are reduced. The number of Slepian tapers (K) is $2W - 1$.

The Slepian taper can be calculated as

$$D \times \alpha - \lambda \times \alpha = 0, \tag{3.3}$$

where the matrix D has components

$$D_{t,t'} = \frac{\sin 2\pi W(t-t')}{\pi(t-t')}, \quad t, t' = 0, 1, ..., \mathrm{NDATA} - 1 \tag{3.4}$$

and is symmetric. The solution of (3.3) has eigenvalues $1 > \lambda_0 > \lambda_1 > \cdots\cdots\cdots > \lambda_{\mathrm{NDATA}-1} > 0$ and associated eigenvectors $v_{\mathrm{k}}(t)$ called the Slepian sequences. Then the Slepian sequences which correspond to the largest K eigenvalues are selected as the Slepian tapers. Figure 3.4 shows an example of the calculated Slepian tapers with W of 6.

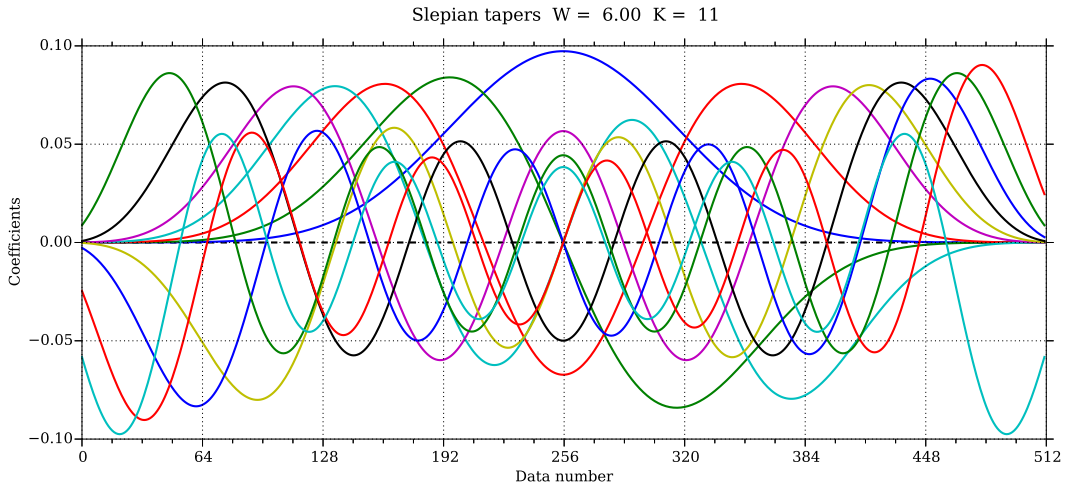

FIGURE 3.4: Example of Slepian tapers with W of 6.

In Step (2), we find the peak location of the Doppler spectrum and then determine the echo range. In Step (3), the spectral parameters are calculated using the Doppler spectrum points within the echo range. Note that the Doppler spectrum produced in Step (1) (i.e., the Doppler spectrum produced using the MTM) was used in both Step (2) and (3).

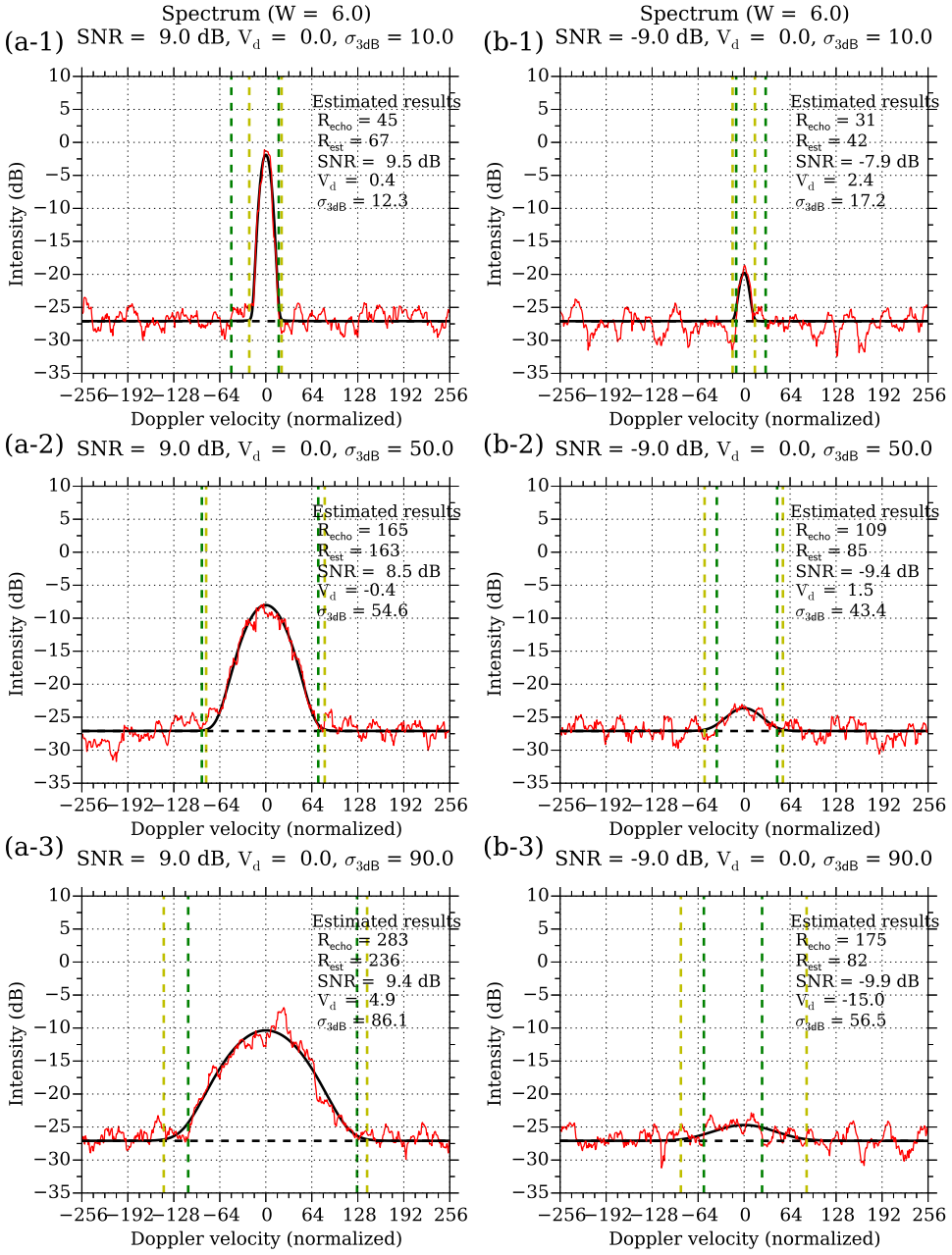

FIGURE 3.5: Same as Figure 3.2 except that the Doppler spectra are produced by the MTM. The Doppler spectra are shown by the red curves. In the computation, a W of 6 and the Slepian tapers were used.

Figure 3.5 shows examples of the Doppler spectrum calculated by using Slepian tapers and minimum bias tapers, respectively. The estimated echo range ($R_{\text{est\_MTM}}$) and estimated spectral parameters are shown. As the case of the computation method using the RA, the accuracy of echo range estimation is a major factor that determines the errors in the spectral parameters. Under a low SNR of -9

dB, as the case of the computation method using the RA, $\sigma_{3\mathrm{dB}}$ was significantly underestimated for the model echoes with $\sigma_{3\mathrm{dB}}$ of 50 and 90. The relation between them is discussed in detail in Section 3.2.2.

3.2 Results and discussion

3.2.1 Estimation error of the computation method using RA

Estimation errors of the spectral parameters for the computation method using the RA are discussed in this section. Firstly, estimation errors of the spectral parameters in high and low SNR cases are presented. Next, we investigate the optimum number of RA points for estimating the spectral parameters.

3.2.1.1 Errors in high SNRs

Figure 3.6 shows the relation between the SNR and the estimation errors for the cases where 7, 13, and 19 RA points were used. In order to evaluate the estimation errors of the spectral parameters in detail, we show both the bias and root-mean-square (hereafter RMS) errors. We varied the number of cases used for the evaluation and confirmed that using 1000 cases is sufficient for quantifying estimation errors even with low SNRs. Between the cases, perturbations of the Doppler spectrum are independent.

Figures 3.6(a-1), (b-1), and (c-1) show the estimation errors of P. For a SNR range of ≥ 0 dB, the bias was within $\pm 2.2\%$ for all the $\sigma_{3\mathrm{dB}}$ and RA-point cases. Therefore, the underestimation of P caused by the echo range selection is negligibly small. For a SNR range of ≥ 0 dB, the case $\sigma_{3\mathrm{dB}} = 10$ (90) had a RMS error of $\sim$26.0% ($\sim$8.6%). Effects of Doppler spectrum perturbations on the estimation errors of P become greater when the echo intensity decreases more sharply as the distance from the peak location increases. Therefore, the estimation errors of P for $\sigma_{3\mathrm{dB}}$ of 10 were greater than those for $\sigma_{3\mathrm{dB}}$ of 90.

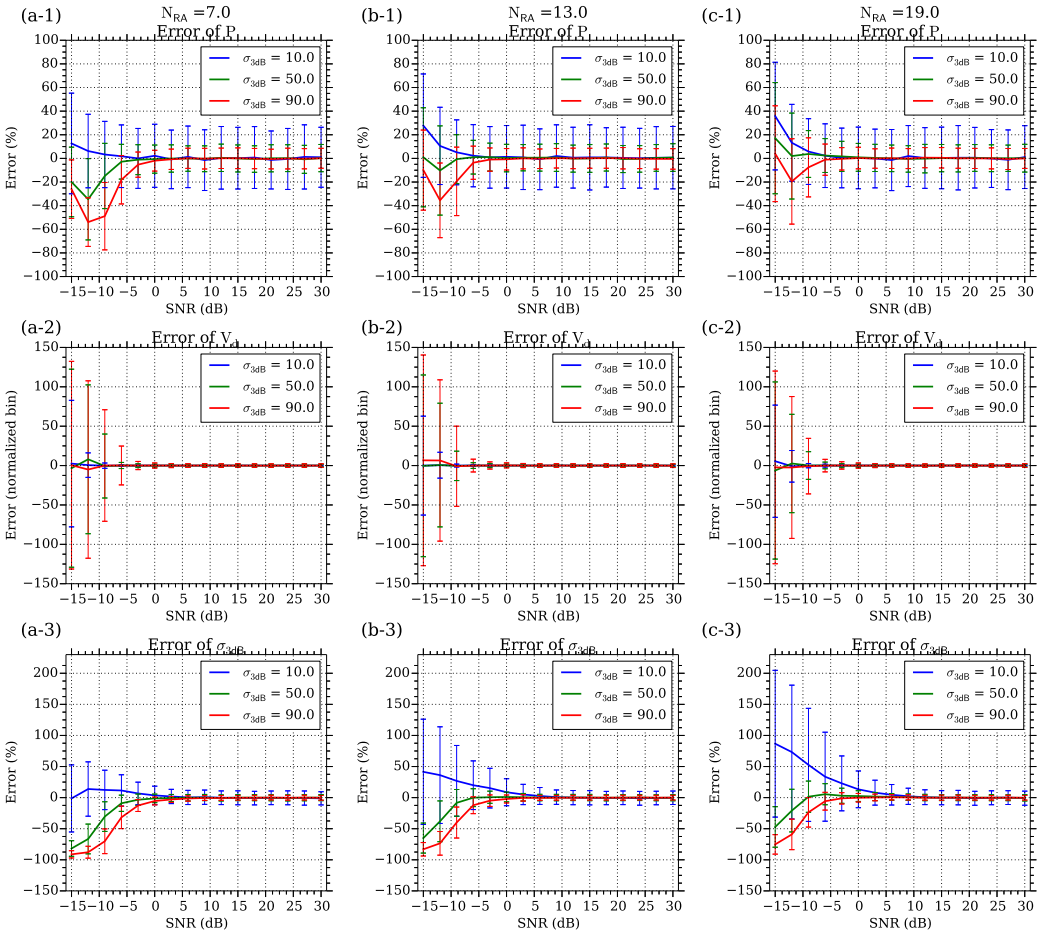

FIGURE 3.6: Errors of the spectral parameters calculated by the computation method using the RA. The panels (a-1), (a-2), and (a-3) show the errors of P, V_d, and σ_3dB, respectively, for RA points of 7. The blue, green, and red curves are errors for the model echoes with σ_3dB of 10, 50, and 90, respectively. The vertical lines are the root-mean-square (RMS) errors. The panels (b-1) – (b-3) and (c-1) – (c-3) show the results for RA points of 13 and 19, respectively.

Figures 3.6(a-2), (b-2), and (c-2) show the estimation errors of V_d. For a SNR range of $\geq$ 0 dB and σ_3dB = 10, the RMS errors of V_d were $\sim$0.8 for all the RA-point cases. For σ_3dB = 90, the values were $\sim$2.5 for all the RA-point cases. These results indicate that the RMS errors of V_d in high SNR cases were almost constant for all the RA-point cases.

Figures 3.6(a-3), (b-3), and (c-3) show the estimation errors of σ_3dB. For a SNR range of $\geq$ 6 dB and the model echo with σ_3dB of 10, the bias and RMS errors of σ_3dB were within $\pm$4.6% and $<$ 16.5% for all the RA-point cases. For a SNR range of $\geq$ 3 dB and the model echo with σ_3dB of 50 (90), they were within $\pm$1.7

(± 3.0)% and < 6.6 (5.3)% for all the RA-point cases. As the estimation error of P, the case which uses the model echo with $\sigma_{3\mathrm{dB}}$ of 10 had the greatest estimation error of $\sigma_{3\mathrm{dB}}$.

3.2.1.2 Errors in low SNRs

Doppler velocity For a SNR range of ≤ -3 dB, the errors of V_d increased with decreases of the SNR (see Figures 3.6(a-2), (b-2), and (c-2)). For the case $\sigma_{3\mathrm{dB}} = 10$, the bias and RMS values of the peak location were almost the same between SNRs of 9 dB and -9 dB (see Table 3.2). The two values indicate that the accuracy of the peak determination was almost unchanged. The estimation accuracy of the $R_{\mathrm{est\_RA}}$ was also almost unchanged between SNRs of 9 dB and -9 dB because the values of $R_{\mathrm{est\_RA}}/R_{\mathrm{echo\_RA}}$ did not show large differences (see Tables 3.3 and 3.4).

TABLE 3.2: Bias and the RMS values of the peak location calculated by using the RA.

$\sigma_{3\mathrm{dB}}$	7-point RA		13-point RA		19-point RA	
	SNR		SNR		SNR	
	9 dB	-9 dB	9 dB	-9 dB	9 dB	-9 dB
10	0.1 ± 1.9	0.1 ± 2.0	-0.1 ± 1.4	0.0 ± 1.5	0.0 ± 1.1	0.0 ± 2.0
50	0.1 ± 9.2	1.8 ± 40.6	0.1 ± 8.5	-1.0 ± 20.8	0.2 ± 7.9	0.4 ± 14.3
90	0.5 ± 15.3	-2.0 ± 83.7	0.3 ± 14.2	0.5 ± 54.2	-0.4 ± 13.4	-0.8 ± 42.6

TABLE 3.3: Mean and RMS value of $R_{\mathrm{est\_RA}}$ calculated by using the RA. The SNR is 9 dB. The data elements contain two lines. The first lines show the mean and RMS values of $R_{\mathrm{est\_RA}}$. The second lines show the percentage values of $R_{\mathrm{echo\_RA}}$.

$\sigma_{3\mathrm{dB}}$	$R_{\mathrm{echo\_RA}}$	RA points		
		7	13	19
10	35	40.2 ± 6.1 $115 \pm 17\%$	50.1 ± 11.5 $143 \pm 33\%$	58.2 ± 14.2 $166 \pm 41\%$
50	163	147.2 ± 9.2 $90 \pm 6\%$	158.3 ± 13.2 $97 \pm 8\%$	167.9 ± 16.7 $103 \pm 10\%$
90	281	240.6 ± 12.3 $86 \pm 4\%$	258.4 ± 16.2 $92 \pm 6\%$	270.6 ± 19.7 $96 \pm 7\%$

TABLE 3.4: Same as Table 3.3 except that the SNR is −9 dB.

σ_{3dB}	R_{echo_RA}	RA points		
		7	13	19
10	27	28.5 ± 6.5 106 ± 24%	37.0 ± 10.4 137 ± 39%	46.6 ± 15.1 173 ± 56%
50	107	61.9 ± 19.7 58 ± 18%	85.9 ± 17.5 80 ± 16%	99.0 ± 19.2 93 ± 18%
90	175	42.7 ± 26.6 24 ± 15%	90.3 ± 35.5 52 ± 20%	122.9 ± 32.9 70 ± 19%

For the case $\sigma_{3dB} = 10$ with a 13-point RA, the RMS error of V_d was ∼0.8 for a SNR of 9 dB and ∼1.8 for a SNR of −9 dB (Figure 3.6(b-2)). These results show that the increased effects of noise perturbations mainly caused the increase in the RMS error of V_d for the case $\sigma_{3dB} = 10$ and SNR = −9 dB.

For the case $\sigma_{3dB} = 90$ with a 13-point RA, the RMS error of V_d, which was ∼2.4 for a SNR of 9 dB, increased to ∼50.9 for a SNR of −9 dB (Figure 3.6(b-2)). The difference between the RMS value of the peak location for the SNR of 9 dB (14.2) and that for the SNR of −9 dB (54.2) was as large as 40.0 (Table 3.2). The difference in the peak location indicates that the peak location was not determined well for low SNR and large σ_{3dB} conditions owing to the large effects from noise perturbations, and the large RMS value of the peak location for the SNR of −9 dB contributed to the large RMS error of V_d.

The difference in errors of the peak location and R_{est_RA} between the cases σ_{3dB} = 10 and 90 can be explained by the fact that the peak intensity of a model echo has a factor of σ^{-1} for an identical SNR, and hence the peak intensity for the case $\sigma_{3dB} = 10$ is 9.5 dB greater than that for the case $\sigma_{3dB} = 90$. The relation between the peak intensity of a Doppler spectrum and the estimation errors of the spectral parameters is discussed in detail in Section 3.2.3.

The RMS error of V_d decreased with an increasing number of RA points. For the case of a SNR of −6 dB and 7-point RA, the RMS error of V_d for σ_{3dB} of 90 was 24.7 (Figure 3.6(a-2)). For the same SNR but with a 19-point RA, the value decreased to 8.0 (Figure 3.6(c-2)). The bias and RMS value of the peak location, which were 0.6 ± 26.4 for the case of the 7-point RA, improved to 0.3 ± 16.4 for the 19-point RA.

Furthermore, the value of $R_{\text{est\_RA}}/R_{\text{echo\_RA}}$, which was 53 ± 15% for the 7-point RA, improved to 83 ± 12% with the 19-point RA (Table 3.5). These results indicate that the accuracy of the peak location and $R_{\text{est\_RA}}$ can be improved by increasing the number of RA points, and the accuracy improvement causes error reductions in V_{d} estimation.

TABLE 3.5: Same as Table 3.3 except that the SNR is −6 dB.

$\sigma_{3\text{dB}}$	$R_{\text{echo\_RA}}$	RA points		
		7	13	19
10	29	31.3 ± 6.7 108 ± 23%	39.3 ± 10.0 136 ± 34%	48.5 ± 14.5 167 ± 50%
50	119	87.5 ± 12.7 74 ± 11%	103.8 ± 14.6 87 ± 12%	114.5 ± 18.5 96 ± 16%
90	197	104.8 ± 28.7 53 ± 15%	145.5 ± 21.9 74 ± 11%	163.5 ± 23.0 83 ± 12%

Echo power For the cases $\sigma_{3\text{dB}} = 50$ and 90, P was underestimated in low SNR situations (see Figures 3.6(a-1), (b-1), and (c-1)). The underestimation was improved by increasing the number of RA points. For the case $\sigma_{3\text{dB}} = 50$, SNR of −9 dB, and 7-point RA, the bias and RMS errors were approximately −14.9% and 27.6%, respectively (Figure 3.6(a-1)). For the case of a 19-point RA, the values were reduced to ∼3.7% and ∼19.8% (Figure 3.6(c-1)). For the case $\sigma_{3\text{dB}} = 50$ with a SNR of −9 dB, the value of $R_{\text{est\_RA}}/R_{\text{echo\_RA}}$, which was 58 ± 18% for the 7-point RA, increased up to 93 ± 18% for the 19-point RA (see Table 3.4). These results indicate that increasing the number of RA points can improve the underestimation of P by reducing the error of $R_{\text{est\_RA}}$.

For the case $\sigma_{3\text{dB}} = 90$ with a SNR of −9 dB, the underestimation of P was as large as −48.9% for the 7-point RA, and it was still as large as −7.6% for the 19-point RA. For RA points of 7 (19), $R_{\text{est\_RA}}$ covered only 24 ± 15 (70 ± 19)% of the $R_{\text{echo\_RA}}$ (see Table 3.4). These results indicate that the degree of improvement in P estimation depends not only on the SNR but also on $\sigma_{3\text{dB}}$. In Section 3.2.3, factors that determine the errors of the spectral parameters are investigated in more detail.

Spectrum width Firstly, the case $\sigma_{3\mathrm{dB}} = 10$ is discussed. As shown in Figures 3.6(a-3), (b-3), and (c-3), for a SNR range of $\leq$ 3 dB, $\sigma_{3\mathrm{dB}}$ was overestimated for all of the RA-point cases. The overestimation increased with decreases in the SNR and with increases in the number of RA points for an identical SNR. For a SNR of -6 dB, the overestimation was 11.5 $\pm$ 25.3%, 19.9 $\pm$ 39.1%, and 33.6 $\pm$ 71.6% for the cases of 7-point, 13-point, and 19-point RAs, respectively. The mean values of $R_{\mathrm{est\_RA}}$ were greater than $R_{\mathrm{echo\_RA}}$ and increased with the increase in the number of RA points (see Table 3.5). These results indicate that smoothing causes overestimation for a small $\sigma_{3\mathrm{dB}}$. Because Doppler spectra smoothed by the RA are broadened, $R_{\mathrm{est\_RA}}$ is overestimated. The overestimation of $R_{\mathrm{est\_RA}}$ causes an increase in the noise perturbations during the calculation of $\sigma_{3\mathrm{dB}}$, and hence $\sigma_{3\mathrm{dB}}$ is overestimated. However, it should be noted that overestimates of $\sigma_{3\mathrm{dB}}$ in terms of absolute values are only $\sim$1.2, 2.0, and 3.4 for the cases of 7-point, 13-point, and 19-point RAs, respectively, for a SNR of -6 dB (Figures 3.6(a-3), (b-3), and (c-3)). Therefore, the overestimation of $\sigma_{3\mathrm{dB}}$ is sufficiently small compared with the RMS errors.

For the case $\sigma_{3\mathrm{dB}} = 50$ with SNRs of ≤ -6 dB, underestimation of $\sigma_{3\mathrm{dB}}$ was significant. For the case where the SNR $= -6$ dB, the underestimation was improved substantially by increasing the number of RA points; the biases were -9.1%, -0.1%, and 5.5% for the cases of 7-point, 13-point, and 19-point RAs, respectively (Figures 3.6(a-3), (b-3), and (c-3)). However, $\sigma_{3\mathrm{dB}}$ was overestimated in the case of the 19-point RA because the value of $R_{\mathrm{est\_RA}}/R_{\mathrm{echo\_RA}}$ was as large as 96 $\pm$ 16% (Table 3.5).

For the case $\sigma_{3\mathrm{dB}} = 90$ with SNRs of ≤ 0 dB, $\sigma_{3\mathrm{dB}}$ was also underestimated. For a SNR of -6 dB, the biases were -31.7%, -12.3%, and -5.8% for the cases of 7-point, 13-point, and 19-point RAs, respectively (Figures 3.6(a-3), (b-3), and (c-3)). These results indicate that increasing the number of RA points can reduce the estimation error of $\sigma_{3\mathrm{dB}}$ even for very large $\sigma_{3\mathrm{dB}}$ of 90 and a low SNR of -6 dB. However, it should be noted that increasing the number of RA points causes overestimation of $\sigma_{3\mathrm{dB}}$ in the model echoes with $\sigma_{3\mathrm{dB}}$ of 10 and 50.

3.2.1.3 Detectability

For spectra with different σ_{3dB}, the decrease of peak intensity caused by RA is different. Therefore, we investigate the relation between the detectability calculated using the smoothed spectrum (D_{RA}) and the RA points (N_{RA}). Figure 3.7 shows the relation between N_{RA}/σ_{3dB} and D_{RA}/D. D is the detectability calculated using the spectrum without smoothing. It is noted that the modeled echo (without perturbation) was used in the calculation.

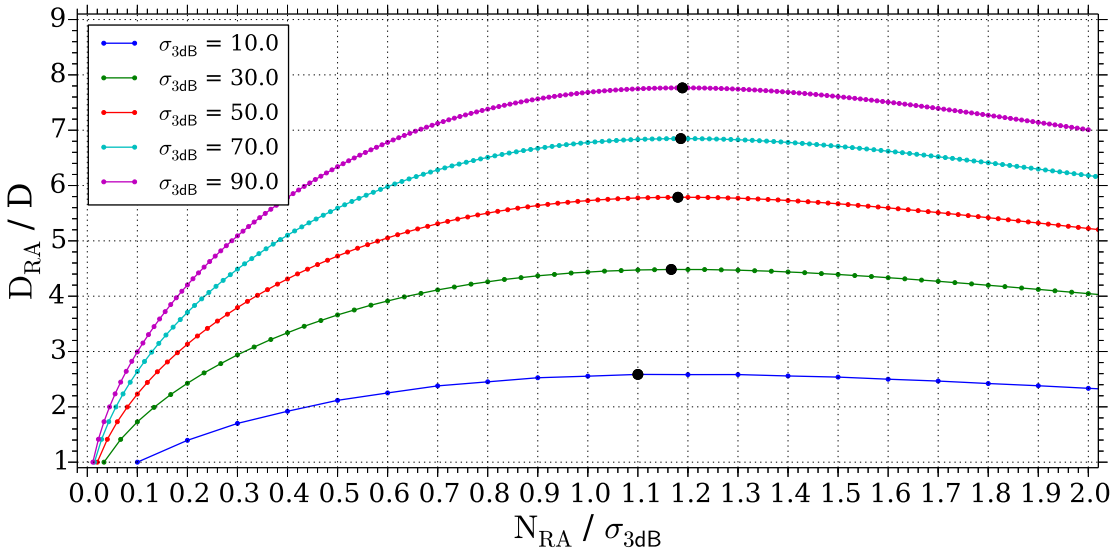

FIGURE 3.7: Relation between N_{RA}/σ_{3dB} and D_{RA}/D. N_{RA} is the RA points. D_{RA} is the detectability calculated using the modeled echo smoothed by RA. D is the detectability calculated using the modeled echo without smoothing. The black points indicate the maximum values of D_{RA}/D.

The black points indicate the maximum values of D_{RA}/D. The maximum values existed in a N_{RA}/σ_{3dB} range between 1.1 and 1.2 for different σ_{3dB}. The results indicated that the optimum N_{RA} varies with σ_{3dB}. Therefore, it is difficult for determining the optimum N_{RA} for different σ_{3dB}. For $\sigma_{3dB} > 10$, the corresponded N_{RA} is very large (i.e., $\sim$24 for σ_{3dB} of 20). Large values of N_{RA} may introduce more interference signals. The broaden effect on spectrum caused by smoothing will also become more serious for large values of N_{RA}. Therefore, large values of N_{RA} are not suitable for practical use.

In our method, the accurate estimation of peak location and that of R_{est_RA} determine the estimation accuracy of spectral parameters. Hereafter, we investigate

the relation between D and the estimation accuracy of peak location and that of $R_{\text{est\_RA}}$. Table 3.6 shows D and the detectability calculated using the modeled echo smoothed by 13-point RA (D_{RA}) for SNR of -9 dB, -6 dB and 9 dB, respectively. It is noted that because the peak intensity decreases after smoothing, D_{RA}/D is $< \sqrt{N_{\text{RA}}}$. Especially for $\sigma_{3\text{dB}}$ of 10, D_{RA} was only $\sim$2.6 times greater than D.

TABLE 3.6: Detectability (D) for different RA points and SNR cases.

$\sigma_{3\text{dB}}$	SNR					
	9 dB		-6 dB		-9 dB	
	D	D_{RA}	D	D_{RA}	D	D_{RA}
10	382.1	987.0	12.1	31.2	6.1	15.6
50	76.4	271.3	2.4	8.6	1.2	4.3
90	42.5	152.3	1.3	4.8	0.7	2.4

For the case of $\sigma_{3\text{dB}} = 10$, D_{RA} was ≥ 15.6. The peak location can be determined accurately (see Table 3.2). However, because of the broaden effect of RA, P and $\sigma_{3\text{dB}}$ were overestimated for SNR of -6 dB and -9 dB (see Figure 3.6). For the cases of $\sigma_{3\text{dB}} = 90$ and SNR $= -9$ dB, D_{RA} was 2.4 and the RMS value of peak location against $\sigma_{3\text{dB}}$ was as large as 0.60. $R_{\text{est\_RA}}$ was only 52% of $R_{\text{echo\_RA}}$. Therefore, both peak location and $R_{\text{est\_RA}}$ cannot be determined accurately for small D_{RA} (or D) condition. For the cases of $\sigma_{3\text{dB}} = 50$ and SNR of -9 dB and $\sigma_{3\text{dB}} = 90$ and SNR of -6 dB, D_{RA} increased to ≥ 4.3. These are boundary cases between success and unsuccess of the parameters estimation. Behavior of our initial value finding is like this; the RMS values of peak location against $\sigma_{3\text{dB}}$ decreased to 0.42 and 0.20, respectively. Under these two conditions, $R_{\text{est\_RA}}$ were only 80% and 74% of $R_{\text{echo\_RA}}$, respectively (see Tables 3.4 and 3.5). From this behavior we can summarize that the initial value finding was successful at its peak. The detectability enhanced by the averaging, D_{RA}, was $\geq$4.3 that exceeded 3.0. Next in the initial value finding, we search for the frequency range where effective signal components exist. However, the search soon stops as the signal intensity decreases and becomes indistinguishable from the noise components. As a results, the spectrum range used for the spectral parameters estimation was much narrower than the model expectation. The errors of the spectral parameters estimation under this condition

are shown below, but large. The errors of P, V_{d}, and $\sigma_{3\mathrm{dB}}$ were $-0.66 \pm 20.7\%$, -0.38 ± 18.6, $-8.4 \pm 18.6\%$ for the case of $\sigma_{3\mathrm{dB}} = 50$ and SNR of -9 dB, and $-3.7 \pm 14.0\%$, 0.0 ± 8.1, $-12.3 \pm 13.5\%$ for the case of $\sigma_{3\mathrm{dB}} = 90$ and SNR of -6 dB. The results indicate that the lowest D_{RA} which can be used as an indicator of accurate estimation of spectral parameters must be determined by considering both the peak location and $R_{\mathrm{est\_RA}}$.

3.2.1.4 Optimum number of RA points

The optimum number of RA points for the measurement parameters listed in Table 3.1 is discussed in this section. In high SNRs, the number of RA points does not significantly affect the estimation errors of the spectral parameters (Figures 3.6(a-1) – (c-3)). Therefore, only the errors of the spectral parameters in low SNRs need to be considered for determining the optimum number of RA points.

For the case which has a model echo with $\sigma_{3\mathrm{dB}}$ of 10 and SNR of -6 (-9) dB, the difference of the overestimation for the mean value of $\sigma_{3\mathrm{dB}}$ between the cases with 7-point and 13-point RAs was 0.8 (1.5) in terms of the absolute value with the unit of ΔV_{bin} (Figures 3.6(a-3) and (b-3)). However, the difference between the cases with 13-point and 19-point RAs was 1.4 for a SNR of -6 dB and 2.6 for a SNR of -9 dB (Figures 3.6(b-3) and (c-3)). These results indicate that increasing the number of RA points has some effect on the increases in the overestimation for small $\sigma_{3\mathrm{dB}}$.

For the cases $\sigma_{3\mathrm{dB}} = 50$ and 90, the improvements from the use of a 19-point RA were small. For the case $\sigma_{3\mathrm{dB}} = 50$ with a SNR of -6 dB (-9 dB), the difference of the underestimation for the mean value of $\sigma_{3\mathrm{dB}}$ between the 7-point and 13-point RAs was 4.5 (11.1) in terms of the absolute value with the unit of ΔV_{bin}. However, the difference decreased to only 2.9 (5.0) between the 13-point and 19-point RAs. For the case $\sigma_{3\mathrm{dB}} = 90$ with a SNR of -6 dB, the difference between the 7-point and 13-point RAs was 17.5 in terms of the absolute value with the unit of ΔV_{bin}. However, the difference decreased to only 5.9 between the 13-point and 19-point RAs. Furthermore, the use of a 19-point RA can lead to the overestimation of $\sigma_{3\mathrm{dB}}$ even for the model echo with $\sigma_{3\mathrm{dB}}$ of 50 and the SNR of -6 dB. These results indicate that the improvement by increasing the RA points from 7 to 13 is

greater than that gained by increasing the RA points from 13 to 19. Furthermore, in practical use, reducing the number of RA points has the advantage of reducing the effects of signals other than echoes (i.e., interference signals). From discussions shown above, we conclude that 13 is the optimum RA points.

In our study, all the values used in the simulation are normalized by ΔV_{bin}. ΔV_{bin} are 0.07 m s^{-1} for the MU radar and 0.04 m s^{-1} for the LQ-7. Therefore, N_{RA} of 13 corresponds to the Doppler velocity range of 0.91 m s^{-1} for the MU radar and 0.52 m s^{-1} for the LQ-7 (see Table 3.1). For observations with different measurement parameters, ΔV_{bin} also changes. Therefore, for the MU radar and LQ-7, the normalized optimum N_{RA} can be selected by $0.91/\Delta V_{\mathrm{bin}}$ and $0.52/\Delta V_{\mathrm{bin}}$, respectively.

Figure 3.7 indicates that D_{RA} has the maximum value when the value of $N_{\mathrm{RA}}/\sigma_{\mathrm{3dB}}$ is in the range between 1.1 and 1.2. D_{RA}/D at N_{RA} of 13 is close to the maximum for σ_{3dB} of 10. Further, D_{RA}/D does not vary large in the $N_{\mathrm{RA}}/\sigma_{\mathrm{3dB}}$ range of 1.0 and 1.3. Therefore, N_{RA} of 13 also can be considered as an optimum value for D_{RA}. The case that σ_{3dB} of 10 is selected as a possible narrow spectrum width case in AR observations. This may suggest that the better selection of RA velocity range is closer to the typical narrow spectrum width.

The results and interpretations shown in Section 3.2.1 demonstrate that the computation method described in Section 3.1.1 provides a simple way to estimate the errors of the spectral parameters and to determine the number of RA points that should be used for calculating the spectral parameters. Therefore, the computation method is useful not only for processing a huge amount of Doppler spectra data but also for providing a convenient way to estimate errors of the spectral parameters.

3.2.2 Estimation error of the computation method using MTM

The estimation errors of the spectral parameters for the computation method using the MTM and those for the computation method using the RA are now compared for the high and low SNR conditions. In order to match the bandwidth of the 13-point RA, W was set to be 6.

For the high SNR of 9 dB and low SNR of −9 dB, the bias and RMS values of the peak location for the computation method using the MTM did not show significant differences from those for the computation method using a 13-point RA (see Tables 3.2 and 3.7). Mean and RMS values of $R_{\text{est\_MTM}}$ also did not show significant differences from those of $R_{\text{est\_RA}}$ except for the case $\sigma_{3\text{dB}} = 10$ (see Tables 3.3, 3.4, and 3.8).

For the high SNR of 9 dB and the computation method using a 13-point RA, the RMS errors of V_{d} were 0.8, 1.7, and 2.4 for the cases $\sigma_{3\text{dB}} = 10$, 50, and 90, respectively (see Figure 3.6(b-2)). For the same SNR and the computation method using the MTM, they were 0.8, 1.8, and 2.4 (see Figures 3.8(b)). For the computation method using a 13-point RA, the RMS errors of P were 26.4%, 11.7%, and 8.3% for the cases $\sigma_{3\text{dB}} = 10$, 50, and 90, respectively (Figure 3.6(b-1)). For the computation method using the MTM, they were 25.5%, 11.4%, and 9.3% (Figures 3.8(a)). These results indicate that there were no significant difference between the errors of P and V_{d} for the computation method using the RA and those from the computation method using the MTM.

For the computation method using a 13-point RA, the RMS errors of $\sigma_{3\text{dB}}$ were 11.6%, 5.2%, and 3.8% for the cases $\sigma_{3\text{dB}} = 10$, 50, and 90, respectively (Figure 3.6(b-3)). For the computation method using the MTM, they were mostly the same as those from the computation method using the RA (8.9%, 5.1%, and 4.0%) (Figures 3.8(c)). However, for the case which has a model echo with $\sigma_{3\text{dB}}$ of 10 and SNR range of $\geq$ 6 dB, the bias of $\sigma_{3\text{dB}}$ was overestimated as ∼27% for the computation method using the MTM.

TABLE 3.7: Same as Table 3.2 except that the values were calculated by using the MTM. In the computation, a W of 6 and the Slepian tapers were used.

$\sigma_{3\text{dB}}$	SNR	
	9.0 dB	−9.0 dB
10	0.0 ± 1.5	−0.1 ± 3.0
50	−0.2 ± 8.9	−0.2 ± 26.2
90	−0.1 ± 14.5	3.4 ± 61.3

TABLE 3.8: Same as Table 3.3 except that the values were calculated by using the MTM.

$\sigma_{3\text{dB}}$	SNR = 9.0 dB		SNR = −9.0 dB	
	$R_{\text{echo\_MTM}}$	$R_{\text{est\_MTM}}$	$R_{\text{echo\_MTM}}$	$R_{\text{est\_MTM}}$
10	45	49.5 ± 10.4 110 ± 23%	31	35.0 ± 9.7 113 ± 31%
50	165	156.2 ± 11.7 95 ± 7%	109	80.3 ± 18.6 74 ± 17%
90	283	253.7 ± 14.3 90 ± 5%	175	77.6 ± 34.5 44 ± 20%

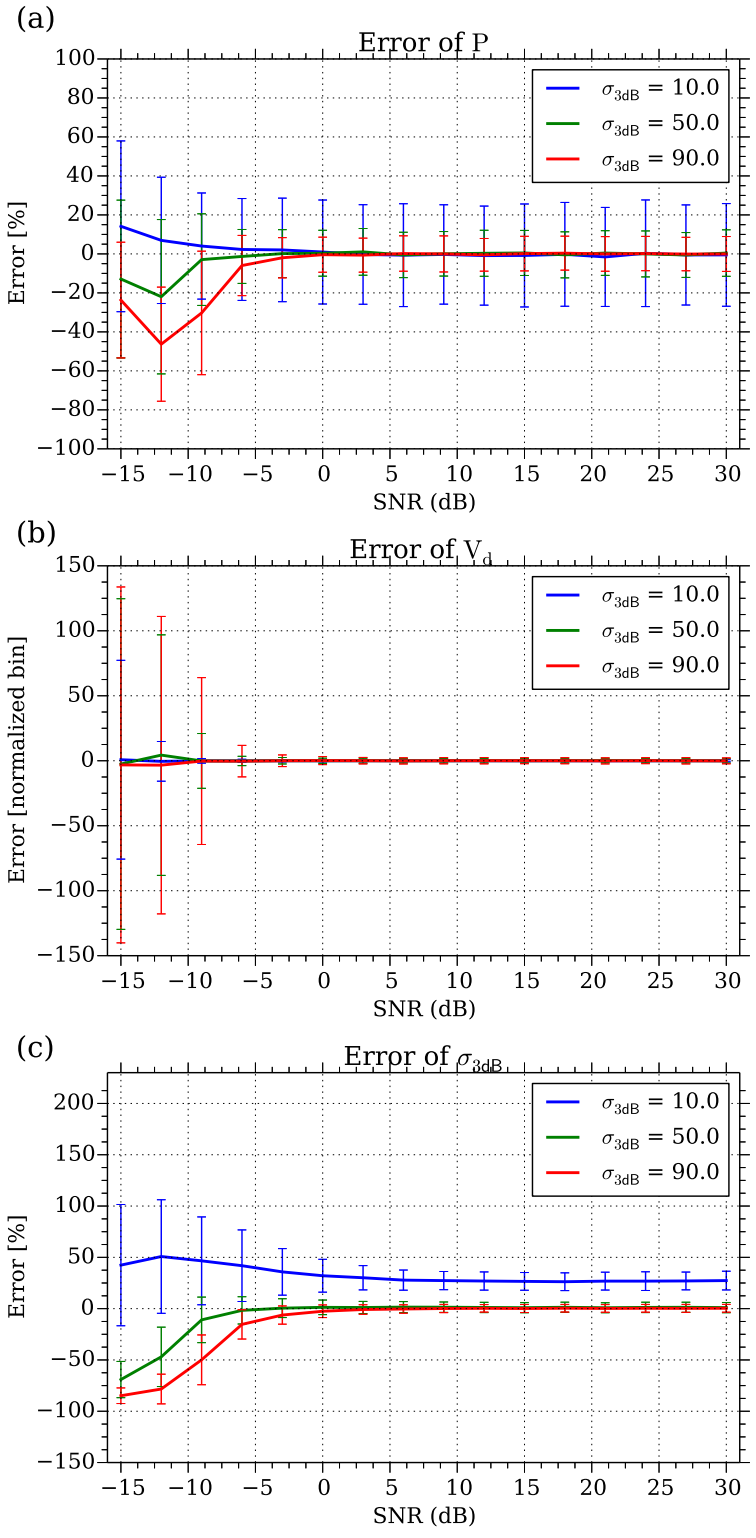

FIGURE 3.8: Same as Figure 3.6 except that the results obtained by the computation method using the MTM are shown. In the computation, a W of 6 and the Slepian tapers were used.

In the computation method using the MTM, Doppler spectra broadened by the

MTM were used for calculating the spectral parameters. In the computation method using the RA, Doppler spectra without filtering in the frequency domain were used. Therefore, the Doppler spectra broadened by the method involving the MTM can explain the overestimation of $\sigma_{3\mathrm{dB}}$ for the case which has a model echo with $\sigma_{3\mathrm{dB}}$ of 10. However, overestimation of $\sigma_{3\mathrm{dB}}$ was not seen for the cases which have model echoes with $\sigma_{3\mathrm{dB}}$ of 50 and 90.

For a low SNR of -6 dB and the computation method using a 13-point RA, the RMS errors of V_{d} were 1.3, 3.6, and 8.1 for the cases $\sigma_{3\mathrm{dB}} = 10$, 50, and 90, respectively (Figure 3.6(b-2)). For the same SNR and the computation method using the MTM, the values were comparable (1.3, 3.6, and 12.1, respectively; see Figures 3.8(b)). For the computation method using a 13-point RA, the errors of P were $2.3 \pm 26.3\%$ and $-3.7 \pm 14.0\%$ for the cases $\sigma_{3\mathrm{dB}} = 10$ and 90, respectively (Figure 3.6(b-1)). For the computation method using the MTM, the values were comparable ($2.3 \pm 26.1\%$ and $-6.0 \pm 15.5\%$, respectively; see Figures 3.8(a)). For the computation method using a 13-point RA, the errors of $\sigma_{3\mathrm{dB}}$ were $19.9 \pm 39.1\%$ and $-12.3 \pm 13.5\%$ for the cases $\sigma_{3\mathrm{dB}} = 10$ and 90, respectively (Figure 3.6(b-3)). For the computation method using the MTM, the values were $41.9 \pm 34.9\%$ and $-15.3 \pm 14.3\%$, respectively (Figures 3.8(c)). For the case which has a model echo with $\sigma_{3\mathrm{dB}}$ of 10, overestimation of $\sigma_{3\mathrm{dB}}$ was greater in the computation method using the MTM.

For the computation method using the MTM, the broadening effect was significant both in low and high SNRs for the case $\sigma_{3\mathrm{dB}} = 10$. For the cases $\sigma_{3\mathrm{dB}} = 50$ and 90, the performance of the computation method using the RA and that of the computation method using the MTM were comparable both in low and high SNRs. Because the computation method using the RA has better performance than that using the MTM, the RA is used to smooth the Doppler spectrum. We define the computation method using the RA as bottom method.

3.2.3 Relation between detectability and estimation errors of the spectral parameters

As discussed in 3.2.1.3, the detectability D has close relation with the determination accuracy of peak location. Hereafter, we examine whether or not D can be used as an indicator for assessing errors of the spectral parameters. Figure 3.9 shows the distribution of the estimation errors of the spectral parameters related to SNR and $\sigma_{3\mathrm{dB}}$. The values of D are shown by white curves. D is calculated using the peak intensity of modeled echo (p_{k}). For a D range of $\geq \sim 6$, the errors of the spectral parameters did not vary significantly by SNR and they tended to depend on the $\sigma_{3\mathrm{dB}}$ of model echo. For example, for SNR of 21 dB, the RMS errors of V_{d} were 0.8, 1.7, and 2.4 for the cases $\sigma_{3\mathrm{dB}} = 10$, 50, and 90, respectively (see also Figure 3.6(b-2)). The RMS errors of $\sigma_{3\mathrm{dB}}$, which were 11.0%, 4.9%, and 3.8% for the cases $\sigma_{3\mathrm{dB}} = 10$, 50, and 90, were 1.1, 2.5, and 3.4 in terms of absolute values. It should be noted that while the RMS error of $\sigma_{3\mathrm{dB}}$ for an identical SNR decreased with the increase of $\sigma_{3\mathrm{dB}}$ in terms of percentage, it increased in terms of the absolute value.

On the contrary, for a D range of $< \sim 6$, the errors of the spectral parameters became significantly larger as D decreased (see Figure 3.9). These results indicate that the errors of the spectral parameters are well correlated to SNR and D.

Because p_{k} cannot be obtained from the received Doppler spectrum, we examined whether or not the peak intensity of a smoothed Doppler spectrum at V_{d} (hereafter p_{est}) can be used as a substitute of p_{k}. Figure 3.10 shows the relation between SNR and p_{est} and that between SNR and p_{k}. It is noted that p_{n} is subtracted from p_{est} and p_{k}. Because the RA causes a decrease in the spectrum peak, p_{est} was $\sim$29% smaller than p_{k} for the case $\sigma_{3\mathrm{dB}} = 10$ (Figure 3.10(a)). However, because p_{est} is smaller than p_{k}, the difference did not cause underestimation of the errors of the spectral parameters. For the cases $\sigma_{3\mathrm{dB}} = 50$ and 90, the difference between them was $< 4\%$ for a SNR range of ≥ -8 dB (Figures 3.10(b) and (c)).

Determination accuracy of the peak location depends on p_{est}, and the noise perturbations do not significantly affect the estimation of the peak location when p_{k} is sufficiently greater than the noise perturbations. The RMS error of V_{d} is a good indicator of the error in the peak location (see Section 3.2.1.2). If the RMS error

of V_d is sufficiently small, we can conclude that p_{est} is not significantly affected by noise perturbations. Therefore, by setting the condition that the RMS error of V_d is < 5, we estimated the threshold value of D above which p_{est} can be used as a substitute for p_k. When D is ≥ 2.5, the RMS errors of V_d are mostly smaller than 5 except for small σ_{3dB} and low SNR cases (i.e., SNR $\leq \sim -9$ dB and $\sigma_{3dB} \leq \sim 20$; see Figure 3.9(b-2)). Therefore, D of 2.5 is the threshold that p_{est} can be used as a substitute for p_k. Furthermore, when D is $\geq \sim 2.5$, the ratio of the RMS values to the mean values in p_{est} was $\sim 30\%$ (see Figure 3.10).

For a SNR range between -6 dB and -3 dB, RMS errors of V_d for the case of a 7-point RA were greater than those for the case of a 13-point RA because reducing the RA points causes an increase of the noise perturbations and hence degrades the accuracy of the peak location (see Figures 3.6(a-2) and (b-2)). Therefore, the threshold increases to D of 3.2 for the case of a 7-point RA (figure not shown). Conversely, the RMS errors of V_d for a SNR range of ≥ -6 dB did not show large differences between the cases of 13-point and 19-point RAs (see Figures 3.6(b-2) and (c-2)). These results indicate that the degree of noise perturbation suppression does not differ much between the computation method using the 13-point RA and that using the 19-point RA. Therefore, the threshold remains D of 2.5 for the case of 19-point RA.

It is noted that for a D range of $< \sim 2.5$, the estimation error of V_d was significantly large. For the case where $\sigma_{3dB} = 50$ and SNR $= -3$ dB (i.e., $D = 4.8$), the RMS error of V_d was as small as 2.6 for the computation method using a 13-point RA (Figure 3.6(b-2)). For a decreased SNR of -9 dB (i.e., $D = 1.2$), it increased to 18.7. For the case where $\sigma_{3dB} = 90$ and SNR $= -3$ dB (i.e., $D = 2.7$), the RMS error of V_d was 4.6, which was close to that in the high SNR cases. For SNR $= -6$ dB (i.e., $D = 1.3$), it increased to 8.1. These results indicate that the D of 2.5 can be used as a threshold to judge whether or not the errors of the spectral parameters are significantly large. In conclusion, the results shown in Figures 3.9 and 3.10 indicate that the use of D is useful for evaluating the errors of the spectral parameters.

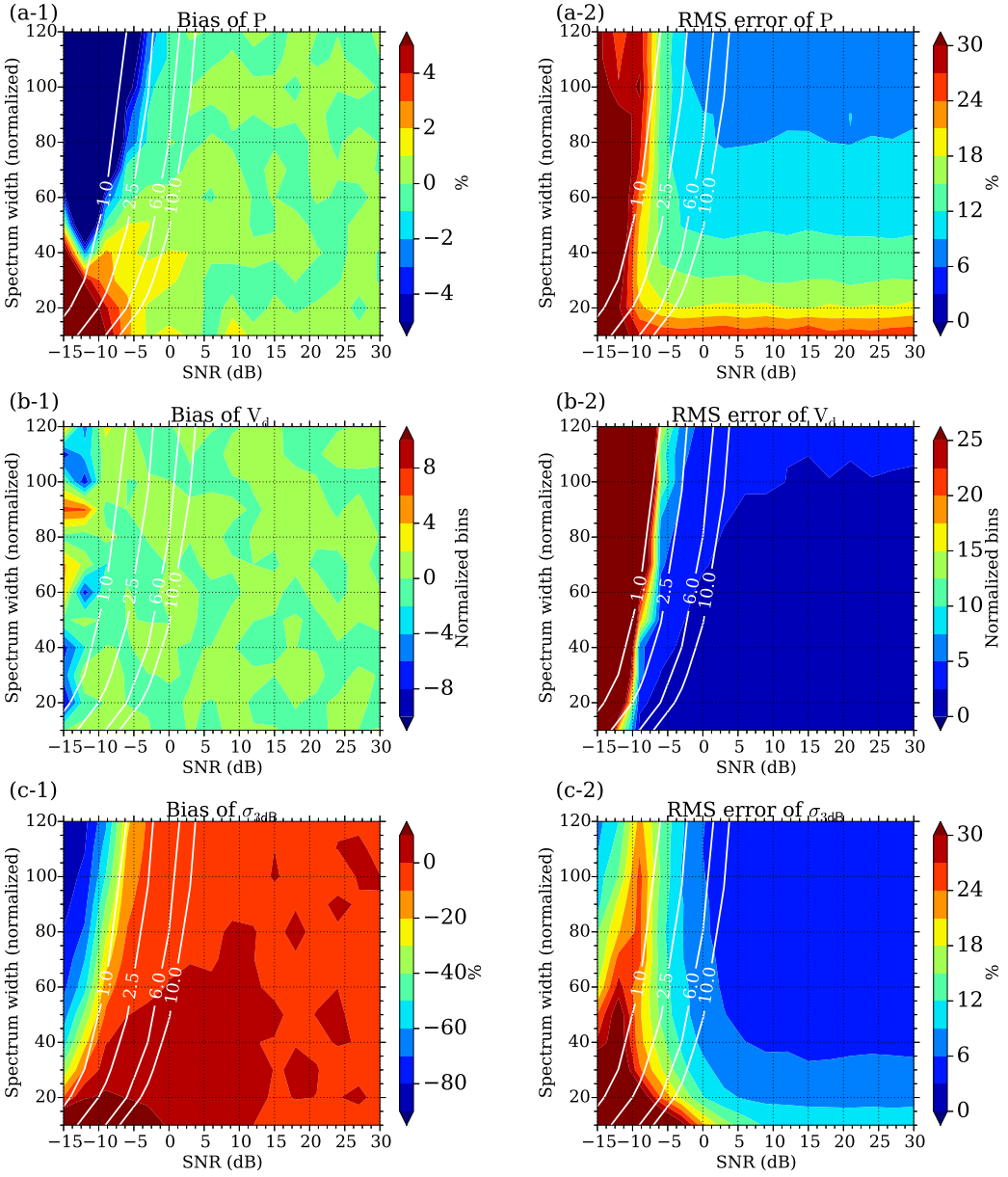

FIGURE 3.9: Distribution of estimation errors of the spectral parameters related to SNR and $\sigma_{3\mathrm{dB}}$. The panels (a-1), (b-1), and (c-1) show distributions of the bias of P, V_d, and $\sigma_{3\mathrm{dB}}$, respectively. The panels (a-2), (b-2), and (c-2) show distributions of the RMS error of P, V_d, and $\sigma_{3\mathrm{dB}}$, respectively. White curves are contours of D calculated using the peak intensity of the modeled echo.

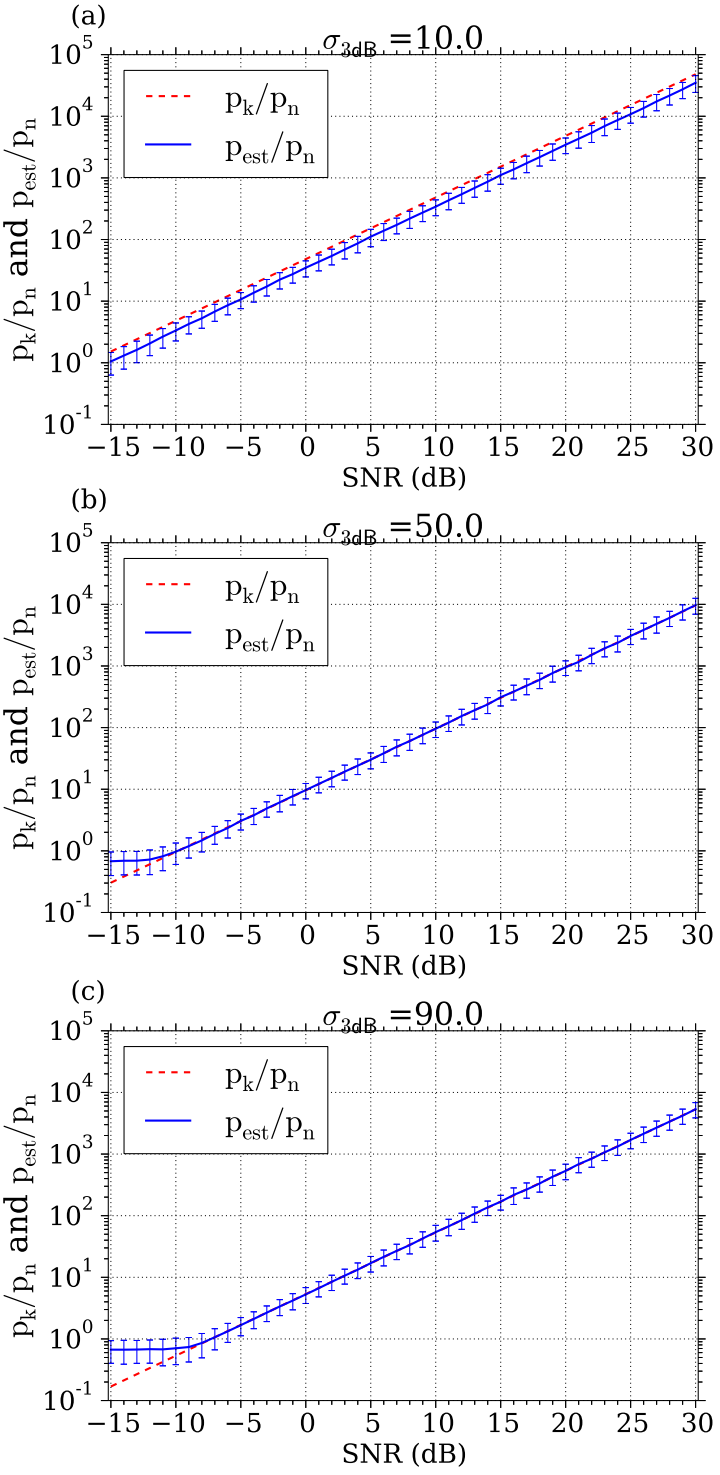

FIGURE 3.10: Relation between SNR and the intensity of the Doppler spectrum smoothed by the 13-point RA at estimated V_d (p_{est}; blue curves). The panels (a), (b), and (c) show cases for the model echoes with σ_{3dB} of 10, 50, and 90, respectively. Error bars are the RMS values of p_{est}. The relationship between SNR and p_k is shown by red dashed curves. From both p_k and p_{est}, p_n is subtracted.

3.3 Considerations for applying incoherent integration

Hereafter we discuss error reduction of the spectral parameters by use of incoherent integration. Incoherent integration times (hereafter N_{icoh}) of 2, 3, and 5 were examined. For calculating the spectral parameters, we used the bottom method with 13-point RA.

3.3.1 Estimation accuracy of echo range

Because accuracy of $R_{\mathrm{est\_RA}}$ determines estimation accuracy of spectral parameters. We compared $R_{\mathrm{est\_RA}}$ calculated by using different incoherent integration times. Figure 3.11 shows the ration of $R_{\mathrm{est\_RA}}$ against $R_{\mathrm{echo\_RA}}$.

For the case σ_{3dB} of 10, $R_{\mathrm{est\_RA}}$ is overestimated because the RA broadens Doppler spectra. With the increase of SNR, the overestimation decreases from 1.49 (-3 dB) to 1.30 (30 dB) for N_{icoh} of 2. For different N_{icoh}, the ratio does not show significant difference. The maximum overestimation for N_{icoh} of 2 is 1.49 and that for N_{icoh} of 5 is 1.53.

For the case σ_{3dB} of 50 (90), with the increase of SNR, the ratio increases. Especially for SNR ≤ -3 dB (0 dB), the ratio shows significant improvement that increases from 0.51 (0.28) to 0.96 (0.92) for the case σ_{3dB} of 50 (90) and N_{icoh} of 2. For the range that SNR ≤ -3 dB (0 dB), the ratio also increases significantly with the increase of N_{icoh} for the case σ_{3dB} of 50 (90). For SNR of -12 dB, the ratio increases from 0.78 (0.41) to 0.98 (0.71) when N_{icoh} increase from 2 to 5 for the case σ_{3dB} of 50 (90).

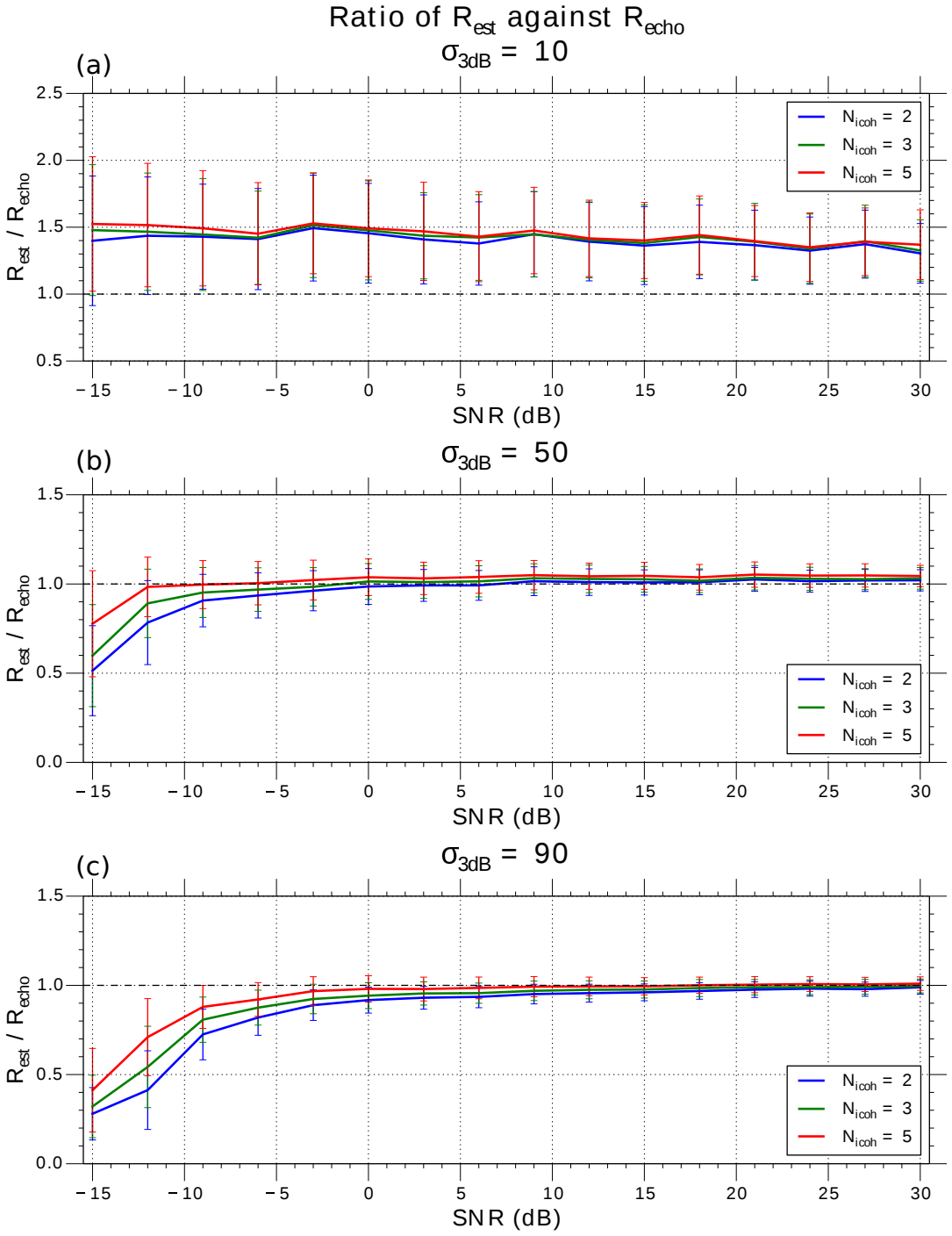

FIGURE 3.11: Ration of $R_{\text{est\_RA}}$ against $R_{\text{echo\_RA}}$ for N_{icoh} of 2, 3, and 5. The panels (a), (b), and (c) show cases for σ_{3dB} of 10, 50, and 90, respectively.

3.3.2 Errors in high SNRs

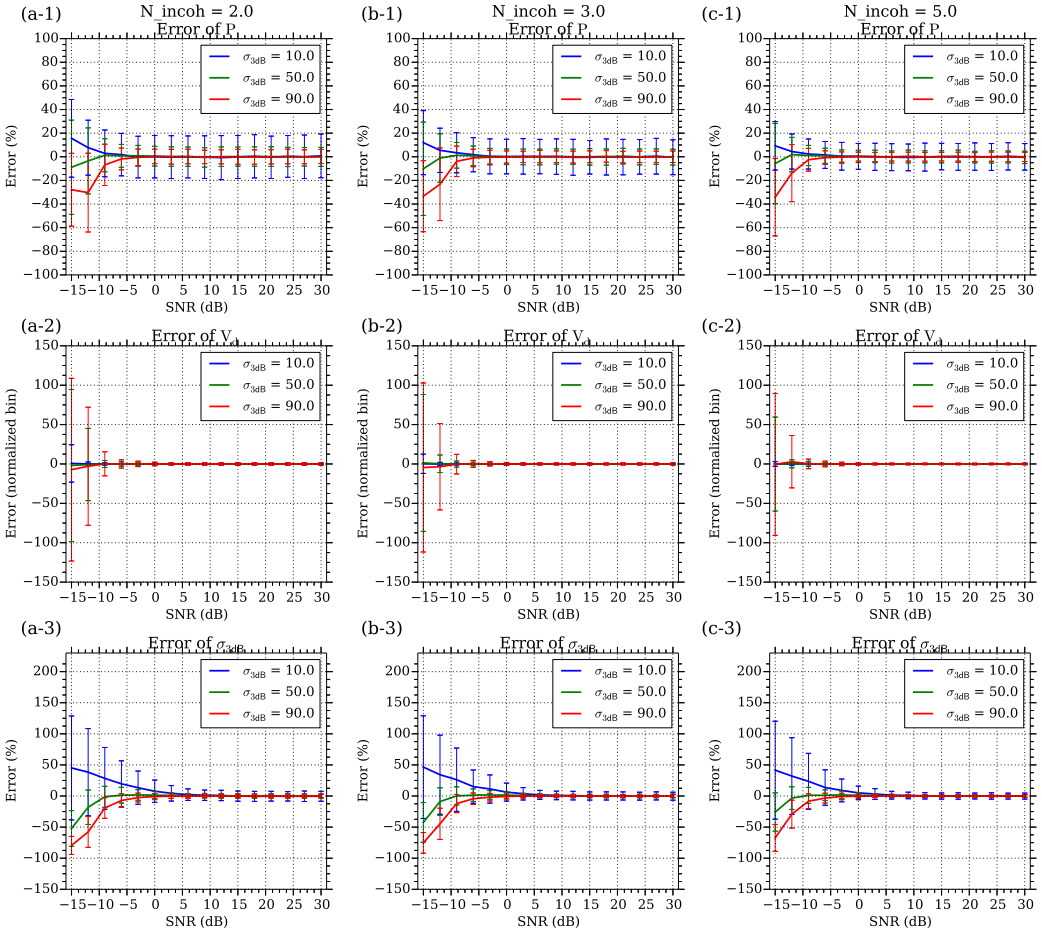

FIGURE 3.12: Same as Figure 3.6 except that incoherent integration is applied and the $R_{\rm est}$ was determined by the Doppler spectrum smoothed by the 13-point RA. The panels (a), (b), and (c) show cases for incoherent integration times ($N_{\rm icoh}$) of 2, 3, and 5, respectively.

The estimation errors of P are described in this sections. For the case without incoherent integration and $\sigma_{\rm 3dB} = 10$, the RMS errors were ∼26.2% for the SNR range of ≥ 0 dB (Figure 3.6(b-1)). For $N_{\rm icoh}$ of 2, 3, and 5, the values decreased to ∼18.1%, 14.9%, and 11.4%, respectively (Figures 3.12(a-1), (b-1), and (c-1)). For the case $\sigma_{\rm 3dB} = 90$ and without incoherent integration, the RMS errors were ∼8.6% for SNRs of ≥ 0 dB. For $N_{\rm icoh}$ of 2, 3, and 5, the values decreased to ∼6.1%, 5.0%, and 3.8%, respectively.

The estimation errors of $V_{\rm d}$ are now described. For a SNR range of ≥ 0 dB and the case without incoherent integration, the RMS errors of $V_{\rm d}$ were ∼0.8 and ∼2.5 for

the cases $\sigma_{3dB} = 10$ and 90, respectively (Figure 3.6(b-2)). By incoherent integration with N_{icoh} of 2, 3, and 5, the RMS errors of V_d decreased to ∼0.6, 0.5, and 0.4 for the case $\sigma_{3dB} = 10$, and to ∼1.7, 1.4, and 1.1 for the case $\sigma_{3dB} = 90$ (Figures 3.12(a-2), (b-2), and (c-2). These results indicate that the RMS error of V_d was reduced up to ∼1.4 by use of incoherent integration with N_{icoh} of 5. It should be noted that even by incoherent integration with N_{icoh} of 2, the RMS error of V_d was significantly reduced (i.e., from 2.5 to 1.7 for the case $\sigma_{3dB} = 90$).

The estimation errors of σ_{3dB} are now described. For a SNR range of ≥ 9 dB and the case without incoherent integration, the RMS error of σ_{3dB} for the model echo with σ_{3dB} of 10 was ∼11.1% (Figure 3.6(b-3)). The errors for the model echo with σ_{3dB} of 10 decreased to ∼8.1%, 6.6%, and 5.0% for N_{icoh} of 2, 3, and 5, respectively (Figures 3.12(a-3), (b-3), and (c-3)). For the model echo with σ_{3dB} of 90 and a SNR range of ≥ 6 dB, the RMS errors were ∼3.7% for the case without incoherent integration. The RMS errors decreased to ∼2.7%, 2.2%, and 1.7% for the cases N_{icoh} = 2, 3, and 5, respectively. These results indicate that the reduction of estimation error is significant for small σ_{3dB}.

3.3.3 Errors in low SNRs

For low SNRs, both bias and RMS errors of the spectral parameters for echoes with large σ_{3dB} were reduced significantly by incoherent integration. For the case σ_{3dB} = 90 and without incoherent integration, the error of P for a SNR of −9 dB was −19.4 ± 29.0%, respectively (Figure 3.6(b-1)). By incoherent integration with N_{icoh} of 2, 3, and 5, the errors decreased to −6.8 ± 17.5%, −3.9 ± 12.9%, and −2.5 ± 9.6%, respectively (Figures 3.12(a-1), (b-1), and (c-1)). For the same σ_{3dB} and SNR, the RMS error of V_d without incoherent integration was 50.9 (Figure 3.6(b-2)). By incoherent integration with N_{icoh} of 2, 3, and 5, the errors decreased to 15.3, 12.5, and 6.1, respectively (Figures 3.12(a-2), (b-2), and (c-2)). For the same σ_{3dB} and SNR, the error of σ_{3dB} was −40.1 ± 24.9% (see Figure 3.6(b-3)). By incoherent integration with N_{icoh} of 2, 3, and 5, the values decreased to −19.3 ± 16.6%, −12.2 ± 14.6%, and −8.4 ± 11.8%, respectively (Figures 3.12(a-3), (b-3), and (c-3)).

3.3.4 Trade-off between time resolution and the estimation error

In high SNRs, the results of numerical simulation show that incoherent integration is useful especially for reducing the estimation errors of echoes with small $\sigma_{3\mathrm{dB}}$ (see Section 3.3.2). However, incoherent integration in high SNRs needs to be applied carefully by considering the time scale of atmospheric phenomena. For the MU radar, the measurement times for N_{icoh} of 2, 3, and 5 are 98.3 s, 147.5 s, and 245.8 s, respectively (Table 3.1). For the RIM LQ-7, the measurement times are 21.3 s, 31.9 s, and 53.2 s for N_{icoh} of 2, 3, and 5, respectively (Table 3.1). The degradation of the time resolution is large especially for the MU radar because it uses a frequency band as low as 50 MHz. Because the degradation of time resolution causes changes in the echo characteristics (i.e., P, V_{d}, and $\sigma_{3\mathrm{dB}}$) within a particular measurement time, N_{icoh} must be determined so that the time resolution is sufficiently smaller than the time scale of atmospheric phenomena measured by ARs.

In low SNRs, because a Doppler spectrum with greater $\sigma_{3\mathrm{dB}}$ has smaller p_{k} for an identical SNR, incoherent integration is especially useful for echoes with large $\sigma_{3\mathrm{dB}}$ (see Section 3.3.3). It is recommended that N_{icoh} is determined by considering both p_{est} and the SNR. Because the estimation error is most significant for $\sigma_{3\mathrm{dB}}$, the error assessment as shown in Figures 3.12(a-3), (b-3), and (c-3) is useful for determining N_{icoh}. It should be noted that incoherent integration with N_{icoh} of only 2 can significantly reduce the errors of the spectral parameters, and spectrum perturbations will be reduced by a factor of only $1/\sqrt{N_{\mathrm{icoh}}}$. Therefore, it is recommended that N_{icoh} is minimized as much as possible for AR measurements with high time resolution.

3.4 High resolution measurement of the boundary layer by RIM LQ-7

For observations, the ARs can be combined use with other remote sense techniques. By combined use GPS, microwave radiometer, AR, and weather radar, the detailed structure of the boundary layer was studied (e.g., *Endo et al.* [2008] and *Gaffard*

et al. [2008]). By combined use lidar and AR, the vertical air motion measured by the AR and that measured by the lidar were evaluated [*Wingo et al.*, 2015]. Lidar and AR were used to measure the boundary layer height and entrainment zone thickness [*Cohn et al.*, 2000]. In this section, we show the measurement results by using AR, lidar, radiosonde, and all-sky camera. The spectral parameter estimation method discussed in this chapter was used. In this observation, we used RIM LQ-7 that was shown in Section 2.3. Because the RIM was used, the range resolution can be improved to several tens meters which is much better than the normal LQ-7 observation.

Figures 3.13 and 3.14 show time-height plots of P, vertical air velocity (W), and $\sigma_{3\mathrm{dB}}$, normalized relative backscatter (NRB) during a period between 08:00 and 16:00 Japan standard time (JST) on 5 and 6 November 2013. For the RIM LQ-7, 10-times oversampling was used. Therefore, the range interval is 15 m. As described in Section 3.1.1, T_{obs} is 10.6 s. NRB was measured by a Mie lidar which locates at $\sim$192 m southwest from the RIM LQ-7. The lidar beam points to south with zenith angle of 30°. In order to reduce the data size, lidar data was averaged over 1 minute. Figure 3.13(d) indicates that the Mie lidar echo intensity is largely enhanced below 1.0–1.5 km altitude. The lower region with high echo intensity corresponds to the boundary layer. From Figure 3.13(a) we can find that the RIM LQ-7 echo intensity is also enhanced at the top boundary of the boundary layer. On November 6, on the other hand, we did not find clear top boundary of the boundary layer. The Mie lidar also did not show clear boundary layer. The echo intensity at $\sim$2 km is larger on November 6 than that on November 5. Data quality of the vertical winds is better on November 6 at high range. Fluctuations of the vertical wind are, on the other hand, much larger on November 5 compared with those on November 6. We will later discuss comparisons between the RIM LQ-7 and the Mie lidar.

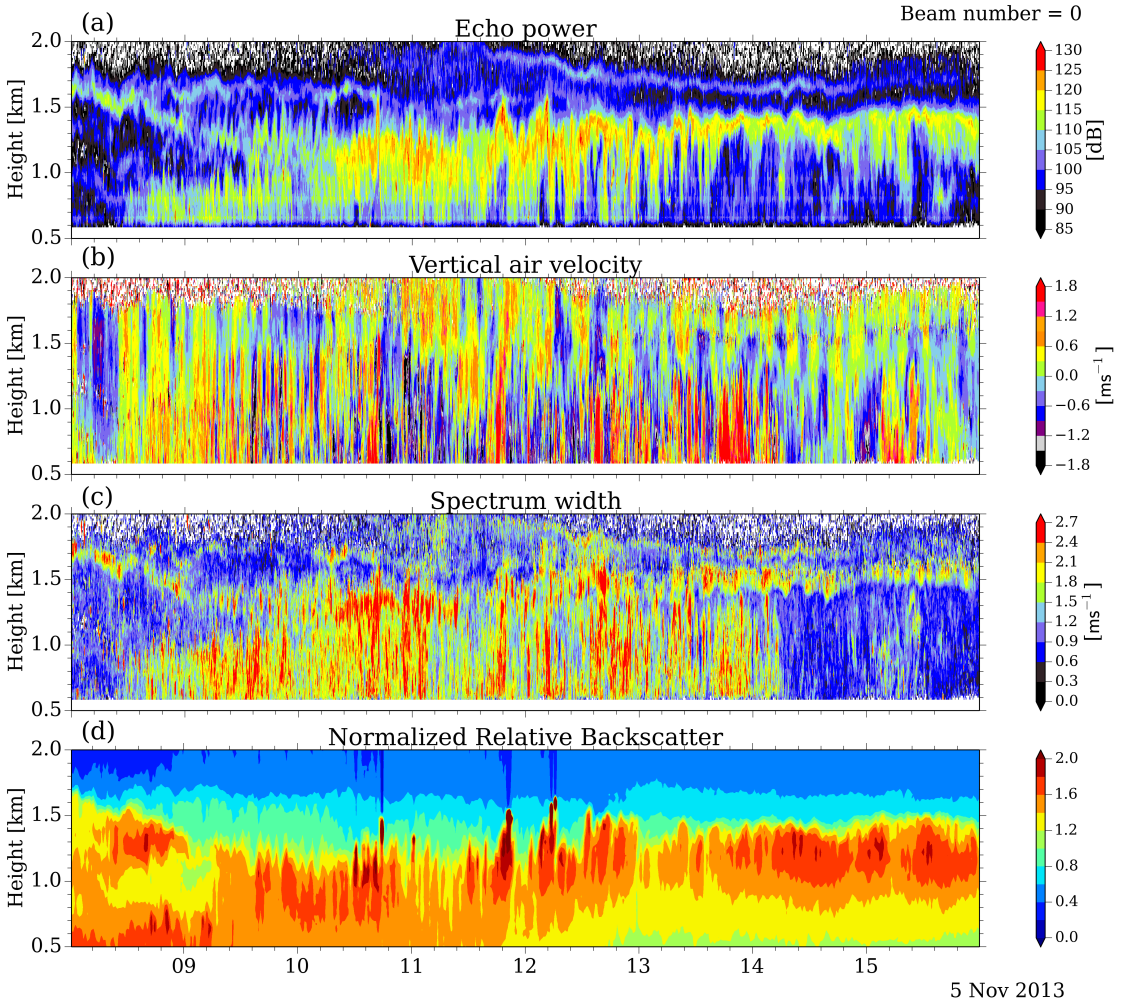

FIGURE 3.13: (a) Time-height plot of P, (b) vertical air velocity (W), (c) $\sigma_{3\mathrm{dB}}$ collected by the vertical beam of the RIM LQ-7 and produced by the bottom method with 13-point RA. (d) Normalized Relative Backscatter (NRB) measured by a Mie lidar. The data were collected during a period between 08:00 and 16:00 Japan standard time (JST) on 5 November 2013.

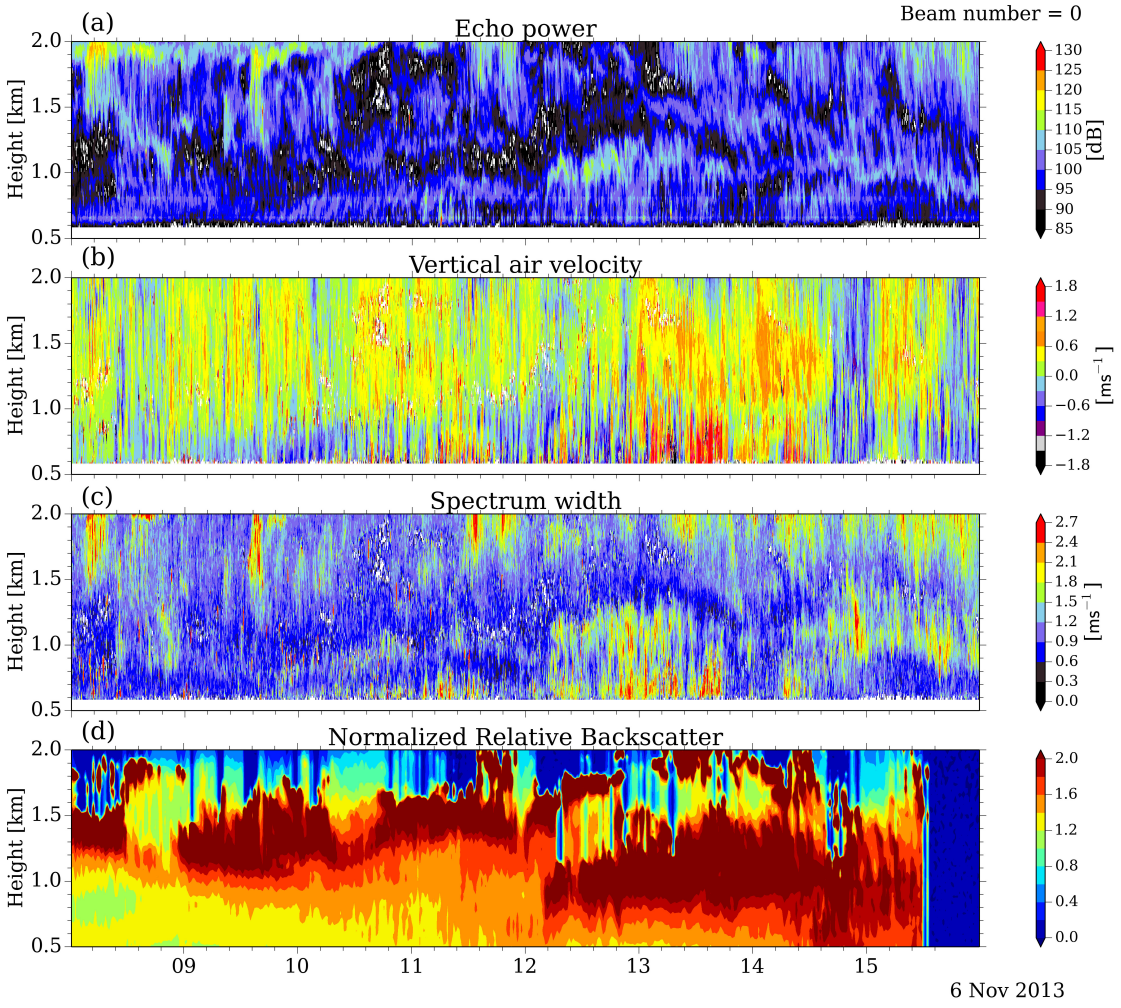

FIGURE 3.14: Same as Figure 3.13 except that the data were collected on 6 November 2013.

By using the averaged W ($\overline{W}$) over 10 records as a true value, we calculated the estimation errors of W ($\epsilon_V = W - \overline{W}$). We selected a time period between 13:00 and 14:30 on 6 November 2013 (see Figure 3.14) that the perturbation of W is relatively small. Figure 3.15 shows the relation between RMS values of ϵ_V and the averaged σ_{3dB}. It is noted that data collected at a height range between 1.0 km and 1.5 km were used. Figure 3.15(b) shows the scatter plot by limiting the y-axis in a range between 0.00 and 0.50. The σ_{3dB} values were averaged over 10 records. The blue curve indicates the RMS values of ϵ_V calculated from simulation results. The results shown in Figure 3.6(b-2) and in a SNR range between 6 dB and 30 dB were used. Compared with the simulation results, the measured results have large

RMS values because the measured W has perturbation. Estimation error from the simulation (blue curve) supports lower boundary of the wind fluctuation, which is reasonable behavior. It is noted that the RMS values are mainly smaller than 0.3 m s^{-1}. For both the simulation results and measurement results, the RMS values of ϵ_V increase with the increase of σ_{3dB}.

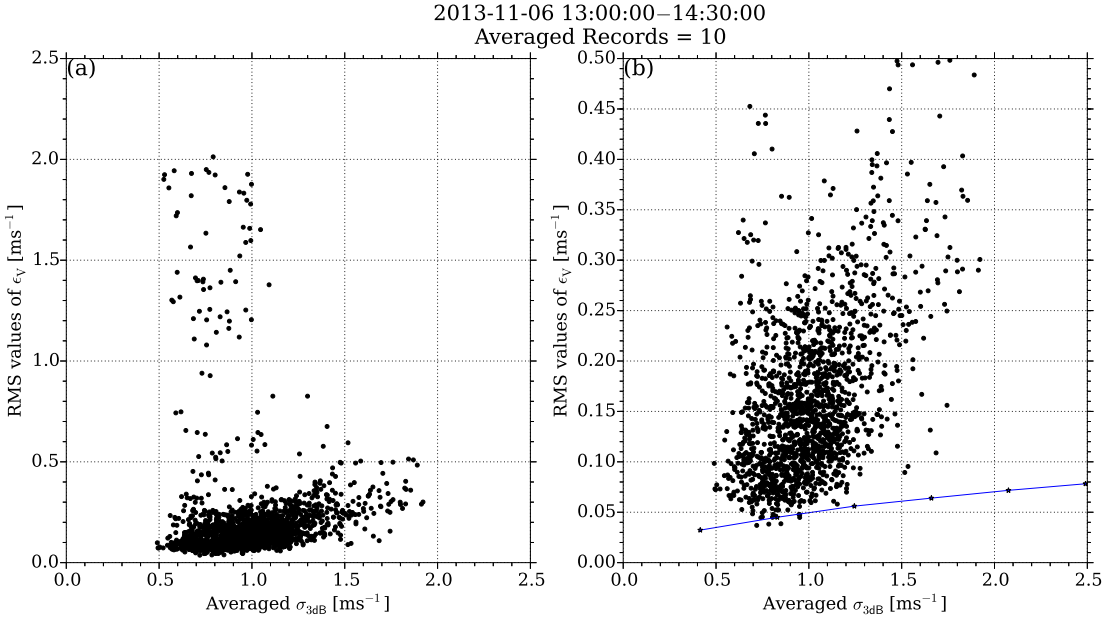

FIGURE 3.15: Scatter plot between averaged σ_{3dB} and RMS values of ϵ_V. The difference between (a) and (b) is the value of y-axis. The blue curve in (b) indicates the relation between σ_{3dB} and RMS values of ϵ_V from simulation results.

Figure 3.16 shows the horizontal velocity measured by the RIM LQ-7 and radiosonde. The radiosonde was launched on 12:27 JST, 6 November 2013. If the wind velocity is uniform over the radar, the horizontal component of the wind velocity v_h is given by

$$v_h = \frac{v_r - v_z \cos\theta}{\sin\theta}, \tag{3.5}$$

where v_r is the Doppler velocity measured by the oblique beam, v_z is the Doppler velocity measured by the vertical beam, θ is the zenith angle of the oblique beam. For the RIM LQ-7, θ is 14.2°. By using v_z and v_r measured by the east beam, the zonal (east-west) wind velocity can be calculated. By using v_z and v_r measured by the north beam, the meridional (south-north) wind velocity can be calculated. In order to ensure the correctness of velocity measurement, we selected the height

range where the averaged P is sufficient high (i.e., $\geq$ 80 dB). Because the random perturbations of v_{r} and v_{z} affect the calculation accuracy of the horizontal velocity. In order to minimize the perturbations, v_{r} and v_{z} were averaged over 20 minutes (10 minutes before and after the launch time of radiosonde). After 20 minutes average, the mean and standard deviation values of Doppler velocity for the vertical, north, east beams are 0.04 $\pm$ 0.10 m s^{-1}, 1.49 $\pm$ 0.39 m s^{-1}, and 1.10 $\pm$ 1.30 m s^{-1}, respectively.

We discuss the comparison of wind from the RIM LQ-7 and the radiosonde. The radiosonde that climbs upward has pendulum motion. This is the reason of large fluctuation of 1-second wind (green curves). The 2-second wind (red curves), the standard data from the Vaisala radiosonde measurement, is the result of further smoothing by the Vaisala software. The pendulum motion of the radiosonde, however, can differ from a simple swing owing to its shape and by the inhomogeneous turbulent motion of the surrounding atmosphere. The 2-second wind of the radiosonde shows good agreement to the RIM LQ-7 wind (blue curves). Small northward shift of radiosonde 2-second wind above 1.25 km may reflect horizontal wind shear in the height region. Also there are some discrepancies between the 2-second wind and the RIM LQ-7 wind, for example, the meridional wind at $\sim$1.05 km and the zonal wind at $\sim$0.9 km, $\sim$1.1 km, and $\sim$1.2 km. These occur when the 1-second wind shows different swing motion from most of the other height range, which is understandable from characteristics of the radiosonde observations. Potential reason of these discrepancies is inhomogeneous wind field, but further discussion is out of scope of this study. Summarizing these discussion above, we can conclude successful horizontal wind estimation by the RIM LQ-7 and enhanced height-resolution observations.

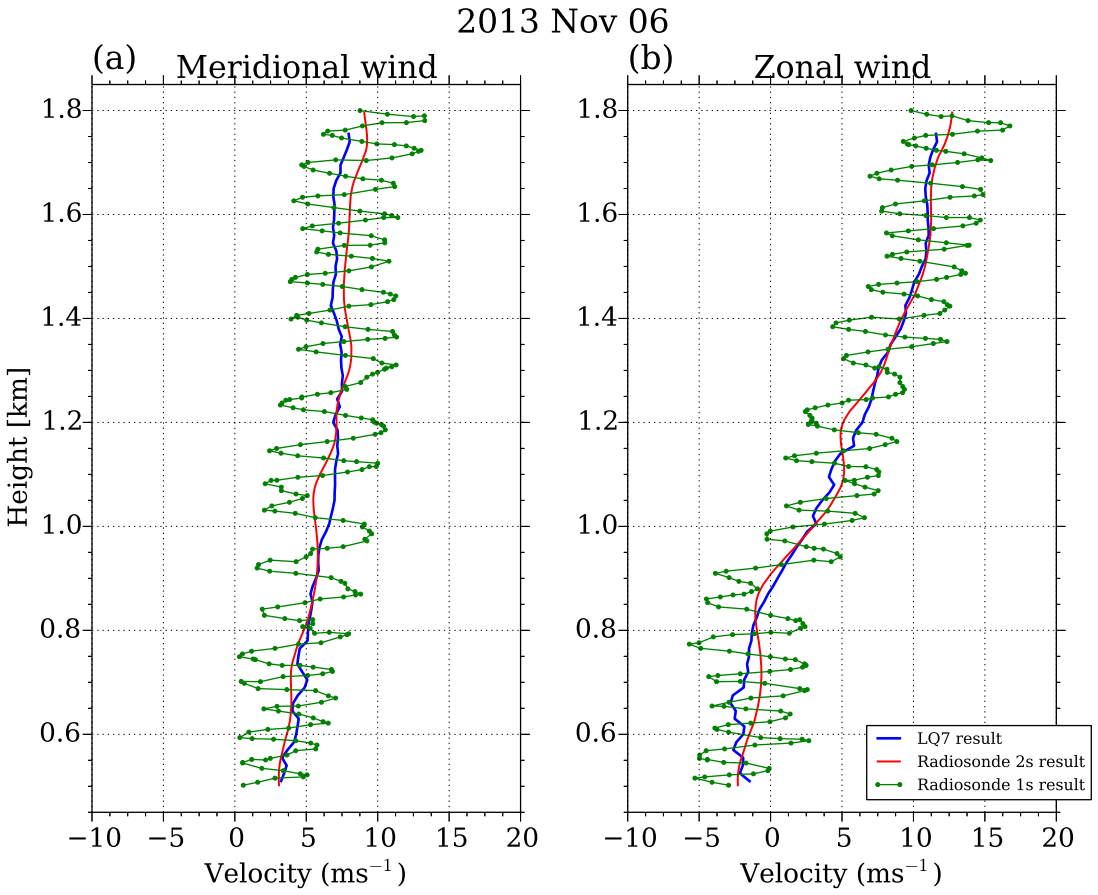

FIGURE 3.16: Height profiles of (a) meridional and (b) zonal wind calculated by the RIM LQ-7 (blue curves), 2-second radiosonde data (red curves), and 1-second radiosonde data (green curves). Green dots show data points of the 1-second radiosonde data. The radiosonde was launched on 12:27 JST, 6 November 2013.

Figure 3.17 shows time-height plots of spectral parameters and NRB between 10:30 and 11:00 JST on 5 November 2013. During the period between ∼10:41 and ∼10:43, P and W showed significant change at a height range between ∼1.0 km and ∼1.6 km. Correspondingly, NRB also showed significant change ∼2 minutes later. Using images taken by a all-sky camera, we show the consistency between the measurement of RIM LQ-7 and that of lidar (see Figure 3.18). The all-sky camera locates at ∼37 m northwest from the RIM LQ-7 and ∼187 m southeast from the lidar. The cross points of the brown circle and the brown line indicate the center of the vertical beam of the RIM LQ-7. The cross points of the pink circle and the pink line indicate the center of the beam of the lidar. At ∼10:41, a cloud approached the

observation area of the RIM LQ-7 and passed by at ∼10:43. This cloud approached the observation area of the lidar at ∼10:43 and passed by at ∼10:45. The results of all-sky camera indicate that the measurement results of RIM LQ-7 and those of lidar have good consistency. The results indicate that because of the high time and range resolution, RIM LQ-7 can measure the enhancement of downward and upward motion of clear-air associated with boundary layer clouds.

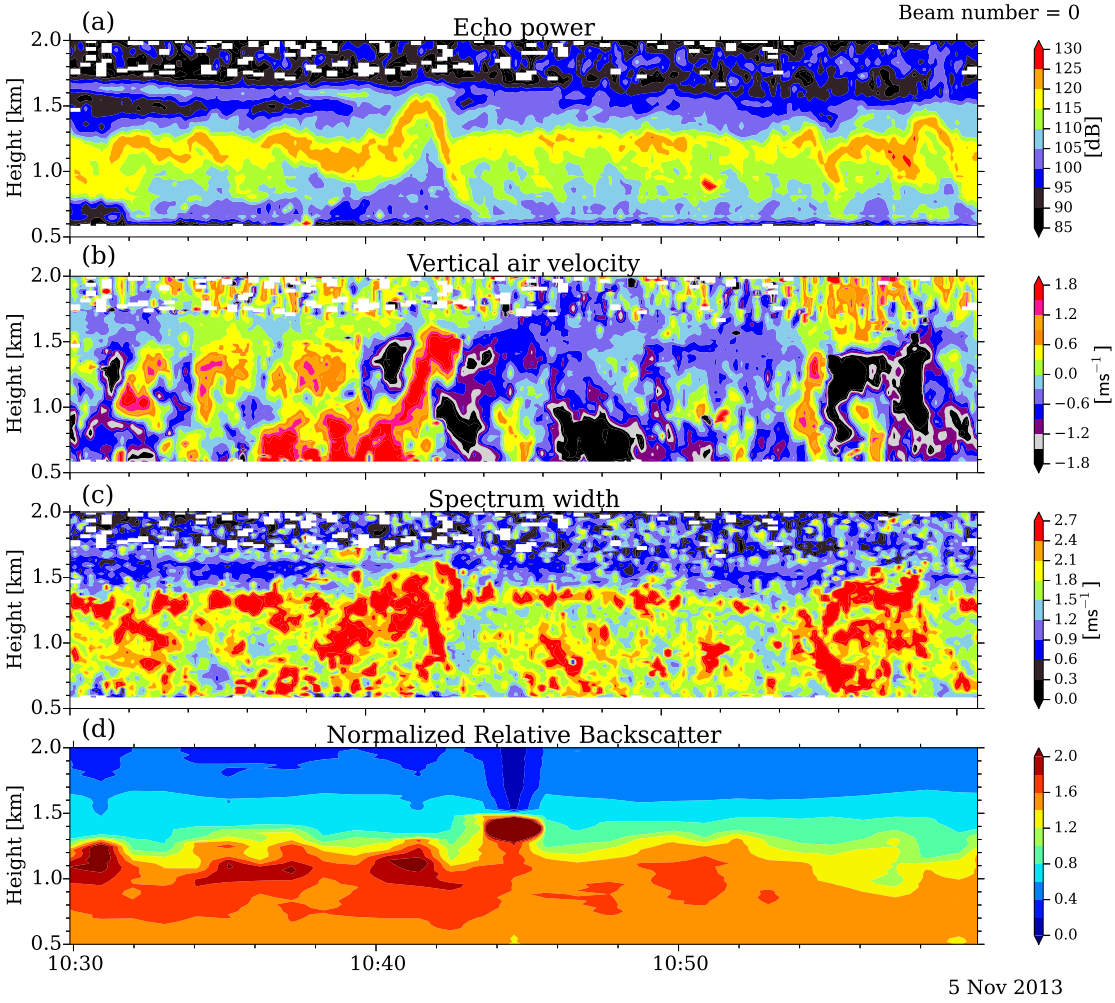

FIGURE 3.17: Same as Figure 3.13 except that the data were collected during a period between 10:30 and 11:00 JST on 5 November 2013.

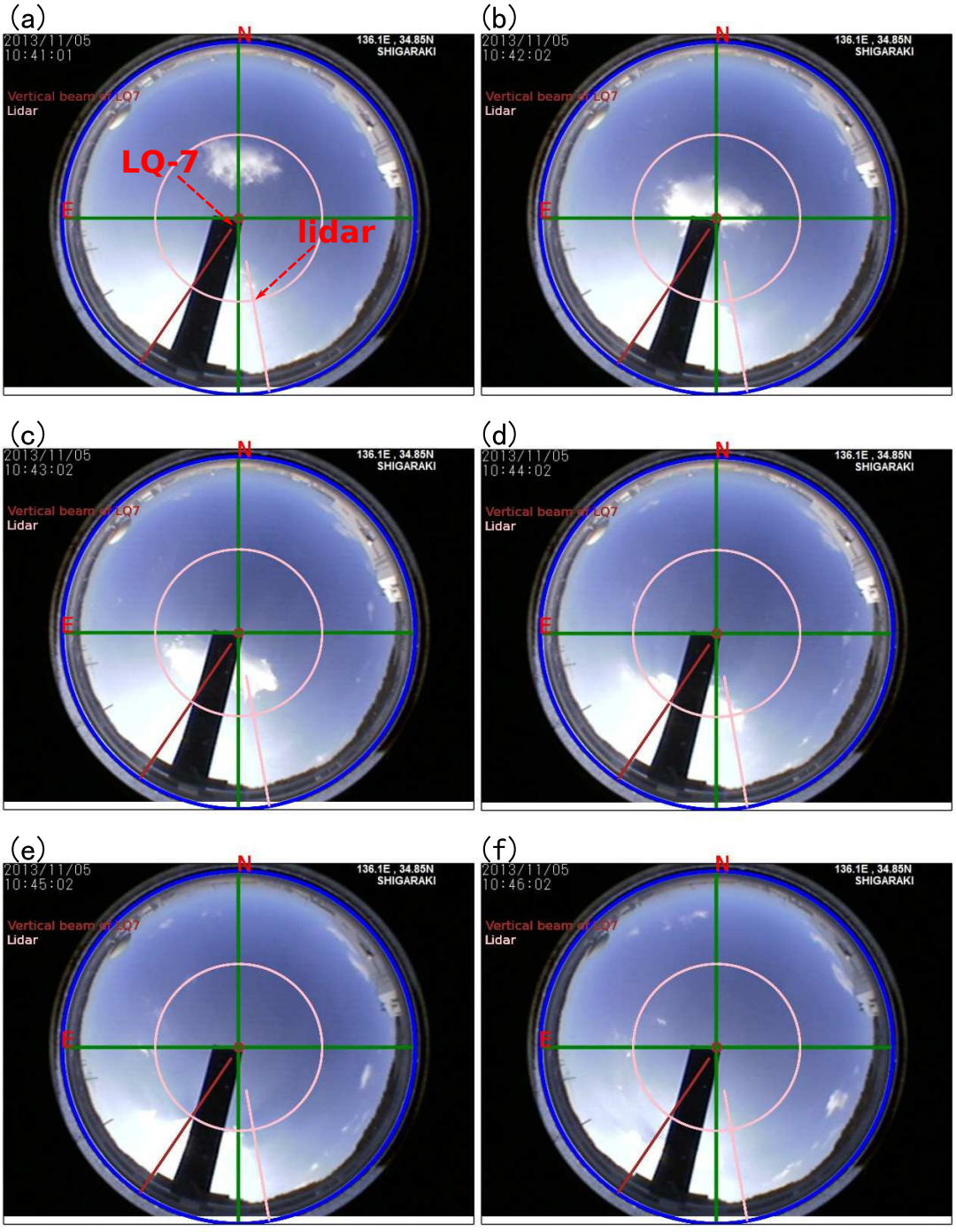

FIGURE 3.18: Images taken from a all-sky camera during a period between 10:41 and 10:46 JST on 5 November 2013. The brown circle indicates the horizontal distance between the vertical beam of the RIM LQ-7 and the all-sky camera at 1.4 km height. The brown line indicates the projection of the vertical beam of the RIM LQ-7 to the all-sky camera at 1.4 km height. Therefore, the cross point of the brown circle and the brown line indicates the center of the vertical beam of the RIM LQ-7 at 1.4 km height. The pink circle and pink line indicate the same but for the lidar. The cross point of the pink circle and the pink line indicates the center of the lidar beam at 1.4 km height. The center of the vertical beam of the RIM LQ-7 and that of the lidar beam are indicated by red arrows in panel (a).

3.5 Summary

In this chapter, using numerical simulation, we investigated methods for calculating the spectral parameters from Doppler spectra collected by high-resolution ARs. Because high-resolution ARs produce a huge amount of Doppler spectra, calculation methods must be simple and fast. Further, in order to attain high-resolution, the use of incoherent integration should be avoided as much as possible. It is recommended that N_{icoh} is determined by considering both D and the SNR. By using the bottom method with 13-point RA, we processed the data collected by the RIM LQ-7. Our measurement showed the enhancement of upward motion of clear-air associated with boundary layer clouds because of the high time and range resolution. The results indicate that the high time and range resolution observations with the RIM LQ-7 are useful for observing the boundary layer.

Chapter 4

Spectral parameters estimation in precipitation for 50-MHz band atmospheric radars

4.1 Computation methods for the spectral parameters

4.1.1 Computation method using the echo peak level (Top method)

In this chapter, the computation methods for calculating the spectral parameters in precipitation region are described. First, the computation method using the echo peak level (EPL; top method) is described. The top method can be used when clear-air echoes are well separated from hydrometeor echoes. Therefore, the top method is useful for raindrops with large fall velocity ($\sim$5–10 m s^{-1}) and solid hydrometeors whose peak echo intensity is much smaller than the clear-air echoes.

4.1.1.1 Signal processing method

Figure 4.1 shows a flow chart of the top method. In order to explain the top method, an example is presented in Figure 4.2(a).

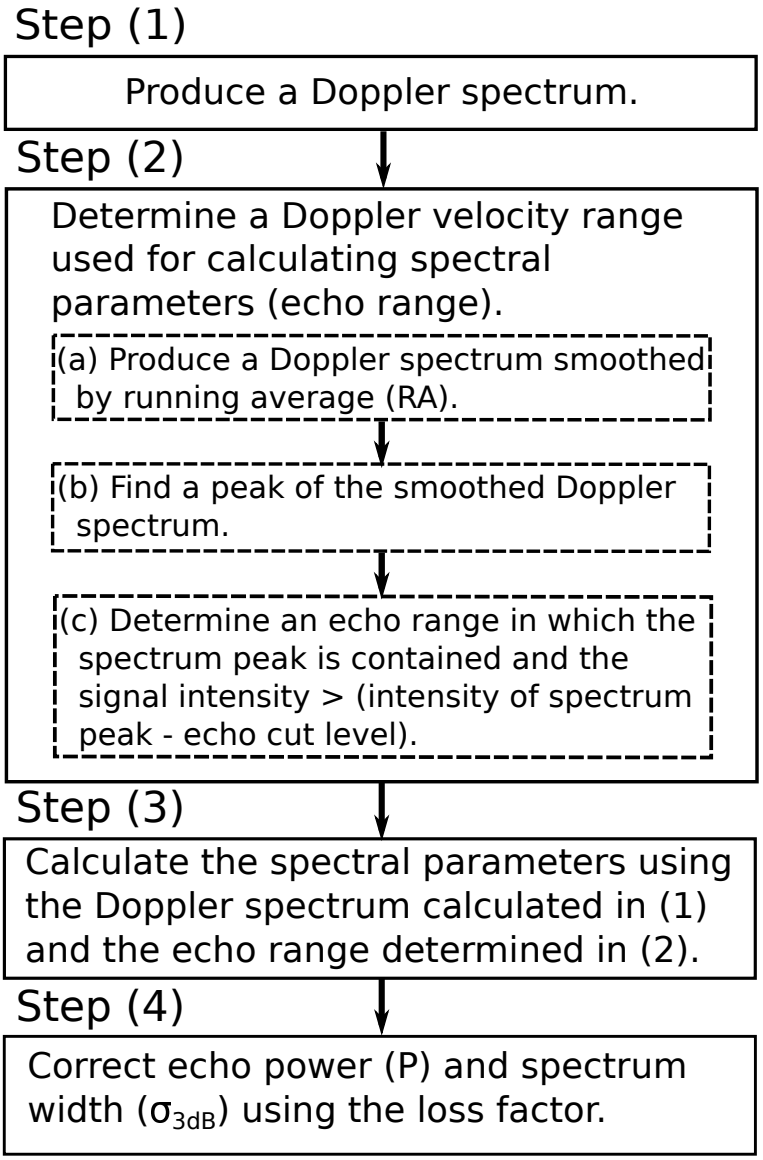

FIGURE 4.1: Flow chart of a computation method for the top method.

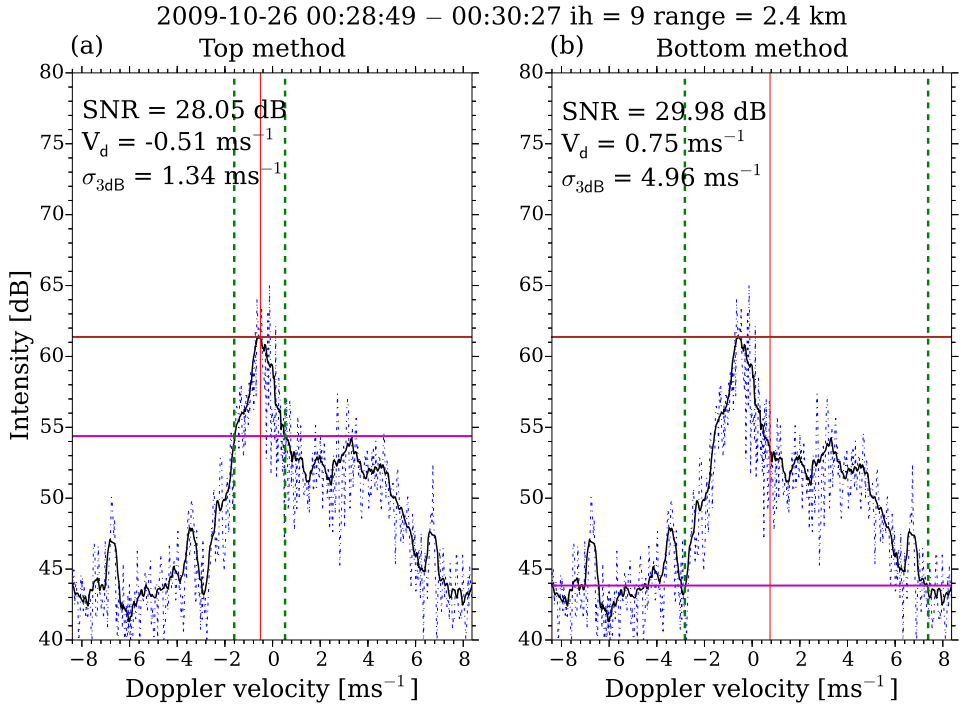

FIGURE 4.2: (a) Spectral parameters calculated by the top method with L of 7 dB, and (b) the bottom method. The Doppler spectrum was collected by the vertical beam of the MU radar during a period between 00:28:49 and 00:30:27 JST on 26 October 2009 at 2.4 km height. The blue dashed curves are the collected Doppler spectrum. The black curves are the Doppler spectrum smoothed by a 13-point running average (RA). The horizontal brown lines are the echo peak level (EPL). The horizontal purple lines in panels (a) and (b) are the echo cut level (ECL) and the noise level, respectively. The vertical green dashed lines are the edges of echo range (R_{echo}). The vertical red solid lines are V_{d}.

The top method has four steps. In Step (1), a Doppler spectrum is produced. In Step (2), Doppler spectrum points used for calculating the spectral parameters are selected. In the example, the clear-air echo exists in the Doppler velocity range between ~ -2.0 and $\sim$1.5 m s^{-1} and the hydrometeor echo exists between $\sim$1.5 and $\sim$5.5 m s^{-1} (Figure 4.2(a)). In order to select only the clear-air echo, we determine a Doppler spectrum range (hereafter R_{echo}) used for calculating the spectral parameters. Within R_{echo}, because of perturbations of the Doppler spectrum, some Doppler spectrum points shown by the blue dotted curve have intensities smaller than the echo cut level (ECL) even in the vicinity of the peak of the clear-air echo (see Figure 4.2(a)). Therefore, in Step (2a), by following the discussion in Chapter 3, RA is used for producing the smoothed Doppler spectrum (see black curve in

Figure 4.2(a)). In Step (2b), we find an EPL using the smoothed Doppler spectrum (see brown line in Figure 4.2(a)). In order to improve estimation accuracy of EPL, it is recommended that a Doppler velocity range used for determining the location of EPL is limited. If an appropriate Doppler velocity range is given by manually or automatically, the top method can be used to both a vertical beam and oblique beams. Then, in Step (2c), we calculate an ECL from the EPL. ECL is the level where the echo intensity is L dB smaller than the EPL (see purple line in Figure 4.2(a)). By using the ECL, we determine R_{echo} in which the peak of the clear-air echo is contained and all the smoothed Doppler spectrum points have intensities greater than the ECL (see green dashed lines in Figure 4.2(a)).

In Step (3), we calculate the spectral parameters using the Doppler spectrum points within R_{echo}. The moment method is used for calculating the spectral parameters. The results of Chapter 3 indicate that a use of low-pass filtered Doppler spectrum causes overestimation of $\sigma_{3\mathrm{dB}}$. Therefore, the Doppler spectrum calculated in Step (1) (i.e., without smoothing) is used for calculating the spectral parameters.

In Step (4), the underestimation of P and that of $\sigma_{3\mathrm{dB}}$ are corrected. Because R_{echo} does not contain all the components of the clear-air echo, the calculated P and $\sigma_{3\mathrm{dB}}$ are underestimated. By assuming that the clear-air echo follows Gaussian distribution as Y88, the relation between the underestimation of P and L is calculated as

$$f_{\mathrm{P\_loss}} = 1 - \frac{2}{\sqrt{\pi}} \cdot \int_{0}^{\sqrt{\frac{L}{10}\cdot \ln 10}} e^{-t^2} \mathrm{d}t, \tag{4.1}$$

where $f_{\mathrm{P\_loss}}$ is the loss factor of P. As for $\sigma_{3\mathrm{dB}}$, the relation between the underestimation and L is calculated as

$$f_{\sigma\_\mathrm{loss}} = 1 - \frac{\int_{-t_0}^{t_0} \frac{t^2}{\sqrt{2\cdot\pi}} \cdot \exp(\frac{-t^2}{2}) \mathrm{d}t}{\int_{-t_0}^{t_0} \frac{1}{\sqrt{2\cdot\pi}} \cdot \exp(\frac{-t^2}{2}) \mathrm{d}t}, \tag{4.2}$$

where f_{σ_loss} is the loss factor of $\sigma_{3\mathrm{dB}}$ and t_0 is equal to $\sqrt{\frac{L}{5} \cdot \ln 10}$.

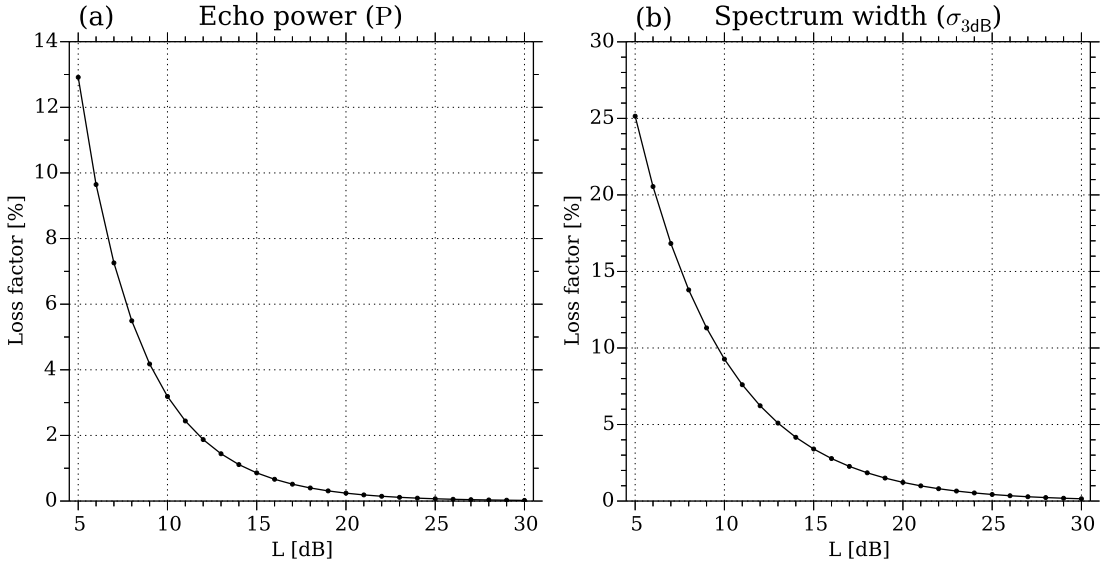

FIGURE 4.3: (a)Relation between L and the loss factor for echo power ($f_{\mathrm{P\_loss}}$), and (b) that for spectrum width (f_{σ_loss}).

Figure 4.3 shows the relation between L and $f_{\mathrm{P\_loss}}$ and that between L and f_{σ_loss}, respectively. For L of 5 dB, $f_{\mathrm{P\_loss}}$ and f_{σ_loss} are 12.9% (0.129) and 25.1% (0.251), respectively. For L of 10 dB, $f_{\mathrm{P\_loss}}$ and f_{σ_loss} decrease to 3.2% (0.032) and 9.3% (0.093), respectively. Compared with the underestimation of P, the underestimation of σ_{3dB} is greater. Using the loss factors, the underestimation is corrected as

$$P_{\mathrm{cor}} = \frac{P}{1 - f_{\mathrm{P\_loss}}}, \tag{4.3}$$

and

$$\sigma_{\mathrm{3dB\_cor}} = \frac{\sigma_{\mathrm{3dB}}}{1 - f_{\sigma\_\mathrm{loss}}}, \tag{4.4}$$

where P_{cor} and $\sigma_{\mathrm{3dB\_cor}}$ are the corrected echo power and the corrected spectrum width, respectively.

Figure 4.2(b) shows the results calculated by the bottom method. In the bottom method, the noise level is used to determine R_{echo}. R_{echo} was as large as 312 because it contained both the clear-air echo and the raindrop echo. V_{d} was 0.75 m s^{-1}, and was apart from the peak location of the clear-air echo (-0.56 m s^{-1}). σ_{3dB} was as large as 4.96 m s^{-1}. By using the top method with L of 7 dB (Figure 4.2(a)), R_{echo} contained only the clear-air echo. Therefore, R_{echo} reduced to 66. V_{d} was -0.51 m

s^{-1}, and was close to the peak location of the clear-air echo (-0.56 m s^{-1}). σ_{3dB} also reduced to 1.34 m s^{-1}.

4.1.1.2 Performance evaluation using numerical simulation

By using numerical simulation, we investigate relations between estimation errors of the spectral parameters and ECL. Figure 4.4 shows an example of the simulated Doppler spectrum and estimated spectral parameters.

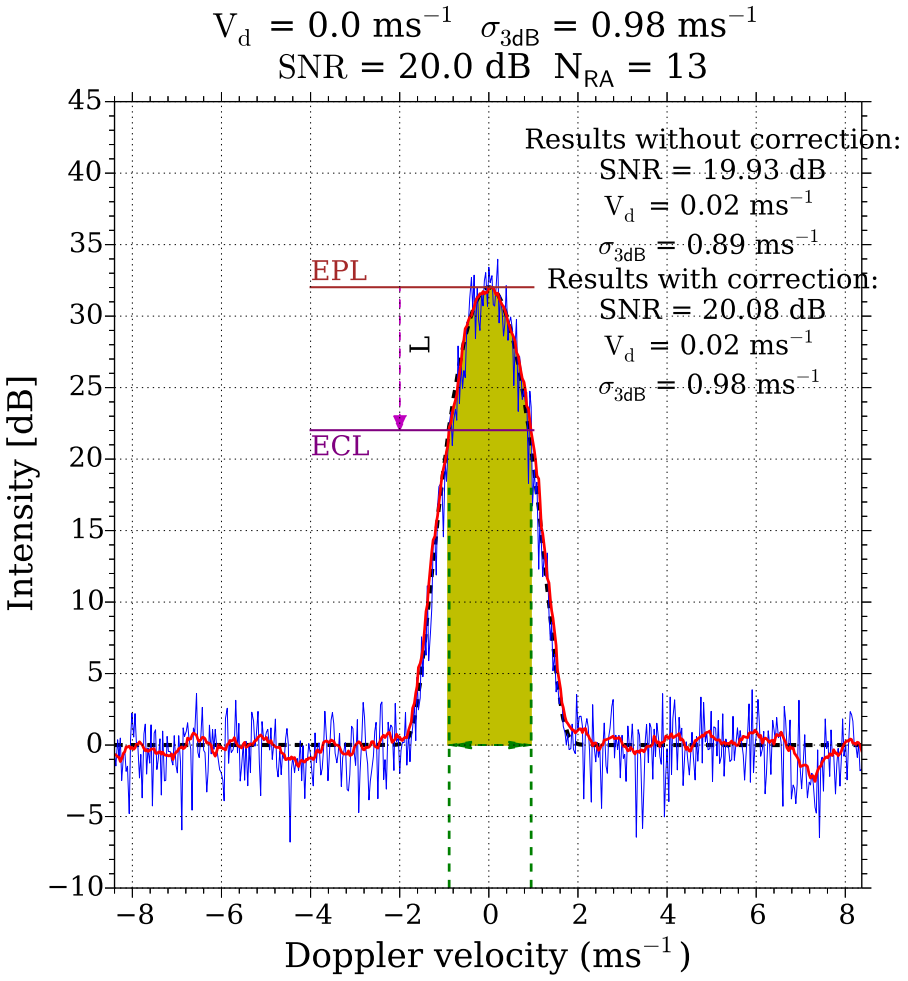

FIGURE 4.4: Example of a simulated Doppler spectrum used for evaluating the ECL of the top method. The blue curve is the simulated Doppler spectrum. The red curve is a Doppler spectrum smoothed by a 13-point RA. The black dashed curve is a modeled spectrum. The horizontal brown line is the EPL. The horizontal purple line is the ECL. L is equal to 10 dB. The green broken lines are the edges of R_{echo}. The yellow-colored region is the region calculated as uncorrected P.

In order to focus on effects of ECL, we presumed that only a clear-air echo and white noise existed in a Doppler spectrum (i.e., hydrometeor echoes, external interferences and clutters are not considered). The noise intensity of each Doppler spectrum point (p_{n}) was set to 0 dB. Therefore, the value of noise power (P_{N}) is equal to the number of the Doppler spectrum points. SNR is defined by P/P_{N}. As the description in Chapter 3, we produced a Doppler spectrum by assuming that the Doppler spectrum follows Gaussian distribution and has perturbations following χ^2 distribution with 2 degrees of freedom.

We set the simulation parameters by referring the measurement parameters of the MU radar on 26 and 27 October 2009 (see Table 4.1). In order to improve range resolution by using range imaging, the MU radar used five frequencies with a 1-MHz span. However, vertical resolution of 150 m, which was determined by the transmitted subpulse of 1 μs, was sufficient for this study [*Mega et al.*, 2012]. Therefore, Doppler spectra collected by the five frequencies were averaged in order to reduce their perturbations. Because the averaging for Doppler spectra collected by the MU radar is same as incoherent integration, 5-time incoherent integration was applied in the simulation. By referring the measured spectral parameters at precipitation heights ($<$ 7.0 km) during 26 and 27 October 2009, V_{d} of 0.0 m s^{-1} and σ_{3dB} of 0.98 m s^{-1} were used to produce the Doppler spectrum. The results of Chapter 3 indicated that 13-point RA is optimum for NDATA of 512. Therefore, 13-point RA was used for smoothing the Doppler spectrum.

By using sufficient number of simulated cases (5000), we statistically investigate the relation between the estimation errors and ECL. Table 4.2 shows the estimation errors for cases $L = 5$ dB, 7 dB, and 10 dB, respectively. Estimation errors calculated by the bottom method were used as a reference. For each of the L cases, bias and RMS errors of P, V_{d}, and σ_{3dB} were calculated. The SNR varied from 10 dB to 30 dB with a 2 dB step. The estimated results were averaged over all the SNR cases.

TABLE 4.1: Same as Table 3.1 except that the measurement parameters are on 26 and 27 October 2009.

MU Radar	
Item	Value
F_{center}	46.5 MHz
IPP	400 μ s
NBEAM	15 (V×5, N×5, E×5)
NFREQ	5
NCOH	32
NDATA	512
Transmitted pulse	1 μs×16 (16 bit optimum Spano code)
V_{NYQ}	$\pm$8.4 m s^{-1}
ΔV_{bin}	0.03 m s^{-1}
T_{obs}	98.3 s

TABLE 4.2: Bias and RMS errors of P, V_{d}, and σ_{3dB} calculated by the top method and the bottom method, respectively. The bias and RMS errors are averaged over SNR.

	P	V_{d}	σ_{3dB}
L = 5 dB	2 $\pm$ 7%	0.00 $\pm$ 0.03 m s^{-1}	2 $\pm$ 8%
L = 7 dB	1 $\pm$ 7%	0.00 $\pm$ 0.02 m s^{-1}	2 $\pm$ 6%
L = 10 dB	1 $\pm$ 7%	0.00 $\pm$ 0.02 m s^{-1}	2 $\pm$ 4%
bottom method	0 $\pm$ 7%	0.00 $\pm$ 0.02 m s^{-1}	0 $\pm$ 3%

For all the L cases, P was slightly overestimated. However, the bias and RMS errors of P were comparable to those calculated by the bottom method ($\leq$ 2% and $\sim$7%, respectively). Similar to P, the bias and RMS errors of V_{d} calculated by the top method were also comparable to those calculated by the bottom method ($\sim$0.00 m s^{-1} and $\leq$ 0.03 m s^{-1}, respectively). When L increased from 5 dB to 10 dB, the errors of σ_{3dB} reduced from 2 $\pm$ 8% to 2 $\pm$ 4%. Though σ_{3dB} was overestimated

compared with that calculated by the bottom method, the overestimation was sufficiently small ($\leq 2\%$). These results indicate that the top method with L of 10 dB shows the best performance and that L down to 5 dB also can be used.

Because the estimation accuracy of R_{echo} determines the estimation errors of the spectral parameters, we calculated mean and RMS values of R_{echo} for L of 5 dB, 7 dB, and 10 dB, respectively (Table 4.3). The Doppler velocity range, in which the model echo intensity is greater than the ECL ($R_{\mathrm{echo\_model}}$), was listed as a reference, and the percentage ratio of R_{echo} against $R_{\mathrm{echo\_model}}$ are shown. It is noted that R_{echo} was slightly overestimated because the smoothed Doppler spectrum was used. The overestimation of R_{echo} caused the slight overestimation of P and σ_{3dB}. With the increase of L, the RMS value of R_{echo} was reduced from 6.6% to 3.3%. Correspondingly, the RMS error of σ_{3dB} was reduced from 8% to 4%.

TABLE 4.3: Bias and RMS values of R_{echo} calculated by the top method. The data elements contain two lines. The first lines show the mean and RMS values of the R_{echo}. The second lines show the percentage ratio of R_{echo} against $R_{\mathrm{echo\_model}}$.

	$R_{\mathrm{echo\_model}}$	R_{echo}
L = 5 dB	41	41.1 ± 2.7 100.2 ± 6.6%
L = 7 dB	47	48.6 ± 2.3 103.4 ± 4.9%
L = 10 dB	57	58.1 ± 1.9 101.9 ± 3.3%

4.1.1.3 Performance evaluation using measurement results

By using the measurement results of the MU radar, we compare the performance of the top method with that of the bottom method. The Doppler spectra were collected by the vertical beam during the period between 22:01 on 26 October and 02:23 JST on 27 October 2009. In order to avoid the influence of hydrometeor echoes, Doppler spectra between 6.0 km and 9.0 km height were used. L of 10 dB was used for the top method.

Figure 4.5 shows the relation between the spectral parameters calculated by the bottom method and those calculated by the top method. For P, because $f_{\mathrm{p\_loss}}$ is

as small as 3.2% (see Figure 4.3), the regression line for the case without correction ($0.999x - 0.09$), and that for the case with correction ($0.999x + 0.052$) do not show significant difference (Figures 4.5(a) and 4.5(d)). On the other hand, because f_{σ_loss} is as large as 9.3% (see Figure 4.3), the regression line for $\sigma_{3\mathrm{dB}}$ improves from $0.85x + 0.031$ to $0.975x - 0.029$ by the correction (Figure 4.5(b) and 4.5(e)). The results demonstrate that the correction is useful for improving estimation accuracy of $\sigma_{3\mathrm{dB}}$. V_d calculated by the bottom method and that calculated by the top method had good agreement as shown by the regression line ($0.998x - 0.006$; Figure 4.5(c)).

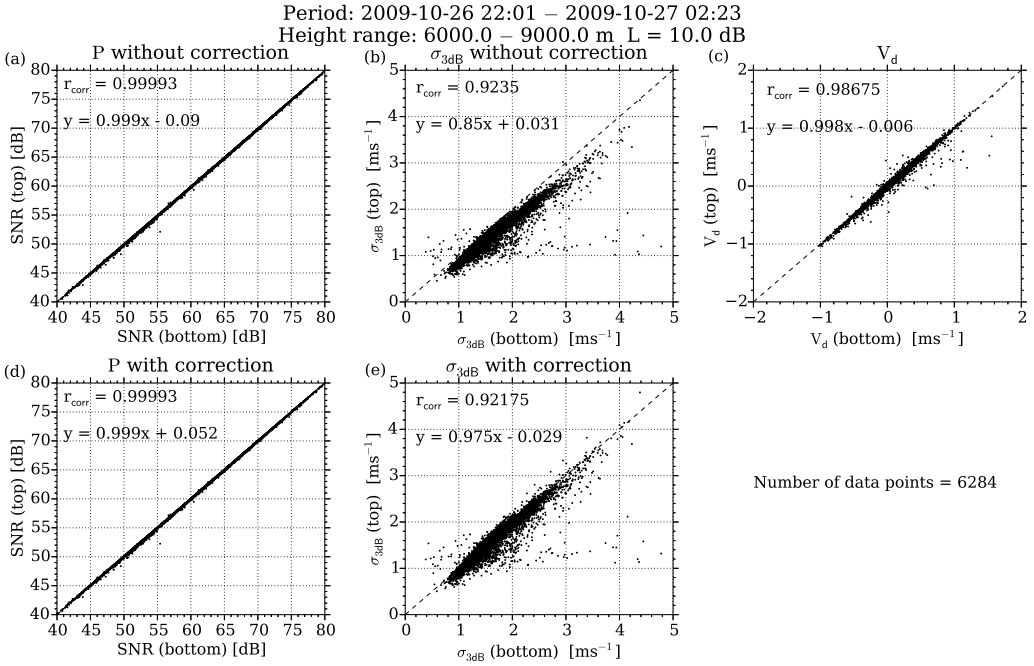

FIGURE 4.5: Scatter plots between the spectral parameters calculated by the bottom method and those calculated by the top method. Doppler spectra were collected by the vertical beam of the MU radar during a period between 22:01 on 26 October and 02:23 JST on 27 October 2009. Calculation results in a height range between 6.0 km and 9.0 km were used. Horizontal axes show the spectral parameters calculated by the bottom method. Vertical axes show the spectral parameters calculated by the top method. (a) The comparison results of P without and (b) with correction for the top method. (b) The comparison results of $\sigma_{3\mathrm{dB}}$ without and (e) with correction. (c) The comparison result of V_d.

4.1.2 Computation method using the minimum echo level (Two-echo method)

In this section, the two-echo method using the minimum echo level (MEL) is described. For aggregates and snowflakes with small fall velocity ($\sim$1–3 m s^{-1}) and large size (see section 3.2.7 of *Houze* [1993]), echo intensities and peak locations of their echoes are close to those of the clear-air echoes. Therefore, the top method, which uses constant L, cannot remove the contamination of their echoes sufficiently. In addition to the top method, we propose the two-echo method which can be used for aggregates and snowflakes. The two-echo method is also applied to melting hydrometeors.

4.1.2.1 Signal processing method

Figure 4.6 shows a flow chart of the two-echo method. In order to explain the two-echo method, an example is presented in Figure 4.7a. In Step (1), a Doppler spectrum is produced (blue dotted curve in Figure 4.7a). In Step (2a), a smoothed Doppler spectrum is produced by using the 13-point RA (black curve). In Step (2b), using the smoothed Doppler spectrum, a MEL which locates between the peak location of the clear-air echo and that of the hydrometeor echo is determined (orange dashed line in Figure 4.7(a)). The unit of MEL is dB. The conditions for determining MEL are as follows. (1) Find the peak location of a clear-air echo. An appropriate Doppler velocity range is recommended to be given for determining the peak location. (2) Doppler velocity bins which have greater values than the peak location (i.e., Doppler velocities downward from the peak location of the clear-air echo) are candidates of the MEL location. (3) Find the center of Doppler velocity bins at which all of the adjacent 30 Doppler velocity bins (15 points each in both the positive and negative directions) have the signal intensities greater than the signal intensity at the center. (4) MEL is determined as the signal intensity of the center which satisfies (2) and (3). If multiple candidates exist, the Doppler velocity bin closest to the peak location of the clear-air echo is determined as the MEL location. The value of 15 points were determined by considering that a peak location of a clear-air echo and that of hydrometeor echo are at least $\sim$1 m s^{-1} apart with each other in most of the cases. Note that because the number of adjacent points used

for determining the MEL depends on resolution of Doppler velocity bins, it needs to be changed for measurement parameters other than those listed in Table 4.1.

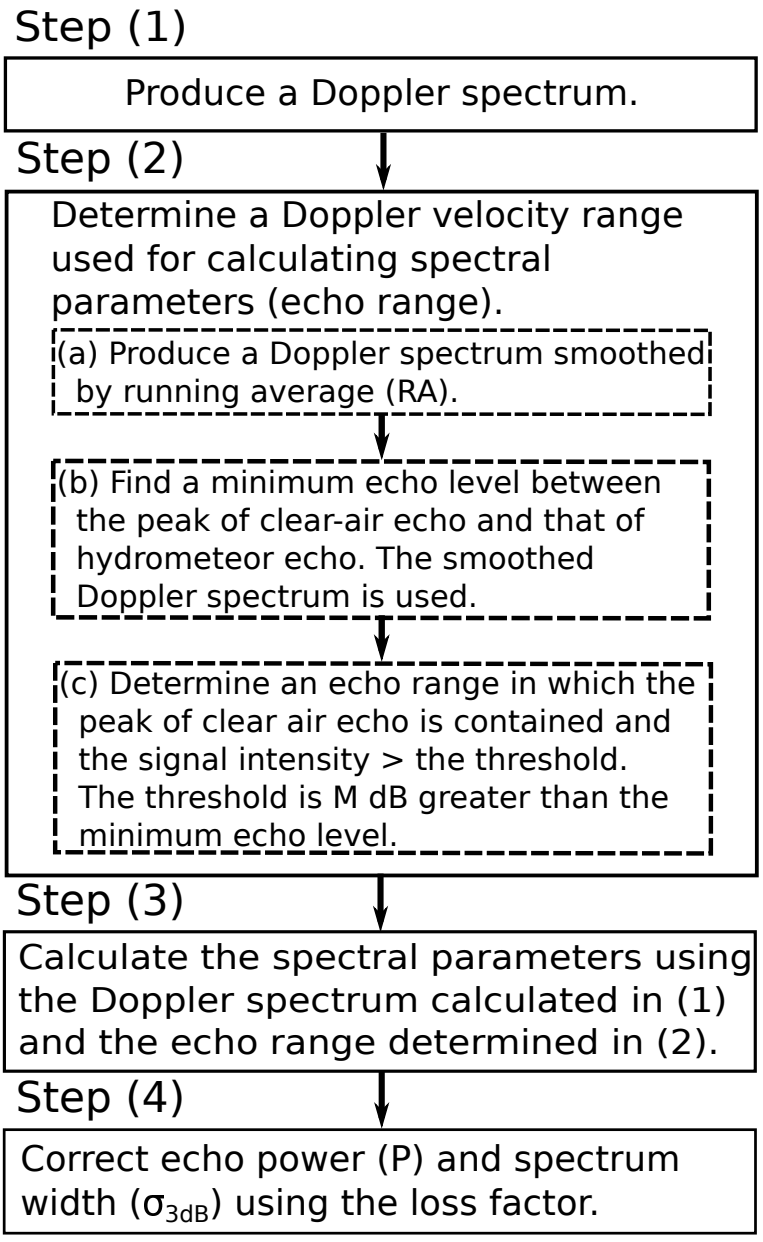

FIGURE 4.6: Same as Figure 4.1 except for the two-echo method.

In Step (2c), ECL is determined from MEL (purple line in Figure 4.7(a)). The difference between ECL and MEL is defined by M (i.e., M=ECL−MEL). By using ECL, R_{echo} is determined (green dashed line in Figure 4.7(a)). In Steps (3) and (4), the same calculations as the top method are carried out.

When the top method with L of 10 dB was used (Figure 4.7(b)), R_{echo} was as large as 102 because the large value of L causes the contamination of hydrometeor echoes. V_{d} was 0.06 m s^{-1}, and was apart from the peak location of the clear-air echo (-0.75 m s^{-1}). σ_{3dB} was as large as 2.31 m s^{-1}. By using the two-echo method with M of 1 dB, R_{echo} reduced to 29 because it contained only the clear-air echo. V_{d} and σ_{3dB} reduced to be -0.73 m s^{-1} and 0.64 m s^{-1}, respectively (Figure 4.7(a)).

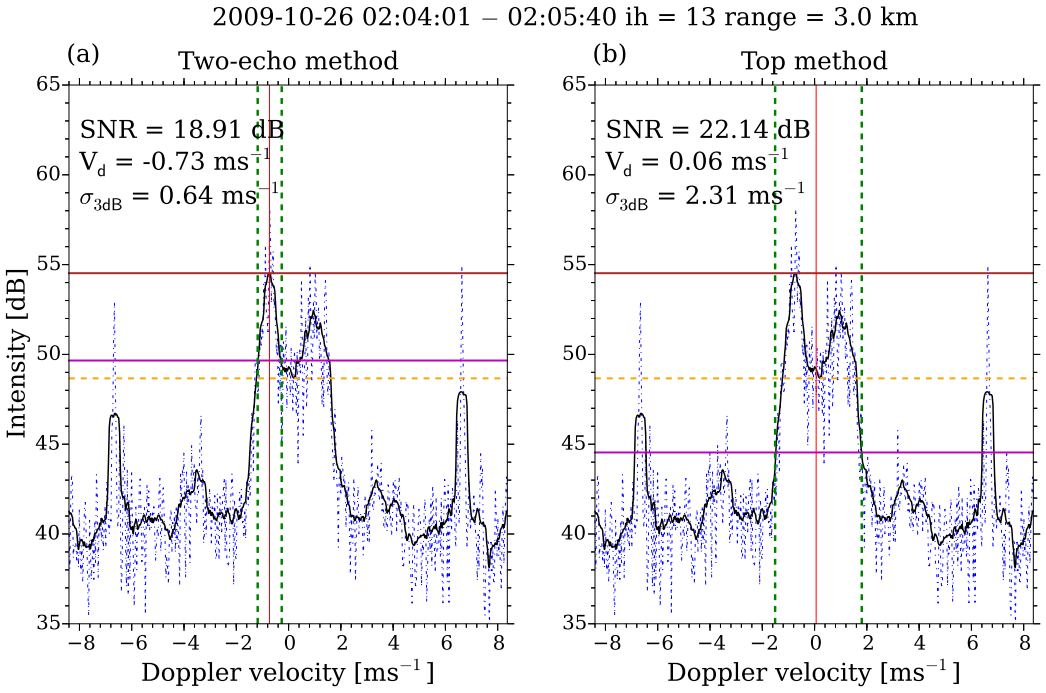

FIGURE 4.7: (a) Spectral parameters calculated by the two-echo method with M of 1 dB and (b) the top method with L of 10 dB. The Doppler spectrum was collected by the vertical beam of the MU radar during a period between 02:04:01 and 02:05:40 JST on 26 October 2009 at 3.0 km height. The curves and lines show the same as those in Figure 4.2 except that the horizontal orange dashed lines are the minimum echo level (MEL).

4.1.2.2 Performance evaluation using numerical simulation

By using numerical simulation, we investigate relation between the estimation errors of the spectral parameters and ECL. Figure 4.8 shows an example of simulated Doppler spectrum. The measurement parameters listed in Table 3.1 were used. At the melting height (from ∼2.4 km to ∼3.1 km), echo power of hydrometeor echoes (P_{h}) and Doppler velocity of hydrometeor echoes (V_{h}) were close to those of the clear-air echoes. The simulation parameters were set by referring the measurement

results of the MU radar in this height range. P_{h} was 1.0 dB smaller than P. V_{d} was -0.5 m s^{-1}, and $\sigma_{3\mathrm{dB}}$ was 0.9 m s^{-1}. V_{h} was 1.5 m s^{-1}, and the spectrum width of the hydrometeor echo ($\sigma_{3\mathrm{dB_h}}$) was 1.1 m s^{-1}. Both the clear-air and hydrometeor echoes were assumed to follow the Gaussian distribution and had perturbations following χ^2 distribution with 2 degrees of freedom. 5-times incoherent integration was used in the simulation. In order to improve determination accuracy of the peak location of a clear-air echo, the peak location was determined in the Doppler velocity range between -1.0 m s^{-1} and 1.0 m s^{-1}.

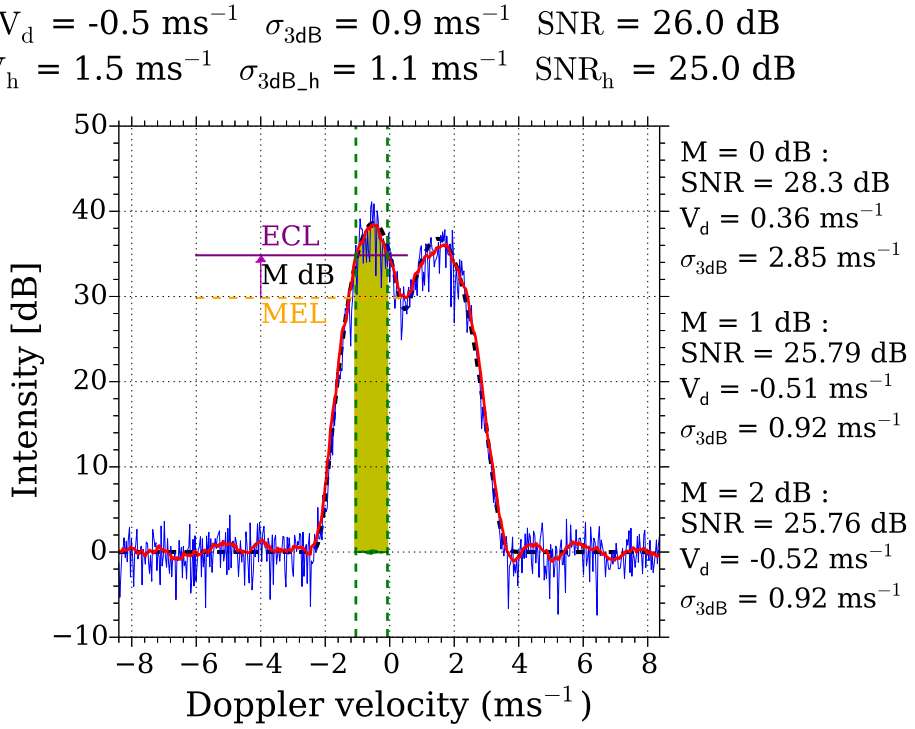

FIGURE 4.8: Example of a Doppler spectrum used for examining M in the two-echo method. The color configurations are the same as those in Figure 4.4 except that the orange dashed line is the MEL. The estimation results for $M = 0$, 1, and 2 dB are shown on the right side of the panel.

By using sufficient number of simulated cases (5000), we statistically investigate the relation between estimation errors of the spectral parameters and the value of M. Table 4.4 shows the estimation errors for cases $M = 0$ dB, 1 dB, 2 dB, and 3 dB, respectively. SNR varied from 10 dB to 30 dB with a 2 dB step. The estimated results were averaged over all the SNR cases.

TABLE 4.4: Same as Table 4.2 except that simulation results obtained by the two-echo method are shown.

M	P	V_{d}	$\sigma_{3\mathrm{dB}}$
0 dB	39 ± 40%	0.40 ± 0.43 m s^{-1}	96 ± 99%
1 dB	3 ± 7%	0.01 ± 0.02 m s^{-1}	5 ± 5%
2 dB	3 ± 7%	0.01 ± 0.02 m s^{-1}	4 ± 6%
3 dB	3 ± 7%	0.01 ± 0.02 m s^{-1}	4 ± 6%

With the increase of M, the estimation errors reduced especially for $\sigma_{3\mathrm{dB}}$. The bias and RMS error of $\sigma_{3\mathrm{dB}}$ reduced from 96 ± 99% to 5 ± 5% by increasing M from 0 dB to 1 dB. For the cases $M = 2$ dB and 3 dB, the estimation accuracy did not show significant improvement from the case $M = 1$ dB.

4.2 Application to a precipitation event

Using the measurement results obtained by the vertical beam of the MU radar during the period between 00:00 and 03:13 JST on 26 October 2009, we assess the performance of the top method and the two-echo method in precipitation region.

4.2.1 Selection of methods

Because the shape and size of hydrometeors vary with heights, the top method and the two-echo method must be used by considering height variations of their fall velocity and echo intensity. In order to explain how the top and two-echo methods are selected, height plots of the Doppler spectra, V_{d}, and $\sigma_{3\mathrm{dB}}$ are shown in Figure 4.9. The Doppler spectra were collected by the vertical beam of the MU radar during the period between 01:17:39 and 01:19:17 JST on 26 October 2009. In a height range between 1.05 km and 2.4 km, the raindrops with large fall velocity (∼5–10 m s^{-1}) existed. Therefore, the top method was used. At the heights except 2.4 km, L of 10 dB was used in order to improve the estimation accuracy. L of 7 dB was used at 2.4 km because the intensities of clear-air echoes were weak. In the height range between 1.05 km and 2.4 km, V_{d} calculated by the bottom method and

that calculated by the top method did not show significant difference. However, σ_{3dB} calculated by the bottom method was overestimated because the raindrop echoes were contaminated in the determination of R_{echo} and noise intensities below 2.4 km were greater than those above ∼5 km (Figure 4.9(a)). At the height of 2.4 km, V_d and σ_{3dB} calculated by the bottom method were as large as 1.86 m s^{-1} and 5.07 m s^{-1}, respectively (Figure 4.9(a)). By using the top method, they reduced to 0.09 m s^{-1} and 0.57 m s^{-1} (Figure 4.9(b)).

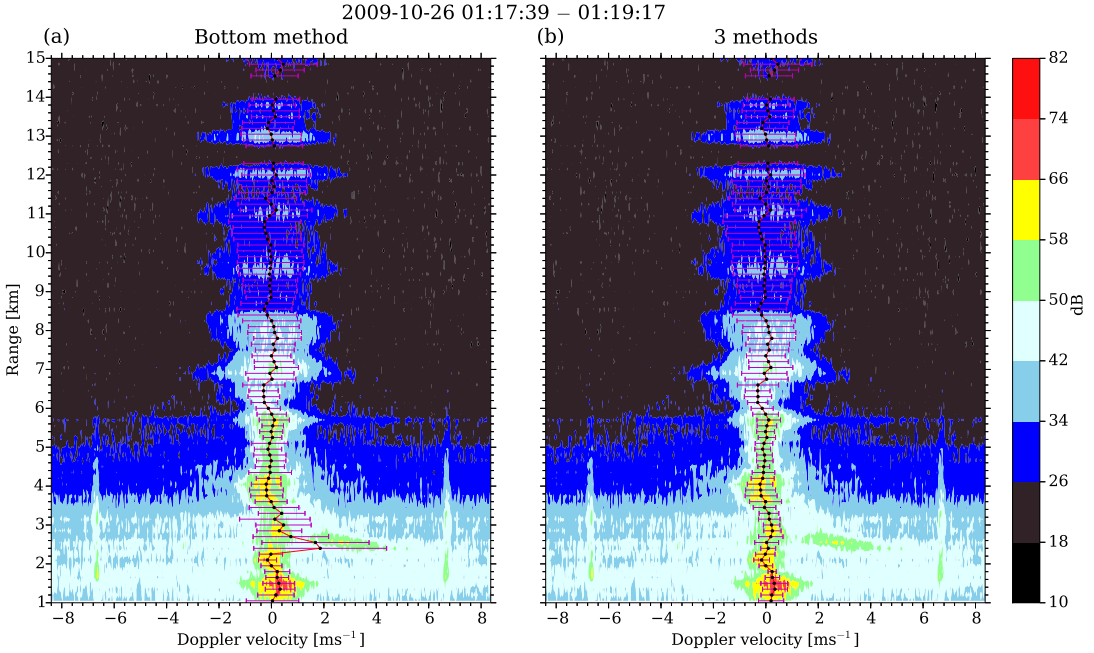

FIGURE 4.9: Examples of height profiles of Doppler spectra (colored), V_d (black dots) and σ_{3dB} (red bars) for the cases of (a) the bottom method and (b) the three methods. The Doppler spectra were collected by the vertical beam of the MU radar during the period between 01:17:39 and 01:19:17 JST on 26 October 2009.

Radiosonde results on 25 October, 2015 showed that 0° C height was ∼3.1 km (figure not shown), and the melting height located between ∼2.4 km and ∼3.1 km (later shown in Figure 4.14). Therefore, in a height range between 2.55 km and 3.9 km, melting hydrometeors, aggregates, or snowflakes with small fall velocity (∼1–3 m s^{-1}) and large echo intensities (close to the echo intensities of clear air) existed. The two-echo method was used in the height range. In a height range between 2.55 km and 2.85 km, M of 2 dB was used because perturbations of Doppler spectra near the location of MEL were greater than those at other heights. The large perturbations

were probably caused by melting hydrometeors with a variety of fall velocities. M of 1 dB was used at other heights. For the results calculated by the bottom method, a downward mis-estimation of V_{d} and overestimation of $\sigma_{3\mathrm{dB}}$ occurred because of the contamination of hydrometeor echoes (Figure 4.9(a)). Especially at the height of 2.55 km, V_{d} and $\sigma_{3\mathrm{dB}}$ were as large as 1.68 m s^{-1} and 4.09 m s^{-1}, respectively (Figure 4.9(a)). However, by using the two-echo method, V_{d} and $\sigma_{3\mathrm{dB}}$ reduced to 0.03 m s^{-1} and 0.91 m s^{-1}, respectively (Figure 4.9(b)).

In a height range between 4.05 km and 6.9 km, solid hydrometeors have small echo intensities (10 dB or more smaller than the those of the clear air). Therefore, the top method with L of 10 dB was used for reducing the estimation errors of the spectral parameters. At the height of 4.35 km, because of the contamination of the hydrometeor echo, $\sigma_{3\mathrm{dB}}$ calculated by the bottom method was as large as 1.63 m s^{-1} (Figure 4.9(a)). However, by using the top method, $\sigma_{3\mathrm{dB}}$ reduced to 0.86 m s^{-1} (Figure 4.9(b)). For a height range above 6.9 km, the bottom method was used because significant hydrometeor echoes were not observed.

The Doppler velocity range used for determining the location of EPL was between -1.0 m s^{-1} and 1.0 m s^{-1} in the height range between 2.4 km and 2.85 km. It was between -2.0 m s^{-1} and 2.0 m s^{-1} at other heights. Melting hydrometeors in the height range between 2.4 km and 2.85 km have a considerable variety of fall velocity, and their echo intensities were comparable to those of clear air. The smaller Doppler velocity range used in the height range between 2.4 km and 2.85 km was useful for reducing estimation errors of the spectral parameters.

4.2.2 Assessment using the measurement results

In order to assess the performance of the top method and the two-echo method, the spectral parameters were produced by three calculation ways: (1) As a reference, the spectral parameters were calculated by the bottom method for all the heights. (2) The spectral parameters were calculated by selecting the methods as described in section 4.2.1. Manual corrections for the spectral parameter estimations were not carried out (i.e., automatic processing; hereafter AP). (3) Same as (2) except that manual corrections were carried out (hereafter MC). For MC, L and M were

manually changed when AP could not remove the contamination of hydrometeor echoes sufficiently. For all of the three methods, in order to reduce the time interval of data collection, the spectral parameters were estimated with 49.1-s intervals ($= T_{\mathrm{obs}}/2$) by overlapping 256 time series points (= NDATA/2) in the calculation of each Doppler spectrum. Reducing the time interval was useful for comparing the measurement results of hydrometeors obtained by the LQ-7 (later explained in Figure 4.14). Figures 4.10, 4.11, and 4.12 show time-height plots of P, W, and $\sigma_{3\mathrm{dB}}$ calculated by the bottom method, AP, and MC, respectively. Because the bottom method cannot remove the contamination of hydrometeor echoes sufficiently, W was downward mis-estimated and $\sigma_{3\mathrm{dB}}$ was overestimated. Especially at a height range around the melting level (2.4 km – 3.1 km), the mis-estimation and overestimation are as large as -3.48 m s^{-1} and 6.76 m s^{-1}, respectively.

Because the top method and two-echo method can separate the clear-air echo from the hydrometeor echo with improved accuracy, the downward mis-estimation of W and overestimation of $\sigma_{3\mathrm{dB}}$ reduced much. However, for some severe cases (i.e., around 00:40 at the melting level), AP cannot determine R_{echo} correctly. Therefore, MC should be carried out for improving the estimation accuracy.

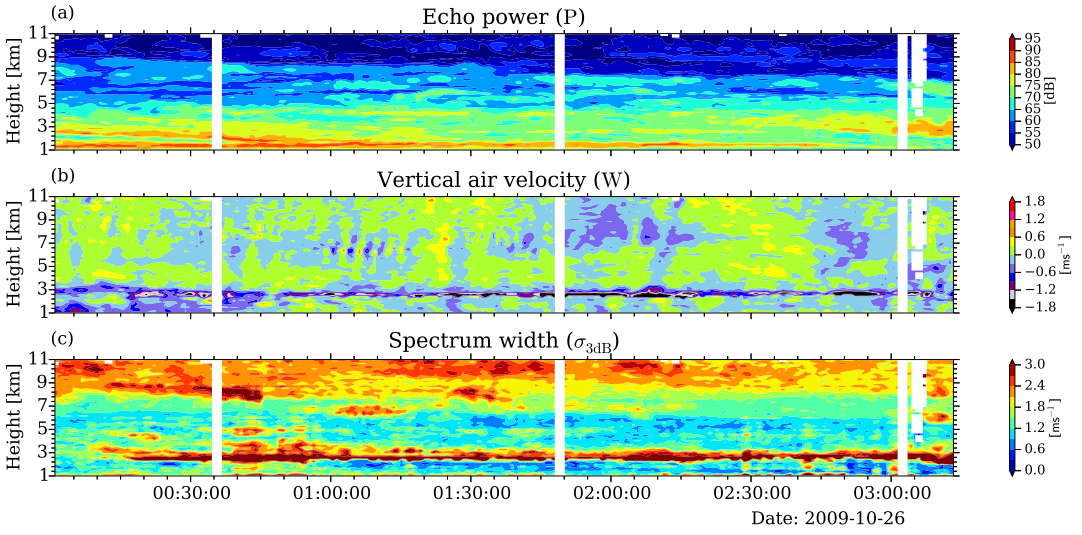

FIGURE 4.10: (a) Time-height plots of P, (b) W, and (c) $\sigma_{3\mathrm{dB}}$ collected by the vertical beam of the MU radar and produced by the bottom method during a period between 00:00 and 03:13 JST on 26 October 2009. Positive value of W indicates upward velocity.

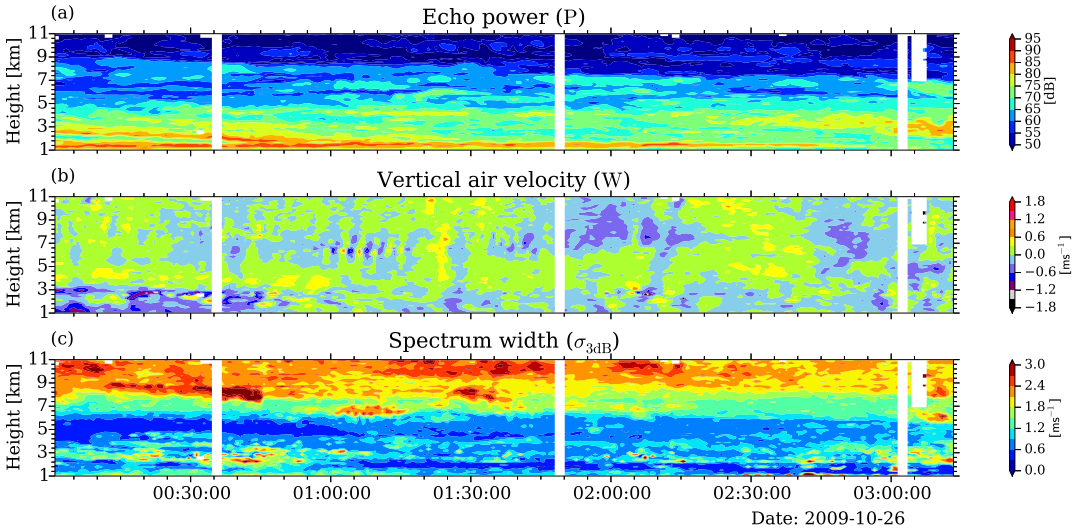

FIGURE 4.11: Same as Figure 4.10 except that AP was used to process data.

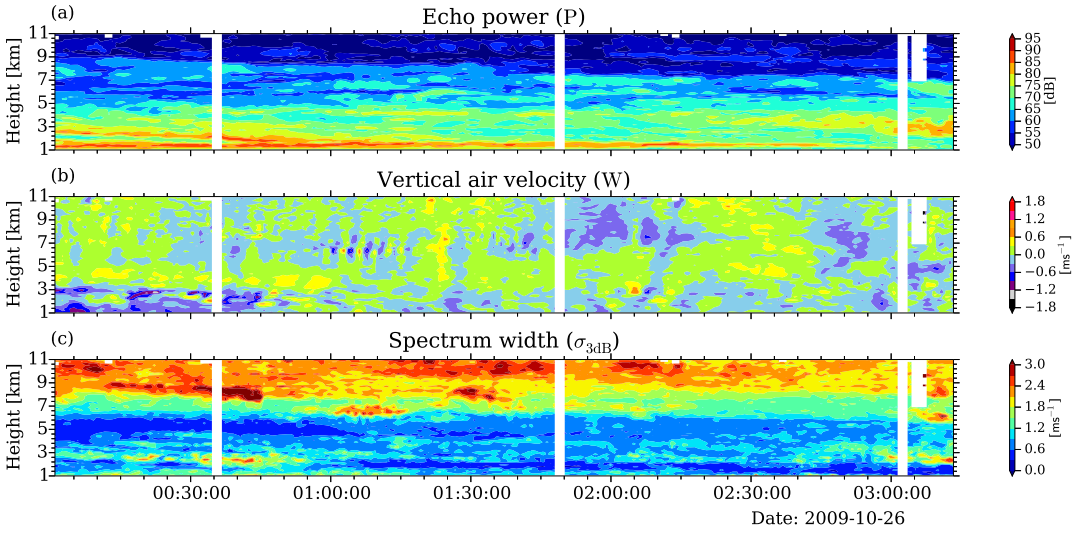

FIGURE 4.12: Same as Figure 4.10 except that MC was used to process data.

In order to evaluate the estimation errors in more detail, we calculated height profiles of mean and RMS values of the spectral parameters. The estimation results of P are shown in Figure 4.13(a). The estimation results above 7.0 km were not shown because only the bottom method was used for all the calculation cases. In the height range between ∼2.4 km and ∼3.8 km, because the bottom method could not separate clear-air echoes from hydrometeor echoes well, P calculated by the

bottom method was overestimated compared with that calculated by MC. The overestimation was as large as 3.8 dB (=76.6−72.8 dB) at 2.7 km height. On the other hand, P calculated using AP and MC did not show significant difference.

Figure 4.13(b) shows the estimation results of W. In the height range between ∼2.4 km to ∼4.0 km, W calculated by the bottom method showed a significant downward mis-estimation. The mean value of W calculated by the bottom method reached to be -1.20 m s^{-1} at 2.55 km height. By using MC, the mean value of W reduced to -0.09 m s^{-1}. W calculated by AP showed a slight downward mis-estimation compared with that by MC. The mis-estimation had the maximum of -0.04 m s^{-1} ($= -0.19 - (-0.15)$ m s^{-1}) at 2.7 km.

Figure 4.13(c) shows the estimation results of $\sigma_{3\mathrm{dB}}$. Compared with $\sigma_{3\mathrm{dB}}$ calculated by MC, $\sigma_{3\mathrm{dB}}$ calculated by the bottom method were significantly overestimated. Especially in a height range between ∼2.4 km and ∼4.0 km, the maximum difference between $\sigma_{3\mathrm{dB}}$ calculated by the bottom method and that calculated by MC was 2.55 m s^{-1} (=3.76−1.21 m s^{-1}) at 2.55 km height. The mean error of $\sigma_{3\mathrm{dB}}$ calculated by AP was greater than that calculated by MC, though its values were much smaller than those calculated by the bottom method. The differences between them were 0.22 m s^{-1} (=1.28−1.06 m s^{-1} at 2.25 km) or less. Data quality check in MC showed that the overestimation was caused by the contamination of hydrometeor echoes. The effects of contamination of hydrometeor echoes were more significant for $\sigma_{3\mathrm{dB}}$ than those for W (see Figure 4.13(b)). The results indicate that careful quality control is necessary especially in production of $\sigma_{3\mathrm{dB}}$.

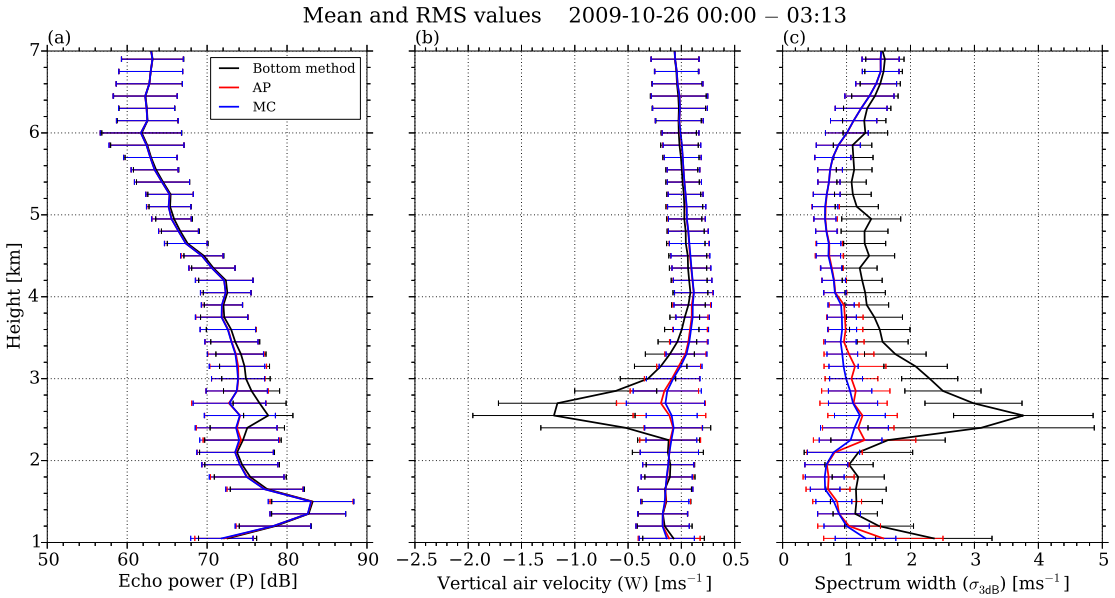

FIGURE 4.13: (a)–(c) Height plots of mean (curves) and RMS values (error bars) of P, W, and σ_{3dB} during the period between 00:00 and 03:13. The black, red, and blue curves show the results calculated by the bottom method, AP, and MC, respectively.

Figure 4.14 shows time-height plots of radar reflectivity factor (Z_e), Doppler velocity of hydrometeors relative to the ground (V_{air+Z}), W, and Doppler velocity of hydrometeors relative to the air (hereafter V_Z), respectively. V_Z was retrieved by subtracting W from V_{air+Z} (e.g., *Luce et al.* [2010]; *Yamamoto et al.* [2008]). Z_e and V_{air+Z} were measured by the LQ-7. Compared with the MU radar, the LQ-7 has higher sensitive for hydrometeor echoes owing to its shorter radar wavelength of ∼22 cm. Time and height intervals of the LQ-7 data collection were ∼18.4 s and 150 m, respectively. In order to compare the results of the MU radar with those of the LQ-7 with reduced uncertainty, data were averaged over 110 seconds in time and 300 m in height. By removing the influences of W, V_Z became more continuous both in time and height. The continuity was clearly seen at the heights above 3.0 km because V_{air+Z} of solid hydrometeors are smaller than that of raindrops (see Figures 4.14(b) and 4.14(d)).

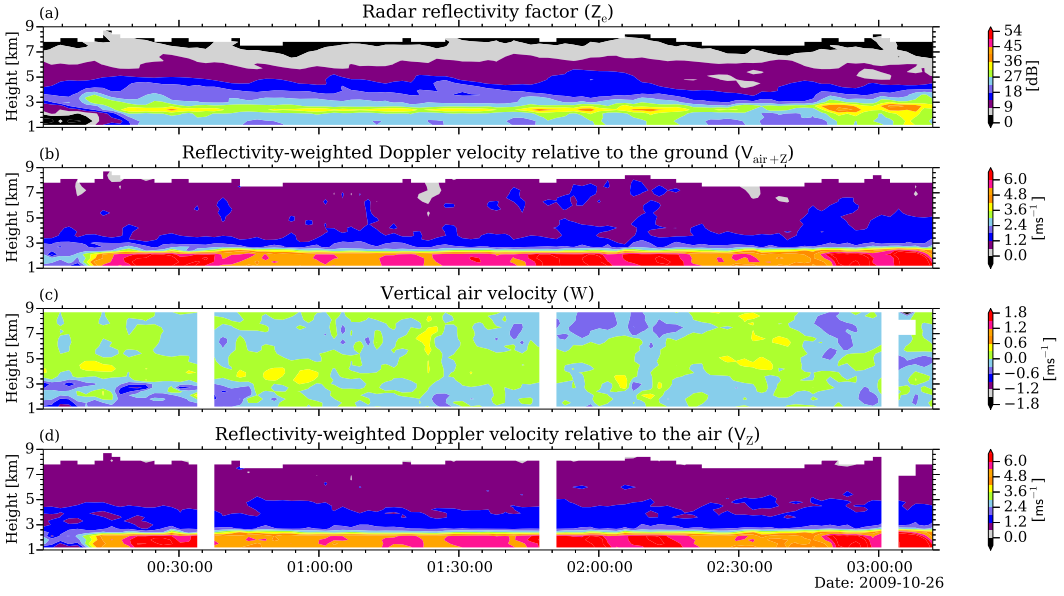

FIGURE 4.14: (a)–(d) Time-height plots of radar reflectivity factor (Z_e), Doppler velocity of the hydrometeor relative to the ground (V_{air+Z}), W, and Doppler velocity of the hydrometeor relative to the air (V_Z) during the period between 00:00 and 03:13. Z_e and V_{air+Z} were collected by the LQ-7. W was collected by the MU radar. V_Z was retrieved from V_{air+Z} and W.

In order to evaluate the measurement accuracy of W, scatter plots between Z_e and V_{air+Z} and that between Z_e and V_Z are shown in Figure 4.15. The spectral parameters were measured during a period between 00:00 and 03:13 JST on 26 October 2009. A height range between 3.125 km and 4.625 km, in which the top method or two-echo method was applied, was used for producing Figure 4.15. Because the effects of W were removed in V_Z, the correlation coefficient between Z_e and V_Z (0.57) was greater than that between Z_e and V_{air+Z} (0.38). The results indicate that W calculated by the top and two-echo methods is useful for retrieving V_Z in precipitation regions.

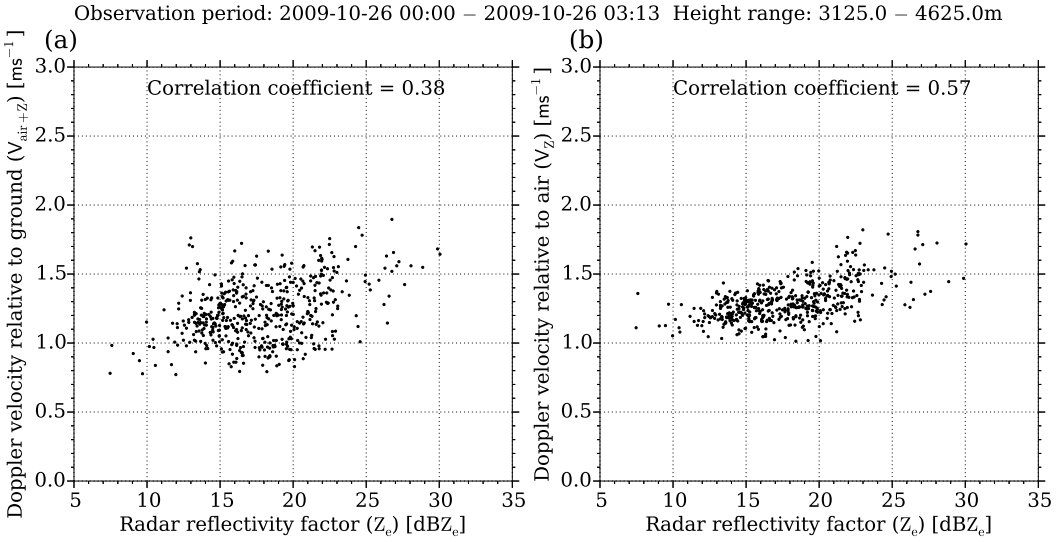

FIGURE 4.15: (a) Scatter plots between Z_e and V_{air+Z} and (b) Z_e and V_Z during the period between 00:00 and 03:13 and in the height range between 3.125 km and 4.625 km.

4.2.3 Manual correction cases

Figure 4.16 shows a height profile of the manual correction rate for the MC case. The correction rate was less than 2.2% at the heights above 4.0 km. The results indicate that the top method is effective especially for solid hydrometeors with small echo intensity. In the height range where solid hydrometeor with large echo intensity or melting hydrometeors existed (i.e., between 2.25 km and 3.9 km), the manual correction rate was greater than 9.1% and had the maximum of 23.4% at 2.25 km. Around the melting layer, the hydrometeors echoes have large intensity and small fall velocity. Therefore, the clear-air echoes and hydrometeor echoes cannot be separated clearly with each other which can be considered as the most severe conditions. The manual correction rate was as large as 23.4%. The manual correction contains the following two steps. First, select the top method or the two-echo method by referencing the observed Doppler spectrum. Second, change the value of L (for the use of the top method) or the value of M (for the use of the two-echo method). Further, in average, the difference between the spectral parameters calculated by MC and those calculated by AP don't show significantly difference. It is stressed that the use of AP contributes to reduce time for quality check even at the melting heights.

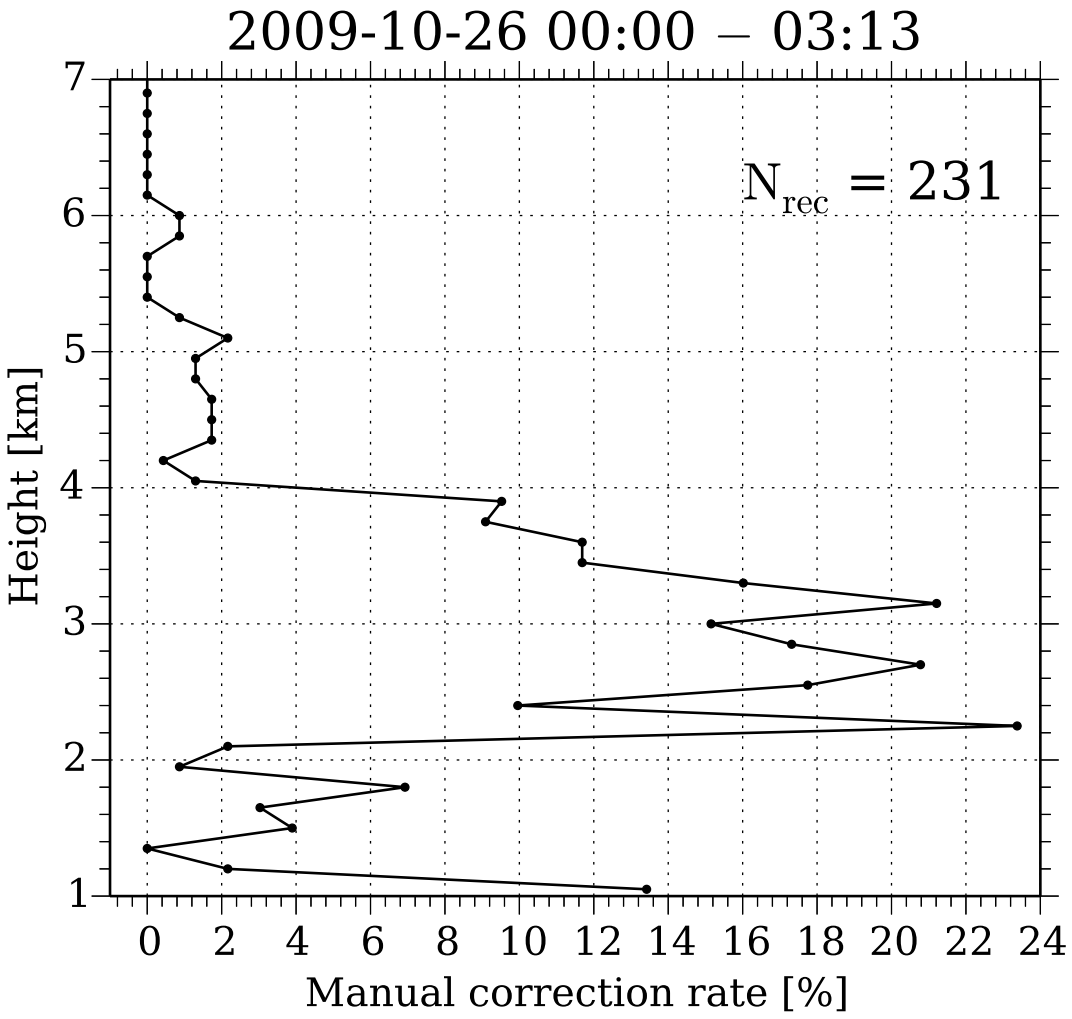

FIGURE 4.16: Height profile of the manual correction rate for the MC case shown in Figure 4.13. N_{rec} is the number of records used for calculating the height profile.

MC needs to be carried out for the following three cases: miss-detection of peak location, underestimation of the spectral parameters, and overestimation of the spectral parameters. Figure 4.17 shows the height profiles of Doppler spectra, V_{d} and σ_{3dB} processed by AP and MC, respectively. By AP, V_{d} indicated a strong downward motion (0.28 m s^{-1}), σ_{3dB} was as large as 2.67 m s^{-1} at 2.85 km. By MC, V_{d} and σ_{3dB} became more smooth in height and changed to -0.91 m s^{-1} and 1.38 m s^{-1}, respectively.

Figure 4.18 shows the Doppler spectrum at 2.85 km. Because the intensity of hydrometeor echo is much higher than that of the clear-air echo, the peak location could not be determined correctly. Therefore, the determined R_{echo} contained both clear-air echo and hydrometeor echo, and was as large as 158 (Figure 4.18(a)). By limiting the peak search range manually (-1 m s^{-1} – 0 m s^{-1}), R_{echo} contained only the clear-air echo and reduced to 32 (Figure 4.18(b)).

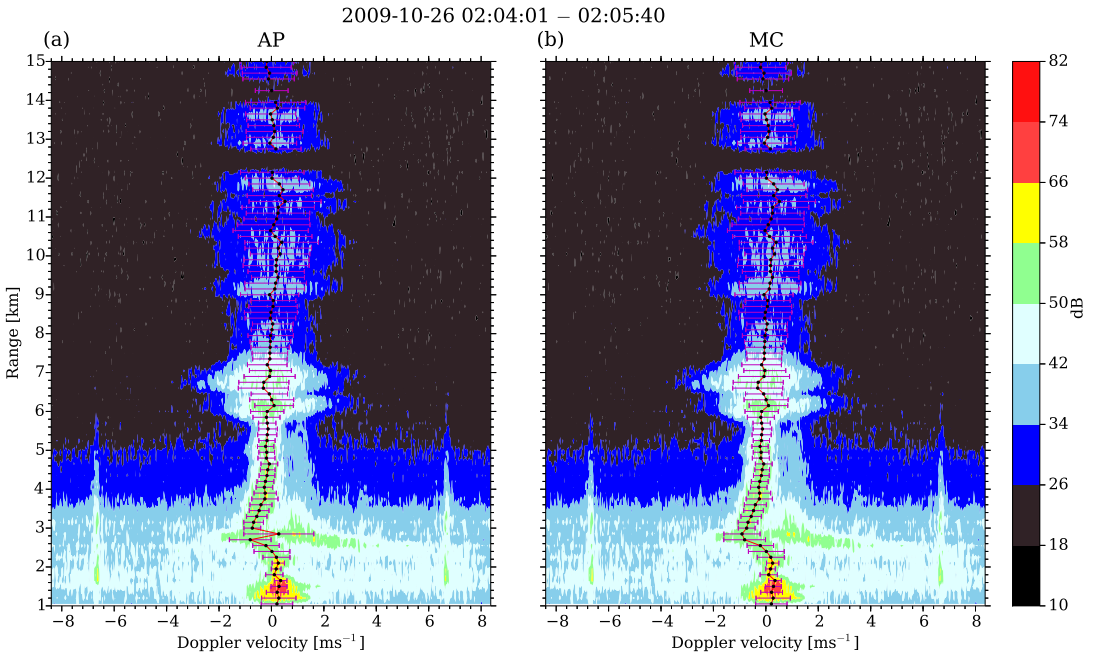

FIGURE 4.17: Examples of height profiles of Doppler spectra (colored), V_{d} (black dots) and $\sigma_{3\mathrm{dB}}$ (red bars). The Doppler spectra were collected by the MU radar during a period between 02:04:01 and 02:05:40 JST on 26 October 2009. The panels (a) and (b) show the results calculated by AP and MC, respectively.

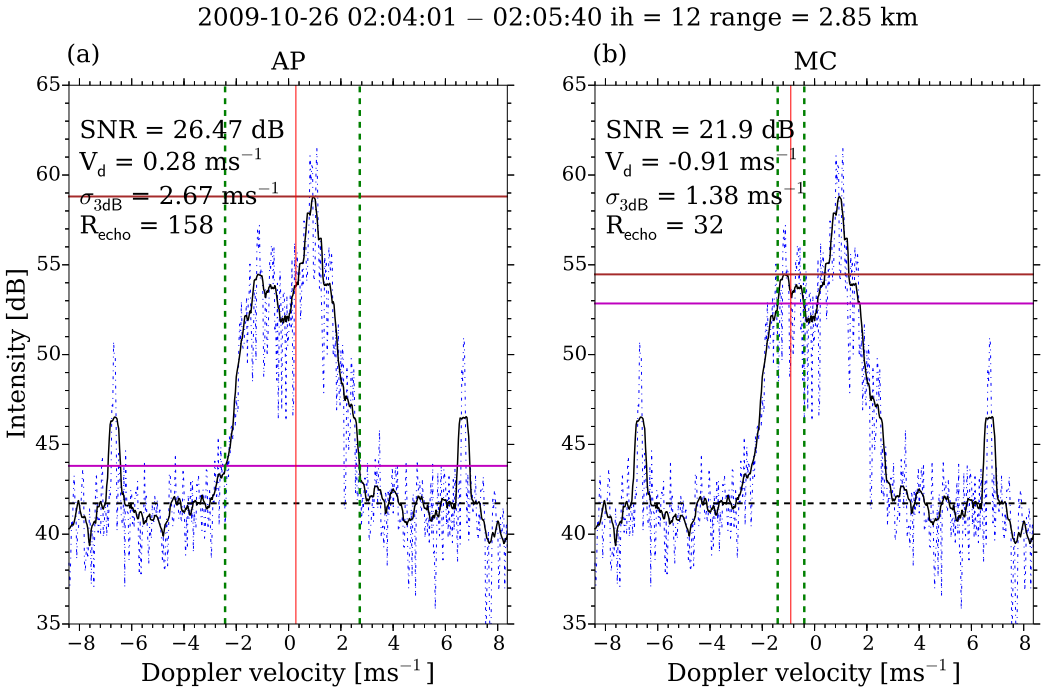

FIGURE 4.18: Spectral parameters calculated by (a) AP and (b) MC. The Doppler spectrum was collected by the MU radar during a period between 02:04:01 and 02:05:40 JST on 26 October 2009 at 2.85 km height.

Figure 4.19 shows the height profiles of Doppler spectra, V_{d} and $\sigma_{3\mathrm{dB}}$ that the spectral parameters were underestimated by AP. By AP, $\sigma_{3\mathrm{dB}}$ at 2.85 km (0.57 m s^{-1}) was smaller than that at conjunctive heights ($\sigma_{3\mathrm{dB}}$ = 1.72 m s^{-1} at 2.7 km). By MC, $\sigma_{3\mathrm{dB}}$ increased to 1.65 m s^{-1} and became continuous in height.

Figure 4.20 shows the Doppler spectrum at 2.85 km. Because the intensity and location of the hydrometeor echo were close to those of the clear-air echo, MEL was close to the peak of the clear air by using M of 2 dB. Therefore, R_{echo} was as small as 15. By using smaller M (0.5 dB), R_{echo} increased to 47. Further, SNR and $\sigma_{3\mathrm{dB}}$ increased to 32.22 dB and 1.65 m s^{-1}, respectively.

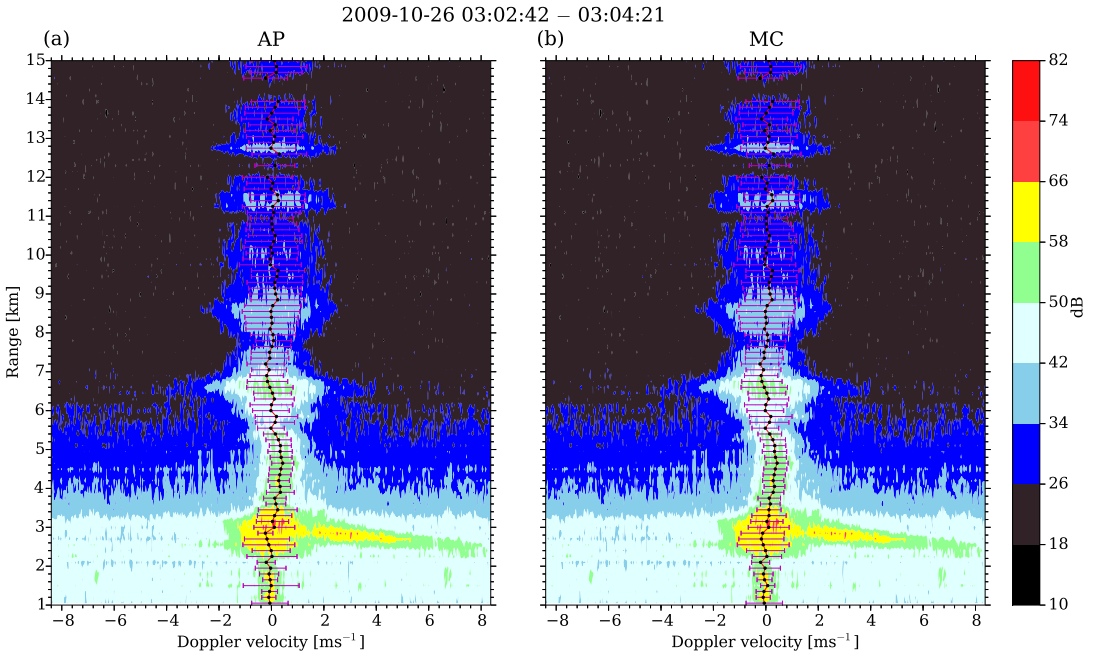

FIGURE 4.19: Same as Figure 4.17 except the Doppler spectra were collected during a period between 03:02:42 and 03:04:21.

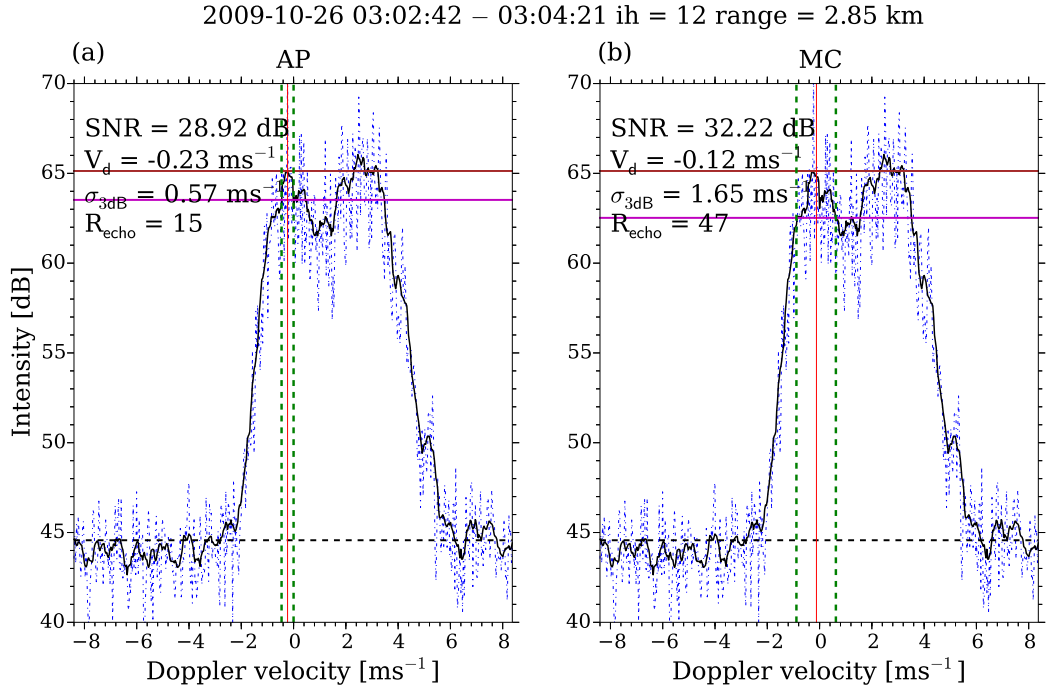

FIGURE 4.20: Same as Figure 4.18 except the Doppler spectrum was collected during a period between 03:02:42 and 03:04:21.

Figure 4.21 shows the height profiles of Doppler spectra, V_d and σ_{3dB} that σ_{3dB} was

overestimated by AP. By AP, V_{d} indicated downward motion (0.3 m s^{-1}), σ_{3dB} was as large as 2.39 m s^{-1} at 2.85 km. By MC, V_{d} and σ_{3dB} became more smooth in height and changed to -0.04 m s^{-1} and 0.89 m s^{-1}, respectively.

Figure 4.22 shows the Doppler spectrum at 2.85 km. The echo intensity of hydrometeor was smaller than that of clear air, and the peak location of the hydrometeor echo was close to that of the clear-air echo. Therefore, MEL could not be determined correctly. By using the top method with L of 7 dB, R_{echo} decreased from 168 to 44 and contained only the significant parts of the clear-air echo.

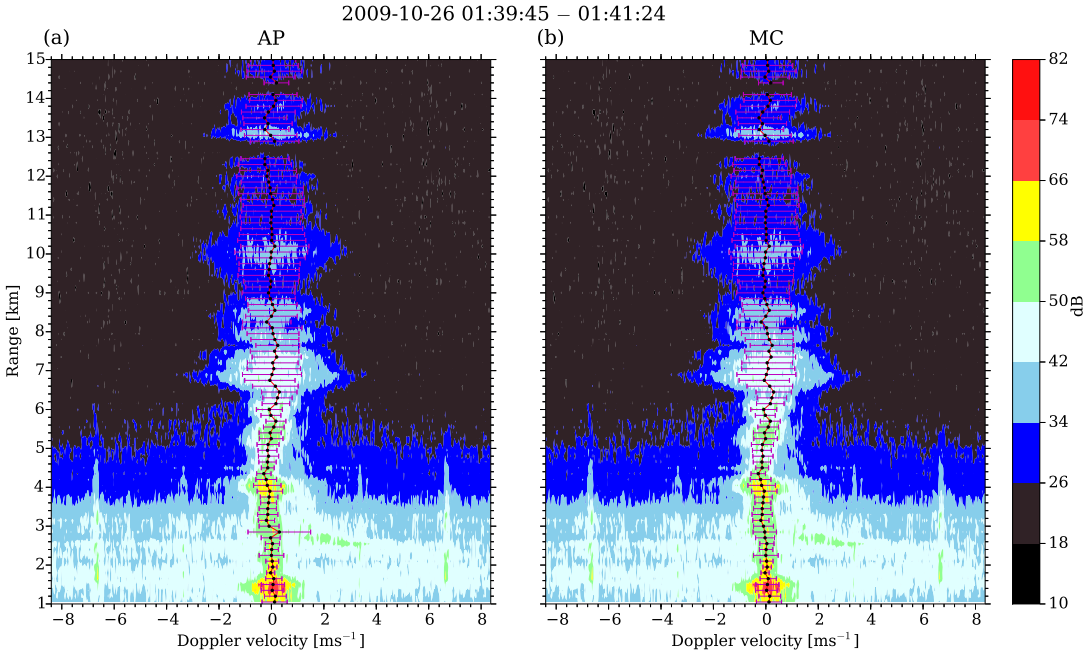

FIGURE 4.21: Same as Figure 4.17 except the Doppler spectra were collected during a period between 01:39:45 and 01:41:24.

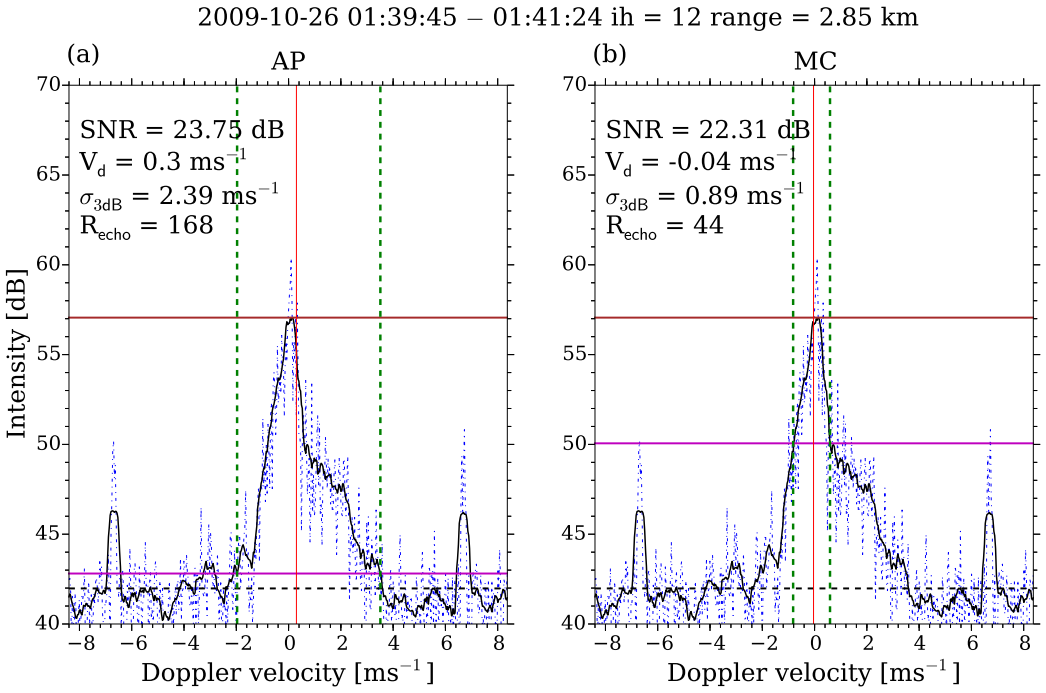

FIGURE 4.22: Same as Figure 4.18 except the Doppler spectrum was collected during a period between 01:39:45 and 01:41:24.

4.3 Methods evaluation

As described in Section 2.1.3, the least squares fitting method is widely used for calculating the spectral parameters in precipitation region. In order to evaluate the performance of the top and two-echo methods, spectral parameters calculated using the method proposed by *Shibagaki et al.* [1997] (hereafter, rain-fitting method) are shown. The rain-fitting method determines initial values automatically. Then the initial values and the least squares fitting method are used to calculating the spectral parameters. In order to match the configuration of the rain-fitting method, the Doppler spectrum points were not overlapped as described in Section 4.2.2. Figure 4.23 shows averaged spectral parameters during the period between 23:59 on 25 and 03:03 JST on 26 October 2009. The blue and red curves indicate the averaged spectral parameters calculated by using the bottom, top and two-echo methods and the rain-fitting method, respectively. The bottom, top, and two-echo methods were used in the same height range as described in Section 4.2.1. It is noted that the spectral parameters were calculated automatically. Because the parameters setting

of the rain-fitting method was not optimum for the parameters listed in Table 4.1, we only compared the results below 9 km where the echo intensity of clear air is sufficient high. Compared with the rain-fitting method, the top and two-echo methods have better performance, especially around the melting level. However, it is noted that the spectral parameters calculated by the rain-fitting method are more accurate than those calculated by the bottom method. Hereafter, we introduce three cases to compare the performance of the rain-fitting method and that of the top and two-echo methods. Figure 4.24 shows the height profiles of Doppler spectra, V_{d} and $\sigma_{3\mathrm{dB}}$ processed by the rain-fitting method and the top and two-echo methods, respectively. By using the rain-fitting method, V_{d} indicated a strong downward motion (1.79 m s^{-1} at 2.55 km), $\sigma_{3\mathrm{dB}}$ was as large as 3.6 m s^{-1} at 2.55 km. By using the two-echo method, these values changed to -0.01 m s^{-1} and 0.77 m s^{-1}, respectively.

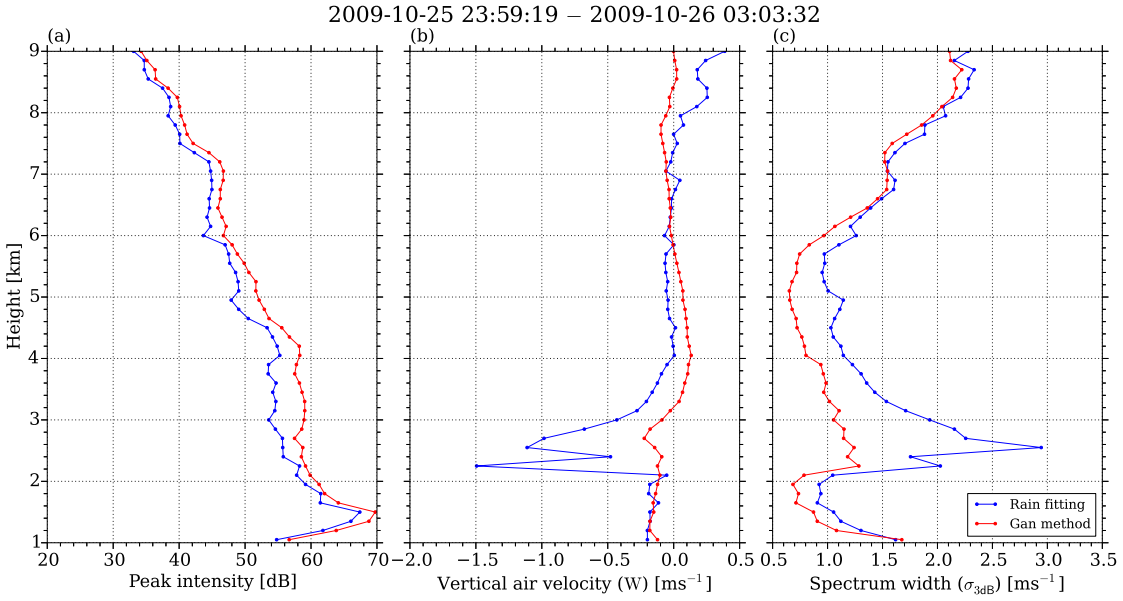

FIGURE 4.23: (a) – (c) Height plot of mean values of peak intensity, W, and $\sigma_{3\mathrm{dB}}$ during the period between 23:59 on 25 and 03:03 JST on 26 October 2009, respectively. The red curves show the results calculated by the top and two-echo methods. The top and two-echo methods were used in the same height range as described in Section 4.2.1. The blue curves show the results calculated by the rain-fitting method.

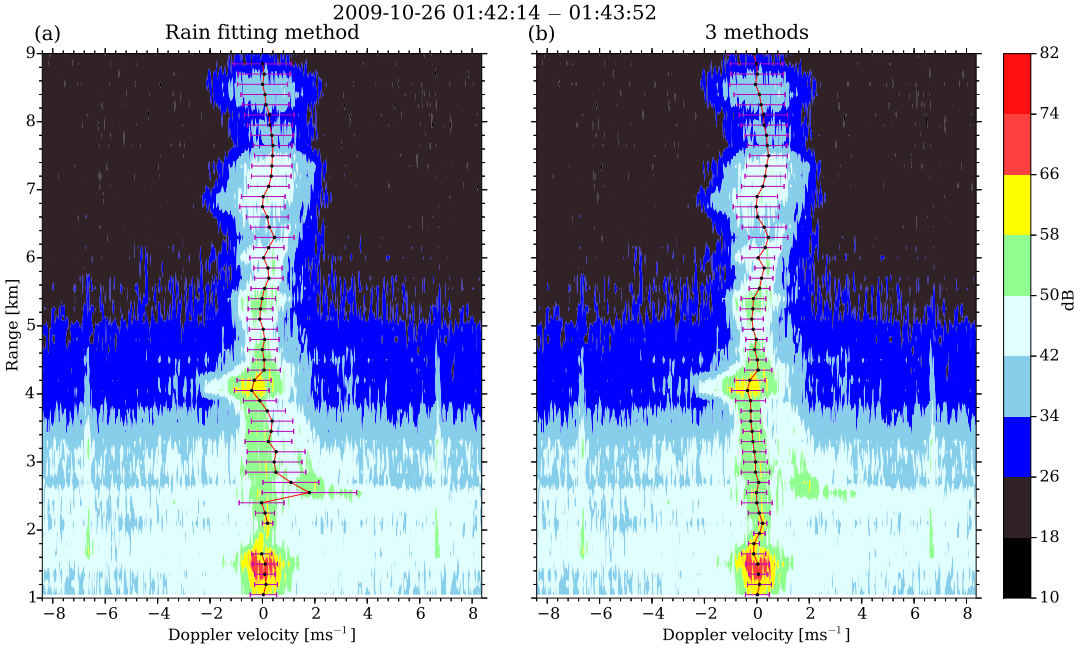

FIGURE 4.24: Examples of height profiles of Doppler spectra (colored), V_{d} (black dots) and $\sigma_{3\mathrm{dB}}$ (red bars). The Doppler spectra were collected by the MU radar during a period between 01:42:14 and 04:43:52. The panels (a) and (b) show the results calculated by the rain-fitting method and the top and two-echo methods, respectively.

Figure 4.25 shows a case that both methods had comparable performance. However, the rain-fitting method failed at 2.4 km and 2.85 km.

Figure 4.26 shows a case that both methods were miss-calculated. At a height range between 2.55 km and 3.15 km, because the contamination of hydrometeor echoes, V_{d} indicated strong downward motion and $\sigma_{3\mathrm{dB}}$ was very large for both methods.

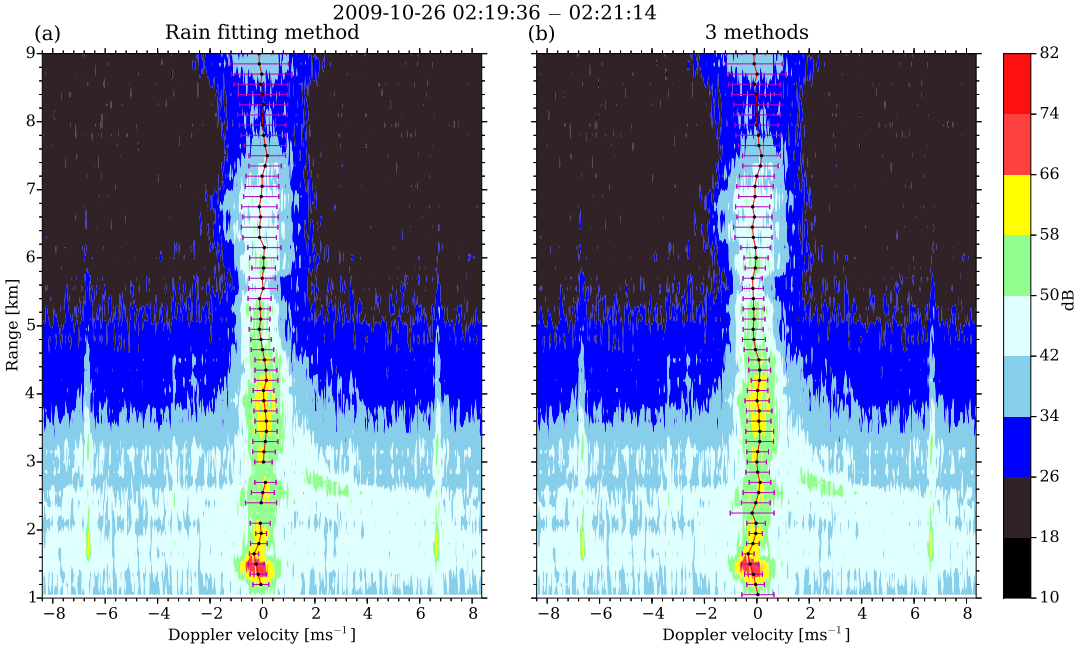

FIGURE 4.25: Same as Figure 4.24 except that the Doppler spectra were collected during a period between 02:19:36 and 02:21:14.

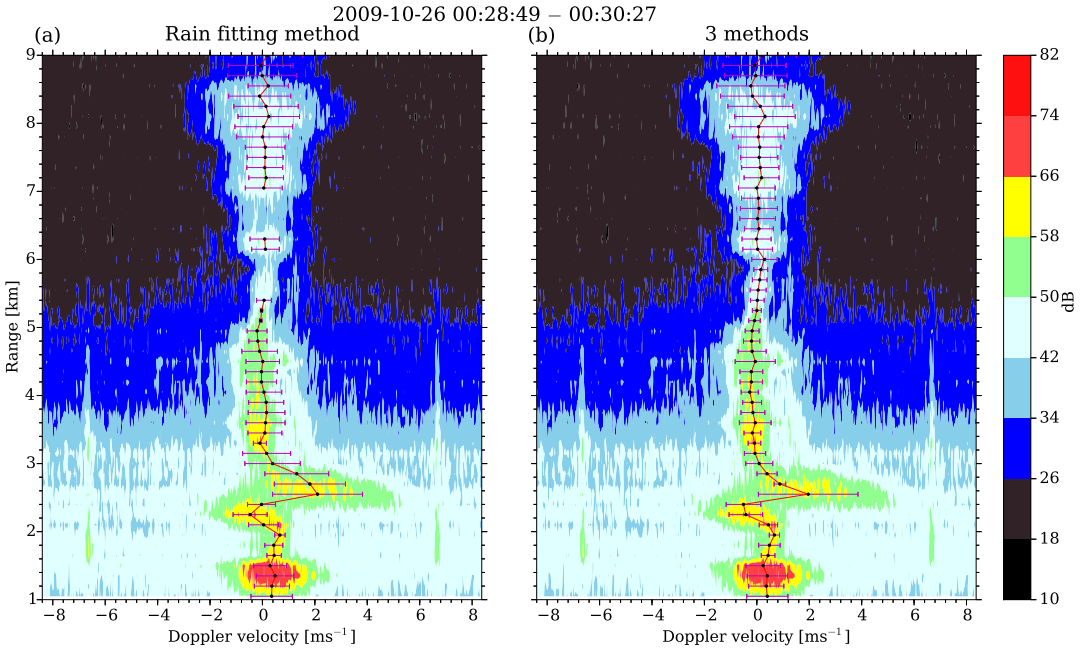

FIGURE 4.26: Same as Figure 4.24 except that the Doppler spectra were collected during a period between 00:28:49 and 00:30:27.

Further, we compared the time cost of the rain-fitting method and that of the top and two-echo methods. The rain-fitting method ran on a Solaris computer with

UNIX system. On the other hand, the top and two-echo methods ran on a computer with Linux system. Therefore, we calculated the flops number of each computer by using LINPACK test. For the Solaris computer with UNIX system, the flops number is about 67 Mflops. Processing about 3-hours MU radar data needs 2410 s. For the computer with Linux system, the flops number is about 2180 Mflops. Processing the same MU radar data needs 24 s. Therefore, the time cost of the rain-fitting method is about 3 times greater than the top and two-echo methods.

For the rain-fitting method, the control parameters are not optimum for the observation parameters on October, 2009. Therefore, the spectral parameters calculated by the rain-fitting method had larger errors at the melting layer compared with those calculated by the top and two-echo methods. However, there is large room for improving the performance of the rain-fitting method by improving the control parameters. There are some cases that both methods worked comparable with each other. Also, for the cases that the clear-air and hydrometeor echoes are close with each other, all the methods cannot calculate the spectral parameters correctly.

4.4 Summary

In this chapter, we proposed the top method and two-echo method for calculating the spectral parameters of the clear-air echo in precipitation region. The top method is used at heights where raindrop with large fall velocity ($\sim$5 – 10 m s^{-1}) or solid hydrometeors with small echo intensities exist. In the presence of aggregates and snowflakes which have smaller fall velocity ($\sim$1 – 3 m s^{-1}) than raindrops and comparable echo intensity to the echo intensity of clear air, the two-echo method is used. By using the Doppler spectra collected by the vertical beam of the MU radar during a precipitation event, the performance of top method and that of the two-echo method were evaluated. The results indicate that though the use of the top method and the two-echo method cannot remove the contamination of hydrometeor echoes completely by automatic signal processing, the time cost of the manual correction reduces much. Further, we compared the performance of the top and two-echo methods with that of the rain-fitting method. The time cost of the top and two-echo methods is smaller than that of the rain-fitting method. Because the

control parameters of the rain-fitting method are not optimum for the measurement parameters on October 2009, there is large room for improving the performance of the rain-fitting method.

Chapter 5

Conclusions

Atmospheric radars (ARs) are used to measure refractive index perturbations caused by atmospheric turbulence. In order to improve the retrieval of truculence parameters, the range resolution should be as high as possible. Hence, in this study, we developed a new digital radar receiver which has range imaging (RIM) and oversampling (OS) capabilities to improve the range resolution. Further, high-resolution ARs collected a huge amount of Doppler spectra. Therefore, methods for calculating the spectral parameters (i.e., echo power (P), Doppler velocity (V_{d}), spectrum width ($\sigma_{3\mathrm{dB}}$)) should be simple and robust. In order to ensure the correctness of the observations, numerical simulation and measurement data were used to evaluate the methods.

In Chapter 1, the concepts of atmospheric radars were introduced. The scatter mechanism, radar equation, etc. were described. Further, techniques for signal processing (i.e., coherent integration, incoherent integration, noise estimation, spectral parameters estimation) were discussed.

In Chapter 2, the observation techniques for precipitation and radar imaging techniques (e.g., coherent range imaging and range imaging) were introduced at first. Then, the development of the digital radar receiver for the 1.3-GHz AR was discussed. The digital receiver uses a general-purpose software-defined radio receiver referred to as the USRP2 and a commercial personal computer (PC). Programs developed by C++ and Python are used for data taking and signal processing,

respectively. The high-speed sampling capability of the USRP2 was used for the 10-MS s^{-1} OS capability of the digital receiver. Because only sequential data transfer from the USRP2 to the PC is available, we implemented the RIM on the PC. By using RIM and OS, the range resolution can be as small as several tens meters.

In Chapter 3, using numerical simulation, we investigated methods for calculating the spectral parameters in clear air region. The methods that we examined are comprised of two steps. Firstly, the echo range (R_{echo}), in which the Doppler spectrum point with peak intensity is contained and all the smoothed Doppler spectrum points have intensities greater than the noise intensity, is determined. For producing the smoothed Doppler spectrum, a running average with equal weight (RA) or multi-taper method (MTM) was used. Next, the spectral parameters were calculated using the Doppler spectrum points within R_{echo}. The simulation results indicate that estimation errors of the spectral parameters depend on the estimation accuracy of the echo peak location and R_{echo}. Because of the simple computation and the better estimation performance for echoes with small σ_{3dB}, the computation method using the RA (bottom method) is more suitable for estimating the spectral parameters than the computation method using the MTM.

The estimation errors of the spectral parameters for the computations using 7-point, 13-point, and 19-point RA were discussed. By increasing the number of RA points, estimation errors in low SNRs can be reduced for echoes with large σ_{3dB} because increasing the number of RA points reduces the estimation errors of the peak location and underestimation of R_{echo}. However, the computation using the 19-point RA did not show much improvement compared with the computation using the 13-point RA. Furthermore, increasing the number of RA points causes an overestimation of σ_{3dB} in low SNRs and can increase the effects of interference signals in practical use. Therefore, we concluded that the 13-point RA is the best for the measurement parameters listed in Table 3.1. Such a consideration demonstrates that the method we proposed is simple and practical for evaluating estimation errors of the spectral parameters and for determining the optimum parameters to be used for calculating the spectral parameters.

We confirmed that the detectability D calculated by using the model Doppler spectrum is related to the estimation errors of the spectral parameters. For the case

number of Doppler spectrum points (NDATA) = 512 and the 13-point RA, the estimation errors tend to be independent of the SNR for a D range of $\geq \sim 6$. Though the peak intensity of the model spectrum (p_{k}) cannot be known from a measured Doppler spectrum, we showed that the peak level of the measured Doppler spectrum (p_{est}) can be used as a substitute for p_{k} when D is 2.5 or greater. Because the estimation accuracy of echo peak location significantly deteriorates when D is less than 2.5, the value can be used as a threshold to judge whether or not the errors of the spectral parameters are significantly large. Combined use of the SNR and D is useful for evaluating the errors of the spectral parameters. The reduction of estimation errors by incoherent integration was demonstrated. It is recommended that number of incoherent integration times (N_{icoh}) is determined by considering both D and the SNR.

By using the method we proposed, data collected by RIM LQ-7 was processed. The measurement results indicated that the high time and range resolution of RIM LQ-7 are useful for observing the boundary layer.

In Chapter 4, we proposed the top method and two-echo method for calculating the spectral parameters in precipitation region. The top method is used at heights where raindrops with large fall velocity ($\sim$5–10 m s^{-1}) or solid hydrometeors with small echo intensities exist. In order to separate clear-air echoes from hydrometer echoes, the echo cut level (ECL) is determined by using the peak intensity of a clear-air echo. The echo range (R_{echo}) is determined by using ECL. Because only the Doppler spectrum points within the R_{echo} are used for calculating the spectral parameters, the top method is able to remove the contamination of hydrometeor echoes. By assuming that the clear-air echoes follow Gaussian distribution, underestimation of P and σ_{3dB} are corrected. Using the numerical simulation and the measurement results by the MU radar, it was shown that the top method is able to calculate the spectral parameters with comparable accuracy as the bottom method.

Because aggregates and snowflakes have smaller fall velocity than raindrops and echo intensity which is comparable to that of clear air, the top method cannot separate hydrometeor echoes from clear-air echoes well. The two-echo method is used in presence of aggregates and snowflakes. In the two-echo method, ECL is determined by using the minimum echo level (MEL). ECL is M dB greater than

MEL. The spectrum point with MEL locates between a spectrum point with the peak intensity of the clear-air echo and that of the hydrometeor echo. By using numerical simulation, we assessed the relation between the estimation errors of the spectral parameters and M.

In order to evaluate the performance of the top method and the two-echo method in precipitation region, the measurement results obtained by the vertical beam of the MU radar during a period between 00:00 and 03:13 Japan Standard Time (JST) on 26 October 2009 were used. The evaluation using the mean and RMS values of P, W, and $\sigma_{3\mathrm{dB}}$ shows that a use of the top and two-echo methods are able to significantly reduce errors of spectral parameters. It is stressed that though the use of the top method and the two-echo method cannot remove the contamination of hydrometeor echoes completely by automatic signal processing, the time cost of the manual correction reduces much.

By using data collected by the LQ-7, Doppler velocity of the hydrometeor relative to the ground ($V_{\mathrm{air+Z}}$) was measured. By subtracting W from $V_{\mathrm{air+Z}}$, Doppler velocity of the hydrometeor relative to the air (V_{air}) was retrieved. The correlation coefficient between radar reflectivity factor (Z_{e}) and $V_{\mathrm{air+Z}}$ and that between Z_{e} and V_{Z} were 0.38 and 0.57, respectively. The improvement of the correlation coefficient shows that W calculated by the top and two-echo methods is useful for retrieving V_{Z} in precipitation regions.

In this study, we developed signal processing methods that contribute to improve the accuracy and resolution of ARs. By using the measurement results of RIM LQ-7, we showed that the method we proposed is useful for high resolution observation of the boundary layer. Further, measurement results of MU radar indicated that the top and two-echo methods are useful for vertical wind measurement in precipitation for 50-MHz band ARs.

Bibliography

[1] Anandan, V. K., C. J. Pan, T. Rajalakshmi, and G. Ramachandra Reddy (2004), Multitaper spectral analysis of atmospheric radar signals, *Ann. Geophys.*, *22(11)*, 3995–4003, doi:10.5194/angeo-22-3995-2004.

[2] Angevine, W. M., A.B. White, and S. K. Avery (1994), Boundary-layer depth and entrainment zone characterization with a boundary-layer profiler, *Bound.-Layer Meteor.*, *68*, 375–385.

[3] Atlas, D. and C. W. Ulbrich (1977), Path- and area-integrated rainfall measurement by microwave attenuation in 1–3 cm band, *J. Appl. Meteor.*, *16*, 1322–1331.

[4] Atlas, D., R. C. Srivastava, and R. S. Sekhon (1973), Doppler radar characteristics of precipitation at vertical incidence, *Reviews of Geophysics*, *11*, 1–35.

[5] Balsley, B. B., and K. S. Gage (1980), The MST radar technique: Potential for middle atmospheric studies, *Pure and Applied Geophysics*, *118(1)*, 452–493, doi:10.1007/BF01586464.

[6] Balsley, B. B., W. L. Ecklund, D. A. Carter, A. C. Riddle, and K. S. Gage (1988), Average vertical motions in the tropical atmosphere observed by a radar wind profiler on Pohnpei (7° N latitude, 157° E longitude), *J. Atmos. Sci.*, *45*, 396–405, doi:10.1175/1520-0469(1988)045<0396:AVMITT>2.0.CO;2.

[7] Barth, M., R. Chadwick, and D. van de Kamp, (1994), Data processing algorithms used by NOAA's wind profiler demonstration network, *Ann. Geophys.*, *12(6)*, 518-–528, doi:10.1007/s00585-994-0518-1.

[8] Capon, J. (1969), High-resolution frequency-wavenumber spectrum analysis, *Proceedings of the IEEE*, *57(8)*, 1408–1418, doi:10.1109/PROC.1969.7278.

[9] Cheong, B. L., M. W. Hoffman, R. D. Palmer, S. J. Frasier, and F. J. López-Dekker (2006), Phased-array design for biological clutter rejection: Simulation and experimental validation, *J. Atmos. Oceanic Technol.*, *23(4)*, 585–598, doi:10.1175/JTECH1867.1.

[10] Chen, J. S. (2004), On the phase biases of multiple-frequency radar returns of mesosphere-stratosphere-troposphere radar, *Radio Sci.*, *39*, RS5013, doi:10.1029/2003RS002885.

[11] Chen, J. S., and M. Zecha (2009), Multiple-frequency range imaging using the OSWIN VHF radar: Phase calibration and first results, *Radio Sci.*, *44*, RS1010, doi:10.1029/2008RS003916.

[12] Chilson, P. B., T. Y. Yu, R. G. Strauch, A. Muschinski, and R. D. Palmer (2003), Implementation and validation of range imaging on a UHF radar wind profiler, *J. Atmos. Oceanic Technol.*, *20(7)*, 987–996, doi:10.1175/1520-0426(2003)20<987:IAVORI>2.0.CO;2.

[13] Chilson, P. B. (2004), The retrieval and validation of Doppler velocity estimates from range imaging, *J. Atmos. Oceanic Technol.*, *21(7)*, 1033–1043, doi:10.1175/1520-0426(2004)021<1033:TRAVOD>2.0.CO;2.

[14] Cifelli, R., and S. A. Rutledge (1994), Vertical motion structure in maritime continent mesoscale convective systems: Results from a 50-MHz profiler, *J. Atmos. Sci.*, *51*, 2631–2652, doi:10.1175/1520-0469(1994)051<2631:VMSIMC>2.0.CO;2.

[15] Cifelli, R., C. R. Williams, D. K. Rajopadhyaya, S. K. Avery, K. S. Gage, and P. T. May (2000), Drop-size distribution characteristics in tropical mesoscale convective systems, *J. Appl. Meteor.*, *39*, 760–777, doi:10.1175/1520-0450(2000)039<0760:DSDCIT>2.0.CO;2.

[16] Cohn, S. A. and W. M. Angevine (2000), Boundary layer height and entrainment zone thickness measured by lidars and wind-profiling radars, *J. Appl. Meteor.*, *39*, 1233–1247, doi:10.1175/1520-0450(2000)039<1233:BLHAEZ>2.0.CO;2.

[17] Doviak, R. J., and D. S. Zrnić (2006), *Doppler radar and weather observations, 2nd Ed*, pp. 562, Mineola: Dover.

[18] Doviak, R. J., and R. D. Palmer (2014), Polarimetric doppler weather radar, in *Encyclopedia of atmospheric science, 2nd Ed*, London: Elsevier.

[19] Ecklund, W. L., D. A. Carter, and B. B. Balsley (1988), A UHF wind profiler for the boundary layer: brief description and initial results, *J. Atmos. Oceanic Technol.*, *5*, 432–441, doi:10.1175/1520-0426(1988)005<0432:AUWPFT>2.0.CO;2.

[20] Ecklund, W. L., D. A. Carter, B. B. Balsley, P. E. Currier, J. L. Green, B. L. Weber, and K. S. Gage (1990), Field tests of a lower tropospheric wind profiler, *Radio Sci.*, *25(5)*, 899–906, doi:10.1029/RS025i005p00899.

[21] Einaudi, F., D. P. Lalas, and G. E. Perona (1978), The role of gravity waves in tropospheric processes, *Pure Appl. Geophys.*, *117*, 627–663.

[22] Endo, S., T. Shinoda, T. Hiyama, H. Uyeda, K. Nakamura, H. Tanaka, and K. Tsuboki (2008), Characteristics of vertical circulation in the convective boundary layer over the Huaihe River basin in China in the early summer of 2004, *J. Appl. Meteor. Climatol.*, *47*, 2911–2928, doi:10.1175/2008JAMC1769.1.

[23] Fritts, D. C. (1984), Shear excitation of atmospheric gravity waves, 2. Nonlinear radiation from a free shear layer, *J. Atmos. Sci.*, *41*, 524–537, doi:10.1175/1520-0469(1984)041<0524:SEOAGW>2.0.CO;2.

[24] Fritts, D. C. and G. D. Nastrom (1992), Sources of mesoscale variability of gravity waves, Part 2: Frontal, convective and jet stream excitation, *J. Atmos. Sci.*, *49*, 111–127, doi:10.1175/1520-0469(1992)049<0111:SOMVOG>2.0.CO;2.

[25] Fukao, S., T. Sato, T. Tsuda, S. K. K. Wakasugi, and T. Makihira (1985a), The MU radar with an active phased array system 1. Antenna and power amplifiers, *Radio Sci.*, *20(6)*, 1155–1168.

[26] Fukao, S., K. Wakasugi, T. Sato, S. Morimoto, T. Tsuda, I. Hirota, I. Kimura, and S. Kato (1985b), Direct measurement of air and precipitation particle motion by very high frequency Doppler radar, *Nature*, *316*, 712–714.

[27] Fukao, S., K. Wakasugi, T. Sato, T. Tsuda, I. Kimura, N. Takeuchi, M. Matsuo, and S. Kato (1985c), Simultaneous observation of precipitating atmosphere by VHF band and C/Ku band radars, *Radio Sci.*, *20*, 622–630, doi:10.1029/RS020i003p00622.

[28] Fukao, S., H. Hashiguchi, M. Yamamoto, T. Tsuda, T. Nakamura, M. K. Yamamoto, T. Sato, M. Hagio, and Y. Yabugaki (2003), Equatorial Atmosphere Radar (EAR): System description and first results, *Radio Sci.*, *38*, 1053, doi:10.1029/2002RS002767.

[29] Fukao, S. (2007), Recent advances in atmospheric radar study, *J. Meteorol. Soc. Jpn*, *85B*, 215–239, doi:10.2151/jmsj.85B.215.

[30] Furumoto, J., K. Kurimoto, and T. Tsuda (2003), Continuous observations of humidity profiles with the MU radar-RASS combined with GPS and rawinsonde measurements, *J. Atmos. Oceanic Technol.*, *20*, 23–41, doi:10.1175/1520-0426(2003)020<0023:COOHPW>2.0.CO;2.

[31] Gage, K. S., and B. B. Balsley (1978), Doppler radar probing of the clear atmosphere, *Bull. Amer. Meteor. Soc.*, *59*, 1074–1093, doi:10.1175/1520-0477(1978)059<1074:DRPOTC>2.0.CO;2.

[32] Gage, K. S., C. R. Williams, and W. L. Ecklund (1994), UHF wind profilers: A new tool for diagnosing tropical convective cloud systems, *Bull. Amer. Meteor. Soc.*, *75*, 2289–2294, doi:10.1175/1520-0477(1994)075<2289:UWPANT>2.0.CO;2.

[33] Gaffard, C., J. Nash, E. Walker, T. J. Hewison, J. Jones and E. G. Norton (2008), High time resolution boundary layer description using combined remote sensing instruments, *Annales Geophysicae*, *26(9)*, 2597–2612, doi:10.5194/angeo-26-2597-2008.

[34] Gill, A. (1982), *Atmosphere-Ocean Dynamics*, pp. 666, Academic Press, New York–Toronto.

[35] Gunn, K. L. S. and R. S. Marshall (1958), The distribution of size of aggregate snowflakes, *J. Meteor.*, *75*, 425–461, doi:10.1175/1520-0469(1958)015<0452:TDWSOA>2.0.CO;2.

[36] Hashiguchi, H., M. D. Yamanaka, T. Tsuda, M. Yamamoto, T. Nakamura, T. Adachi, S. Fukao, T. Sato, and D. L. Tobing (1995a), Diurnal variations of the planetary boundary layer observed with an L-band clear-air doppler radar, *Boundary-Layer Meteorology*, *74(4)*, 419–424.

[37] Hashiguchi, H., S. Fukao, T. Tsuda, M. D. Yamanaka, D. L. Tobing, T. Sribimawati, S. W. B. Harijono, and H. Wiryosumarto (1995b), Observations of the planetary boundary layer over equatorial Indonesia with an L band clear-air Doppler radar: Initial results, *Radio Sci.*, *30(4)*, 1043–1054.

[38] Hashiguchi, H., S. Fukao, Y. Moritani, T. Wakayama, and S. Watanabe (2004), A lower troposphere radar: 1.3-GHz active phased-array type wind profiler with RASS, *Journal of the Meteorological Society of Japan*, *82(3)*, 915–931.

[39] Hassenpflug, G., M. Yamamoto, H. Luce, and S. Fukao (2008), Description and demonstration of the new Middle and Upper atmosphere Radar imaging system: 1-D, 2-D, and 3-D imaging of troposphere and stratosphere, *Radio Sci.*, *43*, RS2013, doi:10.1029/2006RS003603.

[40] Hélal, D., M. Crochet, H. Luce, and E. Spano (2001), Radar imaging and high-resolution array processing applied to a classical VHF-ST profiler. *Journal of Atmospheric and Solar-Terrestrial Physics*, *63(2)*, 263–274, doi:10.1016/S1364-6826(00)00135-8.

[41] Hildebrand, P. H., and R. S. Sekhon (1974), Objective determination of the noise level in Doppler spectra, *J. Appl. Meteor.*, *13(7)*, 808–811, doi:10.1175/1520-0450(1974)013<0808:ODOTNL>2.0.CO;2.

[42] Hines, C. O. (1968), A possible source of waves in noctilucent clouds, *J. Atmos. Sci.*, *25*, 937–942.

[43] Hocking, W. K. (1983), On the extraction of atmospheric turbulence parameters from radar backscatter Doppler spectra–I. Theory, *J. Atmos. Terr. Phys.*, *45*, 89–102, doi:10.1016/S0021-9169(83)80013-0.

[44] Hocking, W. K. (1985), Measurement of turbulent energy dissipation rates in the middle atmosphere by radar techniques: A review, *Radio Sci.*, *20(6)*, 1403–1422, doi:10.1029/RS020i006p01403.

[45] Hocking, W. K. (1986), Observation and measurements of turbulence in the middle atmosphere with a VHF radar, *J. Atmos. Terr. Phys.*, *48*, 655–670, doi:10.1016/0021-9169(86)90015-2.

[46] Hocking, W. K. (1997), Recent advances in radar instrumentation and techniques for studies of the mesosphere, stratosphere, and troposphere, *Radio Sci.*, *32*, 2241–2270, doi:10.1029/97RS02781.

[47] Hocking, W. K. and L. Mu (1997), Upper and middle tropospheric kinetic energy dissipation rates from measurements of Cn 2 —Review of theories, in-situ investigations, and experimental studies using the Buckland Park atmospheric radar in Australia, *J. Atmos. Terr. Phys.*, *59*, 1779–1803, doi:10.1016/S1364-6826(97)00020-5.

[48] Hocking, W. K. (2011), A review of Mesosphere–Stratosphere–Troposphere (MST) radar developments and studies, circa 1997–2008, *J. Atmos. Sol.-Terr. Phys.*, *73(9)*, 848–882, doi:10.1016/j.jastp.2010.12.009.

[49] Houze, R. A., Jr (1993), *Cloud Dynamics*, *Int.Geophys.*, vol. 53, pp. 90–93, Academic, San Diego, Calif.

[50] Imai, K., T. Nakagawa, and H. Hashiguchi (2007), Development of tropospheric wind profiler radar with Luneberg Lens Antenna (WPR LQ-7), *SEI TECHNICAL REVIEW-ENGLISH EDITION*, *64*, 38–42.

[51] Ishihara, M. and H. Goda. (2000), Operational 1.3 GHz-wind profiler network of Japan Meteorological Agency, *Proceedings of the Ninth International Workshop on Technical and Scientific Aspects of MST Radar*, 538–540.

[52] Kato, Y., T. Abo, K. Kobayashi, Y. Izumikawa, and M. Ishihara. (2004), The wind profiler network of the Japan Meteorological Agency, *Tenki*, *50*, 891–907.

[53] Kurosaki, S., M. D. Yamanaka, H. Hashiguchi, T. Sato, and S. Fukao (1996), Vertical eddy diffusivity in the lower and middle atmosphere: A climatology based on the MU radar observations during 1986–1992, *J. Atmos. Solar-Terr. Phys.*, *58*, 727–734, doi:10.1016/0021-9169(95)00070-4.

[54] Latteck, R., W. Singer, M. Rapp, B. Vandepeer, T. Renkwitz, M. Zecha, and G. Stober (2012), MAARSY:The new MST radar on Andøya/Norway–System description and first results, *Adv. Radio Sci.*, *47*, RS1006, doi:10.1029/2011RS004775.

[55] Le Foll, G., P. Larzabal, H. Clergeot, and M. Petitdidier (1997), A new parametric approach for wind profiling with Doppler Radar, *Radio Sci.*, *32(4)*, 1391–1408, doi:10.1029/97RS00087.

[56] Lindzen, R. S. (1981), Turbulence and stress owing to gravity wave and tidal breakdown, *J. Geophys. Res.*, *86*, 9707–9714.

[57] Lindzen, R. S. (1984), Gravity waves in the mesosphere, *Dynam. Middle Atmos.*, *3-18*, Dordrecht Press, Tokyo.

[58] Lottman, B. T., and R. G. Frehlich (1997), Evaluation of Doppler radar velocity estimators, *Radio Sci.*, *32(2)*, 677–686, doi:10.1029/96RS03329.

[59] Lott, F. and H. Teitelbaum (1993), Topographic waves generated by a transient wind, *J. Atmos. Sci.*, *50*, 2607–2654, doi:10.1175/1520-0469(1993)050<2607:TWGBAT>2.0.CO;2.

[60] Lucas, C., A. D. MacKinnon, R. A. Vincent, and P. T. May (2004), Raindrop size distribution retrievals from a VHF boundary layer profiler, *J. Atmos. Oceanic Technol.*, *21*, 45–60, doi:10.1175/1520-0426(2004)021<0045:RSDRFA>2.0.CO;2.

[61] Luce, H., Yamamoto, M., Fukao, S., Helal, D., and Crochet, M. (2001), A frequency domain radar interferometric imaging (FII) technique based on high-resolution methods, *J. Atmos. Sol. Terr. Phys.*, *63(2)*, 221–234, doi:10.1016/S1364-6826(00)00147-4.

[62] Luce, H., Hassenpflug, G., Yamamoto, M., and Fukao, S. (2007), Comparisons of refractive index gradient and stability profiles measured by balloons and the MU radar at a high vertical resolution in the lower stratosphere, *Annales Geophysicae*, *25(1)*, 47–57.

[63] Luce, H., T. Mega, M. K. Yamamoto, M. Yamamoto, H. Hashiguchi, S. Fukao, N. Nishi, T. Tajiri, and M. Nakazato (2010), Observations of Kelvin-Helmholtz instability at a cloud base with the middle and upper atmosphere (MU) and weather radars, *J. Geophys. Res.*, *115*, D19116, doi:10.1029/2009JD013519.

[64] Marshall, J. S. and W. M. Palmer (1948), The distribution of raindrops with size, *J. Meteor.*, *5*, 165–166, doi:10.1175/1520-0469(1948)005<0165:TDORWS>2.0.CO;2.

[65] Matuura, N., Y. Masuda, H. Inuki, S. Kato, S. Fukao, T. Sato, and T. Tsuda (1986), Radio acoustic measurement of temperature profile in the troposphere and stratosphere, *Nature*, *323*, 426–428

[66] Matsuno, T. (1982), A quasi-one-dimensional model of the middle atmosphere circulation interacting with internal gravity waves, *J. Meteor. Soc. Japan*, *60*, 215–226.

[67] May, P. T., G. T. Holland, and W. L. Ecklund (1994), Wind profiler observation of tropical storm Float Saipan, *Wea. Forecasting*, *9*, 410–426, doi:10.1175/1520-0434(1994)009<0410:WPOOTS>2.0.CO;2.

[68] May, P. T., and D. K. Rajopadhyaya (1996), Wind profiler observations of vertical motion and precipitation microphysics of a tropical squall line, *Mon. Wea. Rev.*, *124*, 621–633, doi:10.1175/1520-0493(1996)124<0621:WPOOVM>2.0.CO;2.

[69] Mega, T., M. K. Yamamoto, H. Luce, Y. Tabata, H. Hashiguchi, M. Yamamoto, M. D. Yamanaka, and S. Fukao (2010), Turbulence generation by Kelvin-Helmholtz instability in the tropical tropopause layer observed with a 47 MHz range imaging radar, *J. Geophys. Res.*, *115*, D18115, doi:10.1029/2010JD013864.

[70] Mega, T., M. K. Yamamoto, M. Abo, Y. Shibata, H. Hashiguchi, N. Nishi, T. Shimomai, Y. Shibagaki, M. Yamamoto, M. D. Yamanaka, S. Fukao, and T. Manik (2012), First simultaneous measurement of vertical air velocity, particle fall velocity, and hydrometeor sphericity in stratiform precipitation: Results from 47 MHz wind-profiling radar and 532 nm polarization lidar observations, *Radio Sci.*, *47*, RS3002, doi:10.1029/2011RS004823.

[71] Nastrom, G. D. and D. C. Fritts (1992), Sources of mesoscale variability of gravity waves, Part 1: Topographic excitation, *J. Atmos. Sci.*, *49*, 101–110, doi:10.1175/1520-0469(1992)049<0101:SOMVOG>2.0.CO;2.

[72] Nishi, N., M. K. Yamamoto, T. Shimomai, A. Hamada, and S. Fukao (2007), Fine structure of vertical motion in the stratiform precipitation region observed by a VHF Doppler radar installed in Sumatra, Indonesia, *J. Appl. Meteorol. Clim.*, *46*, 522–537, doi:10.1175/JAM2480.1.

[73] O′Sullivan, D. and T.J. Dunkerton (1995), Generation of inertia-gravity waves in a simulated life cycle of baroclinic instability, *J. Atmos. Sci.*, *52*, 3695–3716, doi:10.1175/1520-0469(1995)052<3695:GOIWIA>2.0.CO;2.

[74] Ottersten, H. (1969), Radar backscattering from the turbulent clear atmosphere, *Radio Sci.*, *4(12)*, 1251–1255.

[75] Palmer, R. D., S. Gopalam, T. Y. Yu, and S. Fukao (1998), Coherent radar imaging using Capon's method, *Radio Sci.*, *33(6)*, 1585–1598, doi:10.1029/98RS02200.

[76] Palmer, R. D., T. Y. Yu, and P. B. Chilson (1999), Range imaging using frequency diversity, *Radio Sci.*, *34(6)*, 1485–1496, doi:10.1029/1999RS900089.

[77] Palmer, R. D., P. B. Chilson, A. Muschinski, G. Schmidt, T.-Y. Yu, and H. Steinhagen (2001), SOMARE-99: Observations of tropospheric scattering layers using multiple-frequency range imaging, *Radio Sci.*, *36(4)*, 681–693, doi:10.1029/1999RS002307.

[78] Pollard, B. D., S. Khanna, S. J. Frasier, J. C. Wyngaard, D. W. Thomson, and R. E. McIntosh (2000), Local structure of the convective boundary layer from a volume-imaging radar, *J. Atmos. Sci.*, *57(14)*, 2281–2296, doi:10.1175/1520-0469(2000)057<2281:LSOTCB>2.0.CO;2.

[79] Rajopadhyaya, D. K., P. T. May, R. C. Cifelli, S. K. Avery, C. R. Willams, W. L. Ecklund, and K. S. Gage (1998), The effect of vertical air motions on rain rates and median volume diameter determined from combined UHF

and VHF wind profiler measurements and comparisons with rain gauge measurements, *J. Atmos. Oceanic Technol.*, *15*, 1306–1319, doi:10.1175/1520-0426(1998)015<1306:TEOVAM>2.0.CO;2.

[80] Rao, T. N., D. N. Rao, and S. Raghavan (1999), Tropical precipitating systems observed with Indian MST radar, *Radio Sci.*, *34(5)*, 1125–1139, doi:10.1029/1999RS900054.

[81] Rao, T. N., N. V. P. Kirankumar, B. Radhakrishna, D. N. Rao, and K. Nakamura (2008), Classification of tropical precipitating systems using wind profiler spectral moments. Part I: Algorithm description and validation, *J. Atmos. Oceanic Technol.*, *25*, 884–897, doi:10.1175/2007JTECHA1031.1.

[82] Renggono, F., H. Hashiguchi, S. Fukao, M.D. Yamanaka, S. Y. Ogino, N. Okamoto, F. Murata, B.P. Sitorus, M. Kudsy, M. Kartasasmita, and G. Ibrahim (2001), Precipitating clouds observed by 1.3-GHz boundary layer radars in equatorial Indonesia, *Ann. Geophys.*, *19* , 889–897.

[83] Riedel, K. S., and A. Sidorenko (1995), Minimum bias multiple taper spectral estimation, *IEEE Trans. on Signal Processing*, *43(1)*, 188–195, doi:10.1109/78.365298.

[84] Rogers, R. R., D. Baumgardner, S. A. Ethier, D. A. Carter, and W. L. Ecklund (1993), Comparison of raindrop size distributions measured by radar wind profiler and by airplane, *J. Appl. Meteor.*, *32*, 694–699, doi:10.1175/1520-0450(1993)032<0694:CORSDM>2.0.CO;2.

[85] Röttger, J. and M. Larsen (1990), UHF/VHF radar techniques for atmospheric research and wind profiler applications, in *Radar in Meteorology*, pp. 235–281, American Meteorological Society.

[86] Sato, T., and R. F. Woodman (1982), Spectral parameter estimation of CAT radar echoes in the presence of fading clutter, *Radio Sci.*, *17(4)*, 817–826, doi:10.1029/RS017i004p00817.

[87] Sato, T. (1988), Radar principles, in *Lecture Notes of International School on Atmospheric Radar (ISAR)*, pp. 19–53, Kyoto:Kyoto University.

[88] Sato, T., H. Doji, H. Iwai, I. Kimura, S. Fukao, M. Yamamoto, T. Tsuda, and S. Kato (1990), Computer processing for deriving drop-size distributions and vertical air velocities from VHF Doppler radar spectra, *Radio Sci.*, *25(5)*, 961–973, doi:10.1029/RS025i005p00961.

[89] Sato, T., N. Ao, M. Yamamoto, S. Fukao, T. Tsuda, and S. Kato (1991), A Typhoon observed with the MU radar, *Mon. Wea. Rev.*, *119*, 755–768, doi:10.1175/1520-0493(1991)119<0755:ATOWTM>2.0.CO;2.

[90] Sato, K. (1993), Small-scale wind disturbances observed by the MU radar during the passage of Typhoon Kelly, *J. Atmos. Sci.*, *50*, 518–538, doi:10.1175/1520-0469(1993)050<0518:SSWDOB>2.0.CO;2.

[91] Sato, K., M. Tsutsumi, T. Sato, T. Nakamura, A. Saito, Y. Tomikawa, K. Nishimura, M. Kohma, H. Yamagishi and T. Yamanouchi (2014), Program of the Antarctic Syowa MST/IS radar (PANSY), *J. Atmos. Sol.-Terr. Phys.*, *118*, 2–15, doi:10.1016/j.jastp.2013.08.022.

[92] Schafer, R., S. Avery, P. May, D. Rajopadhyaya, and C. Williams (2002), Estimation of rainfall drop size distributions from dual-frequency wind profiler spectra using deconvolution and a nonlinear least squares fitting technique, *J. Atmos. Oceanic Technol.*, *19*, 864–874, doi:10.1175/1520-0426(2002)019<0864:EORDSD>2.0.CO;2.

[93] Shibagaki, Y., M. D. Yamanaka, H. Hashiguchi, A. Watanabe, H. Uyeda, Y. Maekawa, and S. Fukao (1997), Hierarchical structures of vertical velocity variations and precipitating clouds near the baiu frontal cyclone center observed by the MU and meteorological radars, *J. Meteor. Soc. Japan*, *75*, 569–596.

[94] Shibagaki, Y., M. D. Yamanaka, M. Kita-Fukase, H. Hashiguchi, Y. Maekawa, and S. Fukao (2003), Meso-α-scale wind field and precipitating clouds in Typhoon 9426 (Orchid) observed by the MU radar, *J. Meteor. Soc. Japan*, *81*, 211–228, doi:10.2151/jmsj.81.211.

[95] Slepian, D. (1978), Prolate spheroidal wave functions, Fourier analysis, and uncertainty — V: The discrete case, *The Bell System Technical Journal*, *57(5)*, 1371–1430, doi:10.1002/j.1538-7305.1978.tb02104.x.

[96] Spano, E., and O. Ghebrebrhan (1996a), Pulse coding techniques for ST/MST radar systems: A general approach based on a matrix formulation, *IEEE Trans. Geosci. Remote Sens.*, *34(2)*, 304–316, doi:10.1109/36.485109.

[97] Spano, E., and O. Ghebrebrhan (1996b), Sequences of complementary codes for the optimum decoding of truncated ranges and high sidelobe suppression factors for ST/MST radar systems, *IEEE Trans. Geosci. Remote Sens.*, *34*, 330–345, doi:10.1109/36.485111.

[98] Srivastave, R. C. (1967), On the role of coalescence between raindrops in shaping their size distribution, *J. Atmos. Sci.*, *24*, 287–292, doi:10.1175/1520-0469(1967)024<0287:OTROCB>2.0.CO;2.

[99] Srivastave, R. C. (1971), Size distribution of raindrops generated by their breakup and coalescence, *J. Atmos. Sci.*, *28*, 410–415, doi:10.1175/1520-0469(1971)028<0410:SDORGB>2.0.CO;2.

[100] Sullivan, R. J. (2000), *Microwave Radar: Imaging and Advanced Concepts*, pp. 72–73, Artech House, Norwood.

[101] Tabata, Y., H. Hashiguchi, M. K. Yamamoto, M. Yamamoto, M. D. Yamanaka, S. Mori, F. Syamsudin, and T. Manik (2011), Observational study on diurnal precipitation cycle in equatorial Indonesia using 1.3-GHz wind profiling radar network and TRMM precipitation radar, *J. Atmos. Sol. Terr. Phys.*, *73(9)*, 1031–1042, doi:10.1016/j.jastp.2010.10.003.

[102] Teshiba, M., H. Hashiguchi, S. Fukao, and Y. Shibagaki (2001), Typhoon 9707 observations with the MU radar and L-band boundary layer radar, *Ann. Geophys.*, *19*, 925–931.

[103] Teshiba, M., M. D. Yamanaka, H. Hashiguchi, Y. Shibagaki, Y. Ohno, and S. Fukao (2004), Secondary circulation within a tropical cyclone observed with L-band wind profilers, *Ann. Geophys.*, *22*, 3951–3958.

[104] Teshiba, M., H. Fujita, H. Hashiguchi, Y. Shibagaki, M. D. Yamanaka, and S. Fukao (2005), Detailed structure within a tropical cyclone “eye”, *Geophys. Res. Lett.*, *32*, L24805, doi:10.1029/2005GL023242.

[105] Thomson, D. J. (1982), Spectrum estimation and harmonic analysis, *Proc. IEEE*, *70(9)*, 1055–1096, doi:10.1109/PROC.1982.12433.

[106] Tsuda, T., Y. Masuda, H. Inuki, K. Takahashi, T. Takami, T. Sato, S. Fukao, and S. Kato (1989), High time resolution monitoring of tropospheric temperature with a Radio Acoustic Sounding System (RASS), *Pure Appl. Geophys.*, *130*, 497–507.

[107] Tsuda, T., T. Adachi, Y. Masuda, S. Fukao, and S. Kato (1994), Observations of tropospheric temperature fluctuations with the MU radar-RASS, *J. Atmos. Oceanic Technol.*, *11*, 50–62, doi:10.1175/1520-0426(1994)011<0050:OOTTFW>2.0.CO;2.

[108] Tsuda, T., M. Miyamoto, and J. Furumoto (2001), Estimation of a humidity profile using turbulent echo characteristics, *J. Atmos. Oceanic Technol.*, *18*, 1214–1222, doi:10.1175/1520-0426(2001)018<1214:EOAHPU>2.0.CO;2.

[109] Ulbrich, C. W. (1983), Natural variations in the analytical form of the raindrop-size distribution, *J. Climate Appl. Meteor.*, *22*, 1764–1775, doi:10.1175/1520-0450(1983)022<1764:NVITAF>2.0.CO;2.

[110] Vincent, R. A., S. Dullaway, A. MacKinnon, I. M. Reid, F. Zink, P. T. May, and B. H. Johnson (1998), A VHF boundary layer radar: First results, *Radio Sci.*, *33(4)*, 845–860, doi:10.1029/98RS00828.

[111] Wakasugi K., A. Mizutani, M. Matsuo, S. Fukao, and S. Kato (1986), A direct method for deriving drop-size distribution and vertical air velocities from VHF Doppler radar spectra, *J. Atmos. Oceanic Technol.*, *3*, 623–629, doi:10.1175/1520-0426(1986)003<0623:ADMFDD>2.0.CO;2.

[112] Wilczak, J. M., R. G. Strauch, F. M. Ralph, B. L. Weber, D. A. Merritt, J. R. Jordan, D. E. Wolfe, L. K. Lewis, D. B. Wuertz, J. E. Gaynor, S. A. McLaughlin, R. R. Rogers, A. C. Riddle, and T. S. Dye (1995), Contamination of wind profiler data by migrating birds: Characteristics of corrupted data and potential solutions, *J. Atmos. Oceanic Technol.*, *12*, 449–467, doi:10.1175/1520-0426(1995)012<0449:COWPDB>2.0.CO;2.

[113] Wilson, R. (2004), Turbulent diffusivity in the free atmosphere inferred from MST radar measurements: a review, *Ann. Geophys.*, *22(11)*, 3869–3887, doi:10.5194/angeo-22-3869-2004.

[114] Williams, C. R., W. L. Ecklund, and K. S. Gage (1995), Classification of precipitating clouds in the tropics using 915-MHz wind profilers, *J. Atmos. Oceanic Technol.*, *12*, 996–1012, doi:10.1175/1520-0426(1995)012<0996:COPCIT>2.0.CO;2.

[115] Williams, C. R. (2012), Vertical air motion retrieved from dual-frequency profiler observations, *J. Atmos. Oceanic Technol.*, *29*, 1471–1480, doi:10.1175/JTECH-D-11-00176.1.

[116] Wingo, S. M. and K. R. Knupp (2015), Multi-platform observations characterizing the afternoon-to-evening transition of the planetary boundary layer in northern Alabama, USA, *Boundary-Layer Meteorology*, *155*, 29–53, doi:10.1007/s10546-014-9988-1.

[117] Woodman, R. F. and A. Guillen (1974), Radar observations of winds and turbulence in the stratosphere and mesosphere, *J. Atmos. Sci.,*, *31(2)*, 493–505, doi:10.1175/1520-0469(1974)031<0493:ROOWAT>2.0.CO;2.

[118] Woodman, R. F. (1985), Spectral moment estimation in MST radars, *Radio Sci.*, *20(6)*, 1185–1195, doi:10.1029/RS020i006p01185.

[119] Woodman, R. F. (1997), Coherent radar imaging: Signal processing and statistical properties, *Radio Sci.*, *32(6)*, 2373–2391, doi:10.1029/97RS02017.

[120] Yamamoto, M., T. Sato, P. T. May, T. Tsuda, S. Fukao, and S. Kato (1988), Estimation error of spectral parameters of mesosphere-stratosphere-troposphere radars obtained by least squares fitting method and its lower bound, *Radio Sci.*, *23(6)*, 1013–1021, doi:10.1029/RS023i006p01013.

[121] Yamamoto, M. K., Y. Ohno, H. Horie, N. Nishi, H. Okamoto, K. Sato, H. Kumagai, M. Yamamoto, H. Hashiguchi, S. Mori, N. O. Hashiguchi, H. Nagata, and S. Fukao (2008), Observation of particle fall velocity in cirriform cloud by VHF and millimeter-wave Doppler radars, *J. Geophys. Res.*, *113*, D12210, doi:10.1029/2007JD009125.

[122] Yamamoto, M. K., M. Abo, T. Kishi, N. Nishi, T. H. Seto, H. Hashiguchi, M. Yamamoto, and S. Fukao (2009a), Vertical air motion in midlevel shallow-layer clouds observed by 47-MHz wind profiler and 532-nm Mie lidar: Initial results, *Radio Sci.*, *44*, RS4014, doi:10.1029/2008RS004017.

[123] Yamamoto, M. K., T. Kishi, T. Nakamura, N. Nishi, M. Yamamoto, H. Hashiguchi, and S. Fukao (2009b), Wind observation around the tops of the midlatitude cirrus by the MU radar and Raman/Mie lidar, *Earth Planets Space*, *61*, e33–e36.

[124] Yu, T. Y., and W. O. J. Brown (2004), High-resolution atmospheric profiling using combined spaced antenna and range imaging techniques, *Radio Sci.*, *39*, RS1011, doi:10.1029/2003RS002907.

[125] Yu, T. Y., G. Zhang, A. B. Chalamalasetti, R. J. Doviak, and D. Zrníc (2006), Resolution enhancement technique using range oversampling, *J. Atmos. Oceanic Technol.*, *23(2)*, 228–240, doi:10.1175/JTECH1841.1.

[126] Yu, T. Y., J. I. Furumoto, and M. Yamamoto (2010), Clutter suppression for high-resolution atmospheric observations using multiple receivers and multiple frequencies, *Radio Sci.*, *45*, RS4011, doi:10.1029/2009RS004330.

List of Publications

Journal publications

1. Gan, T., M. K. Yamamoto, H. Hashiguchi, H. Okamoto, M. Yamamoto (2015), Spectral parameters estimation in precipitation for 50-MHz band atmospheric radars, *Radio Science*, in press, doi:10.1002/2014RS005643.

2. Gan, T., M. K. Yamamoto, H. Hashiguchi, H. Okamoto, M. Yamamoto (2014), Error estimation of spectral parameters for high-resolution wind and turbulence measurements by wind profiler radars, *Radio Science*, *49(12)*, 1214-1231, doi:10.1002/2013RS005369.

3. Yamamoto, M. K., T. Fujita, N. H. B. A. Aziz, T. Gan, H. Hashiguchi, T. Y. Yu, M. Yamamoto (2014), Development of a digital receiver for rang imaging atmospheric radar, *Journal of Atmospheric and Solar-Terrestrial Physics*, *118*, 35-44, doi:10.1016/j.jastp.2013.08.023.

4. Gan, T. and G. Y. Ma (2013), An Algorithm for Signal Synthesis and Acquisition of CAPS Based on Dual-Linear Polarization Antennas, *Astronomical Research and Technology*, *2013(1)*, 009.

5. Ma G. Y., Q. T. Wan, T. Gan (2012), Communication-based positioning systems: past, present and prospects, *Research in Astronomy and Astrophysics*, *12(6)*, 601, doi:10.1088/1674-4527/12/6/001.

Presentations at Conferences

1. Gan, T., M. K. Yamamoto, H. Okamoto, H. Hashiguchi, and M. Yamamoto, "Spectral parameters estimation in precipitation using VHF atmospheric radars", *Japan Geoscience Union Meeting 2015*, Chiba, Japan, May, 2015.

2. Gan, T., M. K. Yamamoto, H. Hashiguchi, H. Okamoto, and M. Yamamoto,

"Error estimation of spectral parameters for high-resolution wind and turbulence measurements by wind profiler radars", *14th International Workshop on Technical and Scientific Aspects of MST Radar (MST1/ iMST1)*, São José dos Campos/SP, Brazil, May, 2014.

3. Gan, T., M. K. Yamamoto, H. Hashiguchi, H. Okamoto, and M. Yamamoto, "Measurement of vertical wind in precipitation by the MU radar: A case study", 第8回MUレーダー・赤道大気レーダーシンポジウム(第260回生存圏シンポジウム), Uji, Japan, September, 2014.

4. Gan, T., M. K. Yamamoto, H. Okamoto, H. Hashiguchi, and M. Yamamoto, "Development of a signal processing method for vertical wind velocity measurement by wind profiler radars", *EarthCARE Workshop 2014*, Tokyo, Japan, September, 2014.

5. Gan, T., M. K. Yamamoto, H. Okamoto, H. Hashiguchi, and M. Yamamoto, "Development of a method for estimating vertical wind velocity in precipitation using VHF atmospheric radars", 日本気象学会2014年度秋季大会, Fukuoka, Japan, October, 2014.

6. Gan, T., M. K. Yamamoto, H. Hashiguchi, M. Yamamoto, and H. Okamoto, "Accuracy assessment of spectral parameters of range-imaging wind profiler radars", 第7回MUレーダー・赤道大気レーダーシンポジウム(第233回生存圏シンポジウム), Uji, Japan, September, 2013.

7. Gan, T., M. K. Yamamoto, H. Hashiguchi, H. Okamoto, and M. Yamamoto, "Accuracy assessment of spectral parameters for RIM WPRs", *International Symposium on Earth-Science Challenges (ISEC) 2013*, Uji, Japan, October, 2013.

8. Gan, T., M. K. Yamamoto, H. Hashiguchi, H. Okamoto, and M. Yamamoto, "Accuracy assessment of spectral parameters of range-imaging wind profiler radars", 日本気象学会2013年度秋季大会, Sendai, Japan, November, 2013.